DESIGN, FABRICATION, AND MECHANICAL ANALYSIS OF INTERTWINED AND FRICTIONAL MICRO-ARCHITECTED MATERIALS

Thesis by

Widianto Putra Moestopo

In Partial Fulfillment of the Requirements for the
Degree of
Doctor of Philosophy

CALIFORNIA INSTITUTE OF TECHNOLOGY
Pasadena, California

2023
Defended July 7th, 2022

ACKNOWLEDGEMENTS

Salam damai dan sejahtera bagi kita semua[1]. My Ph.D. endeavour would not have been possible without the support from so many people. It has not been easy, for in this world we all will have trouble. Yet I thank the One who has overcome the world and given me peace amidst the raging waves that at times hit me. To paraphrase one of my favorite songs in this season: Oh Lord, I love You–Your mercy never fails me. All my days, You have held me in Your hands. You have been faithful, even when I do not yet understand. I will sing of the goodness of God.

I would like to thank my one and only Ph.D. advisor, Professor Julia R. Greer. Thank you for believing in me, guiding me within the large bounds of freedom you have allowed me to have during my scientific explorations, restarting group retreats and implementing office hours, supporting me to go to conferences, and overall helping me grow into a better independent researcher. Thank you for pushing me to hone my research and ideation skills — I have continued to grow in my appreciation of your scientific fervour and endeavours. I look back fondly upon my time in your research group and I do not take it for granted.

I would also like to thank Professor Sergio Pellegrino for serving as the Chair of my Thesis Committee, Professors Kaushik Bhattacharya and Domniki Asimaki for serving in my Thesis Committee, and Professor Chiara Daraio for serving in my Candidacy Committee. All of these professors, along with Professors Katherine Faber, Ares Rosakis, Nadia Lapusta, Guruswami Ravichandran, and Kostia Zuev, have taught me through the courses I took in Caltech, and I would like to thank them for teaching such great classes that have helped me grow as a scientist, an engineer, a researcher, and a thinker.

To Dr. Carlos Portela, I send you my gratitude for taking me under your wings when I started grad school. It would be hard to imagine a smoother transition to (the challenge of) grad school without your mentorship, and I believe the students that you are mentoring and teaching now are so fortunate to have such a caring and talented person guiding them. I want to thank Dr. Michael Cai Wang for introducing me to the rigor of research and helping me prepare for grad school — RateMyProfessors.com gives you a high rating as a teacher, and it is well deserved. I also would like to thank Professor SungWoo Nam for enabling me to do undergraduate research back

---

[1] Peace be upon us.

in UIUC. To the Greer group alums who have warmly welcomed me into the group and helped me navigate grad school and life, many thanks!

Thank you Sammy Shaker for not only being my collaborator but also a great friend in the lab and a fun group chat host. Thank you Weiting Deng for working with me and being my office mate for a time. I want to thank Seola Lee for being a great discussion and mentoring partner. Thank you Wenxin Zhang for collaborating on the tension tip — I hope the experience serves you well in the future. Thank you Dr. Arturo Mateos and Ritchie M. Fuller for introducing me, along with Dr. Carlos Portela, to the hierarchical woven lattice world. To Dr. Bryce Edwards, now-Dr. Amylynn Chen, and Dr. Daryl Yee, thank you for allowing me to be part of your projects and gain new skills and knowledge. Thank you Zane Taylor for working together in the MPEC project, and Kanthasamy Ubamanyu for helping me get access to Guggenheim, especially in 2020. I am grateful for the support of the staff members in Caltech: Carolina Oseguera, Elizabeth Rodriguez, Angie Riley, Holly Golcher, Jennifer Campbell, Lynn Seymour, Christy Jenstad, Jennifer Blankenship, Jennifer Palmer, and the Steele and Keck custodians. I would also like to thank the National Science Foundation for their support of my doctoral studies through the Graduate Research Fellowship, and also to the MCE Department and the Henry L. Guenther Foundation for their support through the Guenther Fellowship.

To my Greer group cohort, what a ride it has been. I am grateful for each one of you (now-Drs. Rebecca, Max, Amy, Fernando), not only for the expertise and mentorship you bring to the group, but also for being great lab mates these past five years. Thank you to my mentees, Ivan Grega, Makyla Boyd, and Ben Spöttling, for allowing me to be your mentor in researching different topics together. To the previous and current mechanics/architected materials subgroup, thank you for being a great place to discuss science. Shout out to Kevin for being a great office mate and lab mate, to Thomas for being a great presence in the lab, and to spice night for being a fun place to hang out, especially in my last few months as a Ph.D. candidate.

Thank you Nachi for being a really great friend these past five years. My time here would not have been the same without you. Andy, what a privilege to have you, my brother in Christ, as my roommate and eventually as my neighbor during grad school. Thank you Gunho for going through the grad school rigor with me and having fun with all of us. Thank you Max and Harsha for the continued friendships we have regardless of our physical address. Thank you Sylvain, Chelsea, and Anushri–along with Max, Andy, Harsha, and Nachi–for being great roommates I had the pleasure of sharing living spaces with. I am also grateful for all the friends I went on national park/beach adventures with, shared yummy food with, had great conversations with, and/or worked for long hours with. To the vibrant MCE community: I enjoyed hanging out with all of you and competing on the soccer (football) pitch together. Thank you also to all the folks I have had the pleasure of playing basketball and frisbee with.

My GCFam: you all have become the one constant community amidst seasons of change. I cherish our fellowship together and I thank God for the strength, peace, joy, faith, and love that overflow through you and become blessings to others throughout my time at Caltech. What a blessing it is for me to have been able to wrestle with tough things and share God's goodness together with all of you, whether it is through our weekly gatherings or even through hosting a Science and Faith Examined event. Albert, Voon, Bekah, Kim, Jamie, Josh, Mark, Tanner, Nathan, Maria, Hannah, Rachel, Grace, Sami, Sara, Grigory, and many others I have wished to list here — thank you! I also extend my gratitude to Grace Pasadena and Fellowship for providing a place to worship and gather together.

My time in college (undergraduate), high school, all the way to childhood have helped shape me into who I am today. Joshua Weakly, I am grateful to be discipled by you during college and for our continuing friendship. Thank you to my buddies, Matt Tse and Bryant Lash, for being such great friends through the years–it is a blessing to be able to continue our fellowship. Also thanks for the Buc-ee's tank. Cole Fritz, thank you for your continued friendship ever since I made the big move. Thank you to the Illini Navs, Permias UIUC, Illini EcoConcept, Kairos, my previous host families and many other families that have cared for me, SF group, SD friends (shout out to Ical), as well as the teaching and support staff members from when I was in UIUC, Wheaton Academy, SMP Taruna Bakti, and SD & TK Prof. Dr. Moestopo. Shout out to Mama's Pondok Gembira.

I would like to thank my grandparents, two of whom passed away before I was born and the other two I had the privilege of sharing life with, for fighting throughout the decades to allow the younger generations to experience freedom and pursue meaningful endeavours. It is easy to forget that the world was much different only a few decades ago. To my Moestopo and Soekardi extended families, thank you so much for your support throughout the years — it means a lot to me. Thank you also to the Maxey and Kuhns families who opened their arms widely as I joined their families via marriage.

Mama, thank you for everything. Truly, truly, thank you. You have gone through a lot, and I hope that we have even better days ahead together as a family. Papa, thank you for teaching me to be a thinker and constantly affirming me in the ups and downs. Icon, thank you for being a brother who cares for me and bringing Ka Silvi and Malen into the family. And Lena: I love you, and I am so grateful that I have you in my life. Thank you for all the support and commitment in Christ through the storms and the still sea. I would not alter my grad school experience in any way if doing it means I do not have you in my life.

ABSTRACT

Natural biomaterials, e.g., shells, bone, and wood, are typically comprised of hard and soft constituent materials that are hierarchically ordered to achieve mechanical resilience, light weight, and multifunctionality. Advanced fabrication techniques have enabled the creation of precisely architected materials with exceptional mechanical properties unattainable by their constituent materials, yet they are often designed with fully interconnected structural members whose junctions are detrimental to their performance because they serve as stress concentrations for damage accumulation and lower mechanical resilience. Most studies have also focused on understanding the stretching, bending, and buckling of the structural members, while explorations toward contact interactions within structural members remain limited. We address these challenges by (i) introducing a new three-dimensional (3D) hierarchical architecture in which fibers are interwoven to construct effective beams, (ii) introducing the concept of knots into the hierarchical architecture framework, and (iii) developing a model to study the effects of structural element length scale on the energy dissipation capability of a frictional architected material.

We first explore the effective lattice response of hierarchical woven microlattices, and we demonstrate the superior ability of woven architectures to achieve high tensile and compressive strains via smooth reconfiguration of woven microfibers in the effective beams and junctions without failure events. We study how fiber topology and constituent materials influence the mechanical behaviors of hierarchical intertwined structures, and we compare our results with theory. Our study reveals that knot topology allows a new regime of deformation capable of shape-retention, leading to increased absorbed energy and failure strain compared to structures with woven topology. Agreements between experimental results and a model for long overhand knots suggest that the model can aid the optimization of the mechanical performance of microwoven materials. We then adapt classical contact mechanics and adhesion models to explore the influence of the size of structural elements in a frictional architected material on its energy dissipation capability. Our model shows that the energy dissipation capability of our frictional architected material can be significantly increased when it is scaled down from the mm-scale to the sub-micron length scale.

Our woven hierarchical design offers a pathway to make traditionally stiff and brittle materials more deformable and introduces a new building block for 3D architected materials with complex nonlinear mechanics. The unique tightening mechanism introduced by knotted topology unlocks new ways to create shape-reconfigurable, highly extensible, and extremely energy-absorbing bulk, 3D architected materials with mechanical properties that can be tuned not only by their geometries and bulk properties, but also by the surface interactions experienced by the structural elements. Lastly, our modeling work shows the potential of creating highly dissipative architected materials with shape-retention capability via carefully architected structural elements.

PUBLISHED CONTENT AND CONTRIBUTIONS

This thesis has been directly adapted from:

1) W.P. Moestopo, A.J. Mateos, R.M. Fuller, J.R. Greer, & C.M. Portela. "Pushing and Pulling on Ropes: Hierarchical Woven Materials". *Advanced Science* **7**, 20, (2020). DOI: 10.1002/advs.202001271
   Contributions: Participated in the conception of the project, designed and fabricated the samples, conducted the experiments, analyzed the data, and wrote the manuscript.

2) W.P. Moestopo, S. Shaker, & J.R. Greer. "Knots are Not for Naught: Design, Properties, and Topology of Intertwined Micro-Architected Materials". In preparation.
   Contributions: Conceived the project, designed and fabricated the samples, conducted the experiments, analyzed the data, and wrote the manuscript.

3) W.P. Moestopo, W. Deng, & J.R. Greer. "Adhesion-Friction Size Effects in Mechanical Metamaterials". In preparation.
   Contributions: Conceived the project, derived the analytical model, designed the samples, fabricated a portion of the samples, analyzed the data, and wrote the manuscript.

Not directly adapted in this thesis:

4) A.C. Chen, W.P. Moestopo, Z.W. Taylor, S. Lee, D.W. Yee, & J.R. Greer. “Vat Polymerization of Compliant and Tough Metal-Coordinated Polymers with Tunable Mechanical Properties”. In preparation.
   Contributions: Designed and conducted a portion of the experiments, analyzed the data, and participated in the writing of the manuscript.

5) M. Maurizi, B.W. Edwards, C. Gao, J. R. Greer, & F. Berto. "Fracture Resistance of 3D Nano-Architected Lattice Materials". In review.
   Contributions: Participated in designing and conducted a portion of the experiments.

TABLE OF CONTENTS

LIST OF ILLUSTRATIONS

LIST OF TABLES

NOMENCLATURE

Amontons-Coulomb friction laws. Basic empirical laws of dry friction which state that, in sliding contact, (i) friction force is independent of the apparent or nominal contact area, (ii) friction force is proportional to the normal force, (iii) friction force is in the opposite direction as the direction of sliding, and (iv) friction force is indepedent of the speed of sliding.

DMT model. Contact mechanics model developed by Derjaguin, Muller, and Toporov (DMT). The model describes the mechanics of contacting surfaces in the presence of surface adhesion and is deemed more appropriate to use when surface forces have a longer range compared to the resulting elastic deformations.

JKR model. Contact mechanics model developed by Johnson, Kendall, and Roberts (JKR). The model describes the mechanics of contacting surfaces in the presence of surface adhesion and is deemed more appropriate to use when surface forces have a shorter range compared to the resulting elastic deformations.

Chapter 1

INTRODUCTION

1.1 Background on Architected Materials

An architected material is a combination of several materials, including open space, configured to attain unique properties that cannot be achieved by the constituent materials alone. Nature provides an abundance of examples of architected materials in the forms of cellular solids, and their feature sizes range from the nanoscale to macroscale [1]. Features with differing length scales in natural materials form hierarchical architectures, enabling these materials to obtain properties unattainable by their constituent materials such as high specific strength in bone, nacre, and diatoms [2, 3] (see also Figure 1.1). Similarly, synthetic architected materials are developed with a goal to reach previously unattainable material properties, such as stiff-and-lightweight [4–7], ultralow thermal conductivity [8], high mechanical resilience [9], negative Poisson's ratio [10], tunable band gaps [11, 12], acoustic wave focusing [13], mechanical "unfeelability" [14, 15], and negative coefficient of thermal expansion [16].

Along with the advancement of fabrication methods, designs for architected materials continue to progress and push the boundaries of material properties. In the area of structural architected materials, the development of high-performance composite materials started in the prior decades has led to the recent commercialization and widespread use of composite materials [17]. In recent years, advances in additive manufacturing have provided more versatile tools to fabricate architected materials from the centimeter scale (direct ink writing [18], continuous digital light processing [19], volumetric additive manufacturing [20], etc.) to the micro- and nanoscale (microstereolithography [21], two-photon lithography [22], etc.). Hierarchical beam-based designs resembling the Eiffel Tower [23] can now be manufactured with nanoscale feature sizes [9]. The ability to fabricate architected materials with feature sizes on the order of nanometers is important due to the material strengthening size-effects at these small length scales [24].

The mechanical properties of cellular solids have been studied extensively over the past few decades [25–28]. The classical model for a cellular solid uses beam theory to model the relationships between the mechanical properties of the material and its

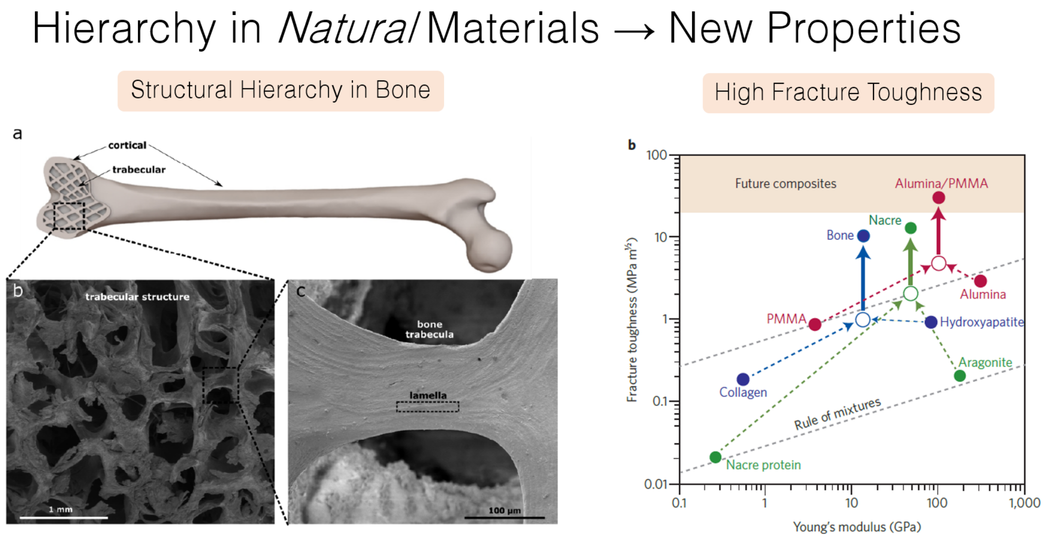

Figure 1.1: Architectural hierarchy in natural materials leads to new properties. Well-known examples include the increased fracture toughness in bone and nacre through hierarchical designs of their structures. The figure on the left is reprinted by permission from IOP Publishing: Bioinspiration & Biomimetics, O. A. Tertuliano et al. ©2021, and the figure on the right is reprinted by permission from Spring Nature: Nature Materials, U. G. K. Wegst, et al. ©2015.

constituent material properties, relative density ($\bar{\rho} = \frac{\rho}{\rho_s}$), and geometry. The relative density is the ratio between the density of the architected material, ρ, and the density of the constituent material, ρ_s. In the classical model, the Young's modulus (E), yield strength (σ_y), and fracture toughness (K_{Ic}) have the following relationships:

$$E = c_1 E_s \bar{\rho}^{\alpha}, \tag{1.1}$$

$$\sigma_y = c_2 \sigma_{ys} \bar{\rho}^{\beta}, \tag{1.2}$$

$$K_{Ic} = c_3 \bar{\rho}^{\gamma}, \tag{1.3}$$

where E_s is the constituent material's Young's modulus, σ_{ys} is the yield or failure stress of the constituent material, c_1, c_2, and c_3 are proportionality constants, and α, β and γ are scaling exponents. The proportionality constants and scaling exponents are related to the type architecture being investigated. For a further discussion on characterizing fracture toughness in architected materials, see Reference [29].

While foams and natural cellular solids generally have architectures that deform primarily by the bending of their components, beam-based lattice design has shown promise to optimize an architected material such that it becomes stiff and yet lightweight [30]. The design process for beam-based lattice designs benefits from theoretical frameworks for general structures such as the ones developed by Pellegrino & Calladine [31–33]. They deem that Maxwell's Rule of rigidity ($3j-b-k=0$ in 3D) is necessary but not sufficient, and they expand it by incorporating the states of self-stress and zero-energy mechanisms present in a pin-jointed structure:

$$3j-b-k=s-m, \tag{1.4}$$

where j is the number of junctions, b is the number of beams, k is the number of kinematic (degree-of-freedom) constraints, s is the number of states of self-stress, and m is the number of zero-energy mechanisms. In general, a pin-jointed structure can be considered as rigid ($m=0$), non-rigid ($m>0$), or periodically rigid ($m=0$ when periodic boundary conditions are imposed upon the lattice unit cell). In a rigid structure, deformation is allowed only if certain beams deform by stretching, which explains how a rigid structure can have a higher stiffness than a non-rigid structure of the same relative density. For a stretching-dominated 3D lattice, the classical model predicts that $\alpha=\beta=1$ [26] and experiments have shown that it is possible to have $\gamma=1$ [34]. For a bending-dominated 3D lattice, the classical model predicts that $\alpha=2$ and $\beta=\gamma=3/2$ [35].

1.2 Current Challenges in Architected Materials

While beam-based lattice architectures have shown promise to produce lightweight architected materials with high stiffness and strength, as well as programmed behaviors [36], their performance has been limited by the geometry of the junctions. In lattices with higher relative densities, beams are less slender and the node (junction) sizes also become larger assuming that the junctions are not tapered. Meza et al. have shown that stretching-dominated lattices become more bending-dominated in higher $\bar{\rho}$ [37], and Portela et al. further prove this by numerically showing that the strain energy transitions from being mainly distributed within the beams to being mainly localized at the junctions as $\bar{\rho}$ increases [38]. Portela et al. also report an extension to the stiffness scaling laws for stretching- and bending-dominated structures (Eq. 1.1) by adding a higher order $\bar{\rho}$ term for each type of structure. Fusion of structural members in junctions also lead to high stress concentrations; beam lattice architectures have been shown to be susceptible to failure due to stress concentrations at the junctions which initiate cracks, leading to catastrophic failure [39]. Incremental improvements in stiffness and compressive strength of architected materials have been achieved by modifying the nodal structures in beam-based architecture according to minimal surface theory [40] or by mimicking a spinodal structure [41].

However, these shell-based designs still suffer from significant degradation upon repeated large deformations unless material fill fraction is very low.

1.3 Lessons from Woven Materials and Knots

As alternatives to interconnected design, interpenetrating lattice and chain mail-like designs have recently been explored [42–44], showing the potential to achieve multifunctionality while being composed of a number of interconnected constituent members. Wire-woven architected materials have desirable energy absorption capabilities and buckling suppression [45–47], presenting a potential approach to enable repeatable deformability and multifunctionality, but have lacked the introduction of hierarchy to further enhance these properties. When the fiber geometry and connectivity within the larger woven architected material system are considered, the complexity associated with contact friction, entanglement, sliding, and bending of fibers during global deformation, along with the properties of the constituent material, renders the understanding of the mechanical properties of woven architected materials far from complete. For example, a change in how may times a fiber is revolved in a woven beam alone can lead to a non-negligible shift in the onset of stiffening when the lattice is pulled [48]. To gain intuition in studying the complexity of the mechanics of hierarchical woven lattices, several lessons can be taken from knots, which are analogous to fiber entanglement in woven materials. Knots can be found in a wide range of length scales: from sailing, climbing, and sutures, all the way to the entanglement of DNA, protein, and polymer strands [49–52]. The structure (topology) of knots itself has been a topic of interest for centuries in the field of mathematics [53, 54]. Researchers have found that even if two knots have seemingly similar configurations (i.e., number of crossings), a slightly different twist can lead to one knot being unstable and the other stable [55–57].

In earlier explorations, tight configurations of a knot have been observed to break near the entrance and exit points of a knot, and these phenomena were attributed to the corresponding curvature peaks in an ideal, or tightest, knot model and the corresponding regions of localized elastic strain energy in molecular dynamics simulations [52, 58]. More recent explorations have shown that the mechanical properties of tight, physical knots are more complicated; the properties of the constituent material can influence where and how the knots break due to the reduction of cross-sectional area and torsion [59–61]. For loose configurations of knots, a recent study has found that the increase in contact area and the accompanying friction can significantly affect the deformability of a simple overhand knot [62]. Another set of studies on loose slip knots have also shown the ability of friction in knots to increase fiber toughness by multiple orders of magnitude while allowing/disallowing the knots to untie [63–65]. These studies suggest that understanding the mechanics of hierarchical woven materials will require not only for geometry to be considered, but friction and constituent material properties as well.

1.4 Outline and Objectives

The aim of this thesis is to explore novel architected material design concepts, characterize their mechanical properties, and elucidate the important mechanisms that govern their mechanical behaviors. Specifically, we focus on developing architected material design frameworks that allow for high resilience, extreme deformability, and enhanced energy dissipation. In Chapter 2, we discuss the design, fabrication, characterization, and computational techniques we utilize in our studies. We then introduce a new hierarchical design concept in Chapter 3 in which monolithic beams are transformed into intertwined fibers that are not fused together at the effective junctions. The effective lattice properties in tension and compression are discussed in this chapter, along with comparison to previously reported architected materials. In Chapter 4, we introduce the concept of knotted fiber topology into the hierarchical intertwined material framework, a topology that is uniquely available for intertwined materials due to the fact that their fibers can slide within the effective junctions. We discuss how varying the fiber topology and the constituent material properties of intertwined materials affect their mechanical behaviors, and we compare our experimental results of knotted structures with theory on simple overhand knots. In Chapter 5, we explore the effect of reducing the length scale of the structural elements of architected materials with frictional mechanisms by developing a simplified architected material model that takes into account adhesion between contacting surfaces. We conclude this thesis by discussing open questions and future research directions to realize new materials with previously unattainable properties and real-world impacts.

Chapter 2

METHODS

This chapter is adapted from:

W.P. Moestopo, A.J. Mateos, R.M. Fuller, J.R. Greer, & C.M. Portela. "Pushing and Pulling on Ropes: Hierarchical Woven Materials". *Advanced Science* **7**, 20, (2020).
Contributions: Participated in the conception of the project, designed and fabricated the samples, conducted the experiments, analyzed the data, and wrote the manuscript.

W.P. Moestopo, S. Shaker, & J.R. Greer. "Knots are Not for Naught: Design, Properties, and Topology of Intertwined Micro-Architected Materials". In preparation.
Contributions: Conceived the project, designed and fabricated the samples, conducted the experiments, analyzed the data, and wrote the manuscript.

W.P. Moestopo, W. Deng, & J.R. Greer. "Adhesion-Friction Size Effects in Mechanical Metamaterials". In preparation.
Contributions: Conceived the project, derived the analytical model, designed the samples, fabricated a portion of the samples, analyzed the data, and wrote the manuscript.

2.1 Design and Fabrication

Advanced fabrication techniques have enabled the creation of structures with complex geometries and unique functionalities. Scientific explorations presented in this thesis utilized cutting edge additive manufacturing techniques to fabricate novel structures in the micron and sub-micron length scale that would otherwise be very difficult to synthesize using common substractive manufacturing techniques (e.g., milling, electron-beam lithography). All monolithic and hierarchical woven lattices for the work discussed in Chapter 3 were fabricated out of IP-Dip photoresist via two-photon lithography using a commercially available system (Photonic Professional GT, Nanoscribe GmbH). Each sample was written on a Si substrate using laser power and scan speed of 15 mW and 10 mm s^{-1}, respectively. All lattices were designed to have 30-µm unit cell width and 4x4x4 unit cells, and they were printed with equal hatching (d_h) and slicing (d_s) distance of 0.1 µm, with the exception of monolithic octahedron lattices which were printed with hatching and slicing distances of 0.2 µm and 0.1 µm, respectively; for both woven and monolithic lattices, a contour line was printed on the perimeter of each printed cross-section. All IP-Dip pillars were printed with equal hatching and slicing distance of 0.2 µm and without contour line. For tension and tension-to-compression samples, the Si substrates were silanized prior to writing to improve adhesion between the samples and the chips. Critical point drying was performed on written samples using Autosamdri 931 (Tousimis). To ensure that the tested lattice samples had relative densities close to the intended design, radii of selected fibers were measured from the top and/or the side of each sample. Fiber cross-sectional areas were then estimated using the radii measurements and compared to the cross-sectional area in the design.

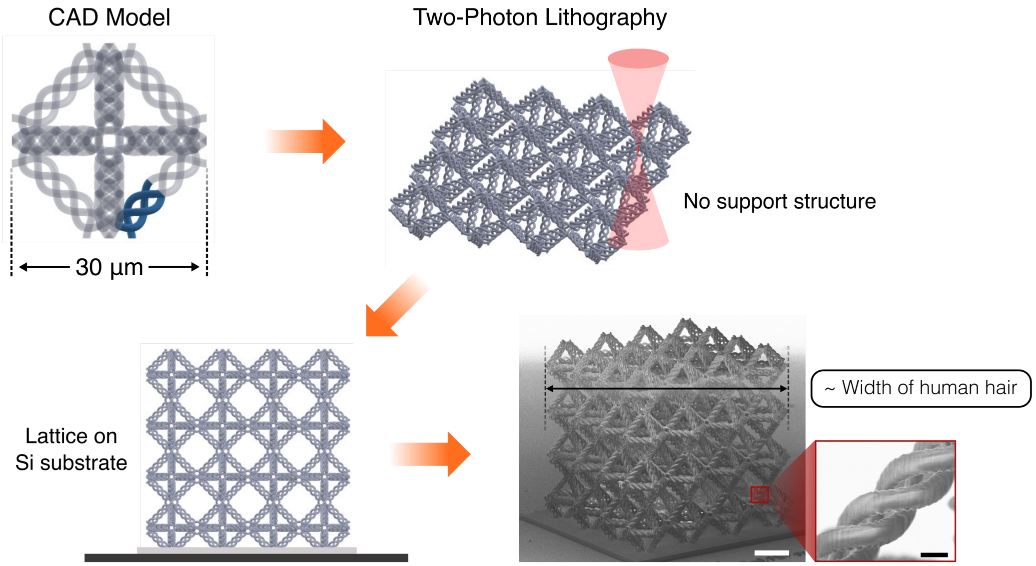

Figure 2.1: Design and fabrication of hierarchical woven lattices. This example shows tessellations of woven octahedron unit cells composed of woven structural elements (highlighted in blue). The width of a fabricated lattice is around the width of a human hair. White scale bar corresponds to 20 µm, and black scale bar in the inset is 2 µm.

The intertwined structures and pillars in Chapter 4 were also fabricated in a similar manner. We first fabricated polymeric intertwined and monolithic structures out of IP-Dip photoresist using two-photon lithography via a commercially available Photonic Professional GT System (Nanoscribe GmbH). All structures were additively manufactured on a silanized Si substrate with laser power and scan speed set at 15 mW and 10 mm s^{-1}, respectively. Structures originating from the same batch were printed on the same Si substrate within one printing run. An equal hatching (d_h) and slicing (d_s) distance of 0.1 μm was prescribed for each intertwined rhombus structure and monolithic structure (pillar and plate). The base and top cap of each monolithic pillar was printed using $d_h = d_s = 0.1$ μm, while the base and top cap for each intertwined structure had $d_h = d_s = 0.2$ μm. IP-Dip plates of dimensions 3.5 μm x 3.5 μm x 0.3 μm (LxWxH) were fabricated with ~20 min and subsequently dried via critical point drying in Autosamdri 931 (Tousimis). To fabricate passivated structures, select polymer structures were conformally coated with 5-nm thickness Al_2O_3 using a plasma-enhanced atomic layer deposition (ALD) process inside a FlexAL II system (Oxford Instruments). The chamber was held at 200 °C, and trimethylaluminum and O2 were used as precursors, resulting in 1.2 Å/cycle growth rate.

Hexagonal frictional unit cells in Chapter 5 were fabricated out of a customized resin based on pentaerythritol tetraacrylate (PETA) using two-photon lithography (oil-immersion technique, 63x lens) via Photonic Professional GT System (Nanoscribe GmbH). 0.6g of PETA and 150mg DETC were added to a 10-mL vial and sonicated for 15 minutes to form a clear homogeneous photoresist solution. Laser power of 35 mW, scan speed of 70 mm s^{-1}, and slicing distance (d_s) of 80 nm were implemented. The samples were dried using a critical point drying process in an Autosamdri 931 system (Tousimis).

2.2 Mechanical Testing

In the work on hierarchical woven lattices discussed in Chapter 3, quasi-static uniaxial tension and tension-to-compression experiments were performed using a custom-made tension tip attached to a nanoindenter (InSEM, Nanomechanics Inc.) installed in an SEM (FEI Quanta 200F) to enable in situ imaging of the experiments. In situ quasi-static compression experiments were performed using a compression tip on the same nanoindenter, and cyclic ex situ compression experiments were performed in a G200 XP Nanoindenter (Agilent Technologies) up to 35% strain. For each architecture (woven vs. monolithic) and unit cell configuration, three samples were tested in tension up to failure and at least three samples were tested under cyclic compression. Normalized energy absorption and effective modulus data from compression cycles that did not go all the way to 35% strain were omitted. All lattice samples were loaded at a strain rate of 3 x $^{-4}$ s^{-1}, and all pillars were loaded at

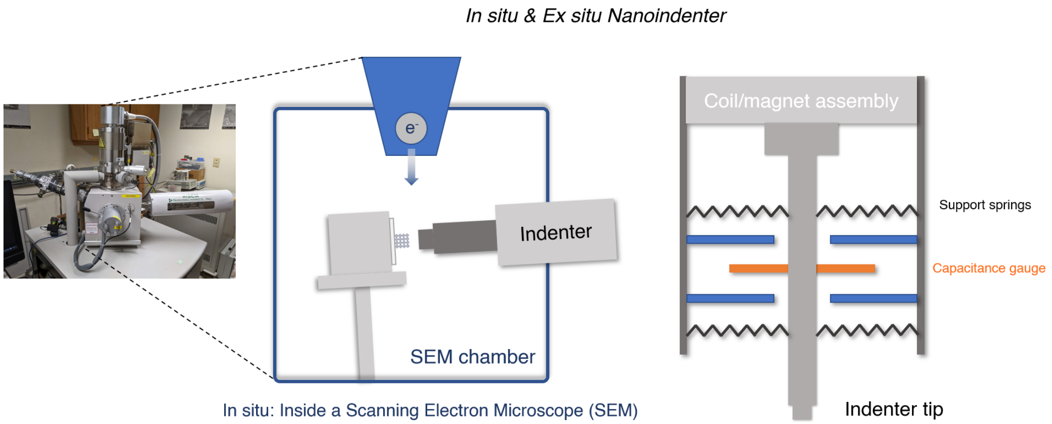

Figure 2.2: Diagram of in situ and ex situ indenters for mechanical testing. A variety of tip geometries can be mounted on a nanoindenter to probe the mechanical properties of the sample.

a displacement rate of 30 nm s^{-1}, which falls around the machine displacement-limit and corresponds to a strain rate of 4.3 x 10^{-4} s^{-1}. Stress is calculated using $\sigma = \frac{F}{A}$, where F and A are load and the initial cross-sectional area of the lattice perpendicular to vertical loading direction, respectively. Engineering strain ε is calculated by normalizing vertical displacement by the gauge length. In tension and tension-to-compression experiments, measured vertical displacements were corrected to account for the compliance of the IP-Dip grip heads and base (see Figures 2.5–2.6 and Equation 2.3). The absolute absorbed energy density W_{abs} is calculated as the area inside the stress-strain curve, which equals to Equation 2.1 for cyclic experiments. Explicit outliers in cyclic compression data were removed. The toe region of the stress-strain curve, which indicates the measured initial deformation before full contact was established between the sample and the indenter tip, was removed from each data set except for cyclic compression data. Unless otherwise noted, experimental lattice data came from at least three different samples and are presented as mean ± standard deviation. Statistical analysis was carried out using MATLAB.

We calculated the dissipated energy density per i-th compression, ΔU_i, as the area enclosed by each stress (σ) vs. strain (ε) cycle,

$$\Delta U_i = \oint \sigma \, d\varepsilon, \tag{2.1}$$

and report the first-cycle-normalized quantities Π_i, defined as

$$\Pi_i = \frac{\Delta U_i}{\Delta U_1}. \tag{2.2}$$

For the work shown in Chapter 4, uniaxial tension experiments were also performed using custom-made tension tips attached to the same nanoindenter (InSEM, Nanomechanics Inc.) installed in the same scanning electron microscope (FEI Quanta 200F). Stress (σ) is defined as the engineering stress $\sigma = \frac{F}{A}$, where F and A are the measured load and the initial cross-sectional area of the sample perpendicular to the vertical loading direction, respectively. Strain (ε) is defined as the engineering strain $\varepsilon = \frac{\delta}{H}$, where δ is the sample displacement and H is the initial height of the sample. Displacement values for intertwined structures were obtained from the nanoindenter and corrected using a compliance correction method while displacement values for pillars tested in tension were obtained via digital image tracking. No significant deviation is observed between the compliance correction method and digital image tracking for rhombus testing (Figure 2.3). Unless otherwise noted, each experiment was performed within nine days after fabrication using a strain rate of 1 x 10^{-3} s^{-1}. Structural dimensions of each sample were measured inside the scanning electron microscope prior to mechanical testing, and measurements of fiber diameters were used to calculate the effective fiber cross-sectional area for each sample.

Strain Rate Determination for Lattice Experiments

To determine the acceptable strain rate for our quasi-static experiments on polymeric structures in Chapter 3, we performed compression tests up to 30% strain on octahedron lattices using the strain rate that is commonly found in literature (1 x 10^{-3} s^{-1}) and the lowest achievable strain rate for our testing set up (3 x 10^{-4} s^{-1}). Figure 2.4 shows the measured strain of the lattice at a specified time after the indenter tip and the sample lost contact during unloading. The lower strain rate corresponds to a smaller unloading strain lag between the indenter and the sample when they lost contact (~1% less strain than with the larger strain rate). Once the strain values settled, the lower strain rate corresponds to a lower strain, which can be interpreted as less plastic deformation. Therefore, we concluded that all experiments should be conducted at a strain rate that was as close to 3 x 10^{-4} s^{-1} as possible. Further explorations should take into account the strain rate dependency of the lattice constituent material which can potentially be studied via dynamic mechanical analysis (DMA) and rheological testing, as appropriate.

Compliance Correction

Due to less-than-optimal video quality that has been deemed inadequate to produce accurate digital image correlation, we have chosen to methodically perform a rigor-

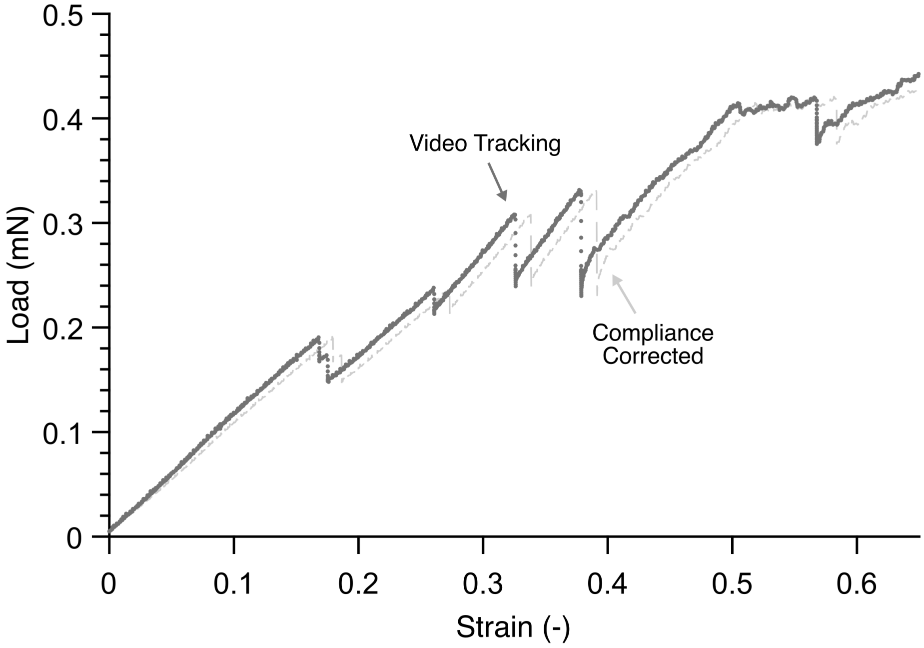

Figure 2.3: Comparison between data correction methods. Load vs. strain data from a rhombus of H = 70 μm tested in tension up to failure and corrected using (i) the compliance correction method and (ii) digital image tracking. The lack of deviation between the two data sets shows that both methods are comparable to one another. Note that charging on polymer surface during prolonged imaging inside an SEM may induce measurement errors when using digital image tracking.

ous compliance correction procedure to present accurate tensile data. The custom set up for tension and tension-to-compression experiments requires the fabrication of IP-Dip grip head via two-photon lithography directly after the writing of each sample. An IP-Dip base was also fabricated underneath each lattice sample to improve adhesion to the Si substrate. Since the compliance of the grip head (C_{grip}) and the compliance of the base (C_{base}) cannot be assumed to be infinitely small compared to the compliance of the lattice sample, the vertical displacement of the lattice (u_{lat}) needs to be corrected as follows:

$$u_{total} = u_{lat} + u_{grip} + u_{base}$$

$$u_{total} = (C_{lat} + C_{grip} + C_{base}) \cdot Load,$$

where u_{total}, u_{grip}, and u_{base} are the displacements of the nanoindenter, the grip head, and the base, respectively, and C_{lat} is the lattice compliance. Here, the nanoindenter (labeled as machine) and the Si substrate are assumed to be rigid with respect to the IP-Dip components. Using the stiffness-compliance relationship

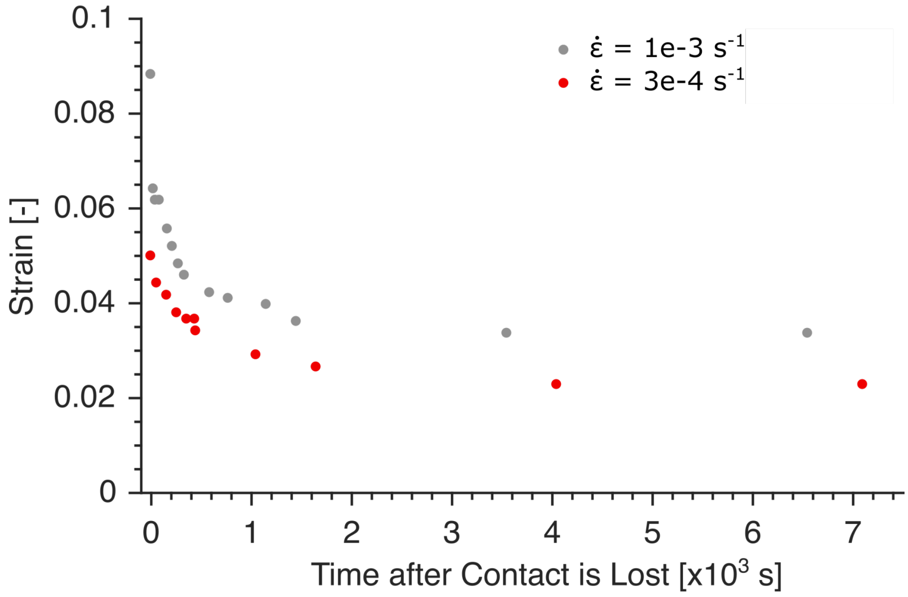

Figure 2.4: Compressive strain vs. time data showing viscoelastic creep phenomena of octahedron IP-Dip woven lattices ($\bar{\rho} \cong 5$ %) under two different strain rates once contact was lost between the indenter tip and the corresponding sample during the unloading portion of a compression up to 30% strain.

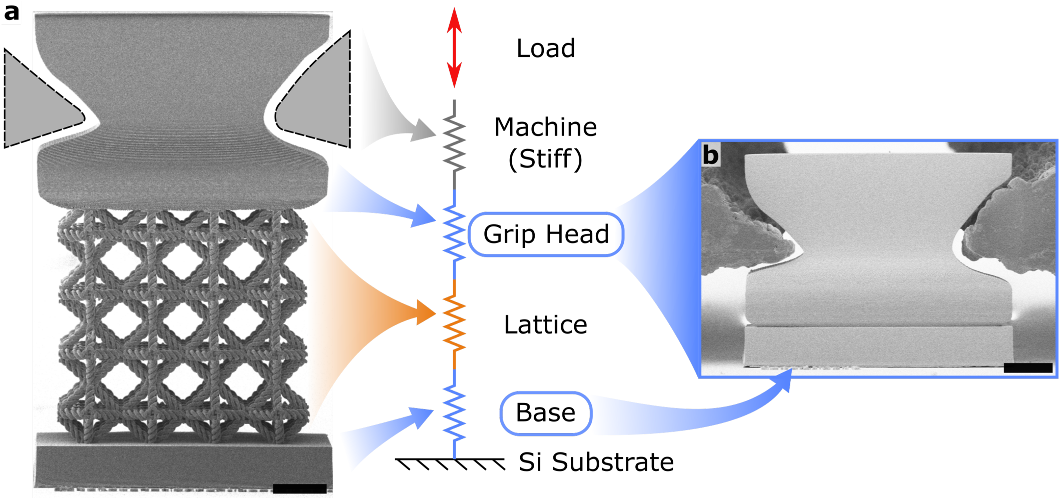

Figure 2.5: Lattice tension and tension-to-compression experimental set up. a) Mechanical representation of the experimental set-up for in situ tension and tension-to-compression experiments. b) Testing set-up to measure the stiffness of the IP-Dip grip head and base. The grip head shown in both images was designed for tension-to-compression experiment of octahedron samples. Scale bars are 25 μm.

$K_{eff} = \frac{1}{(C_{grip}+C_{base})}$,

$$u_{lat} = u_{total} - \left(\frac{1}{K_{eff}} \cdot Load\right) . \tag{2.3}$$

As shown in Figure 2.5, the stiffness of the combined grip head and base was measured by loading the grip head and base alone without any lattice (or pillar) in between. There are three different grip categories: grips for tension-to-compression lattice experiments, tension-only lattice experiments, and tension-only IP-Dip pillar experiments. Each grip category for lattices consists of one grip design for octahedron lattices and one for diamond lattices; there are a total of five grip designs in this work. Each unit cell configuration merits its own grip design because the grip is susceptible to printing failure in regions where it is not connected to the beams of the lattice underneath it (Figure 2.6). We have measured the stiffness of each grip design and obtained K_{eff} values ranging from 9.7 to 16.8 kN m^{-1} depending on which unit cell and loading configuration the lattice grip head was designed for. For pillar samples, the average K_{eff} value was 3.7 kN m^{-1}.

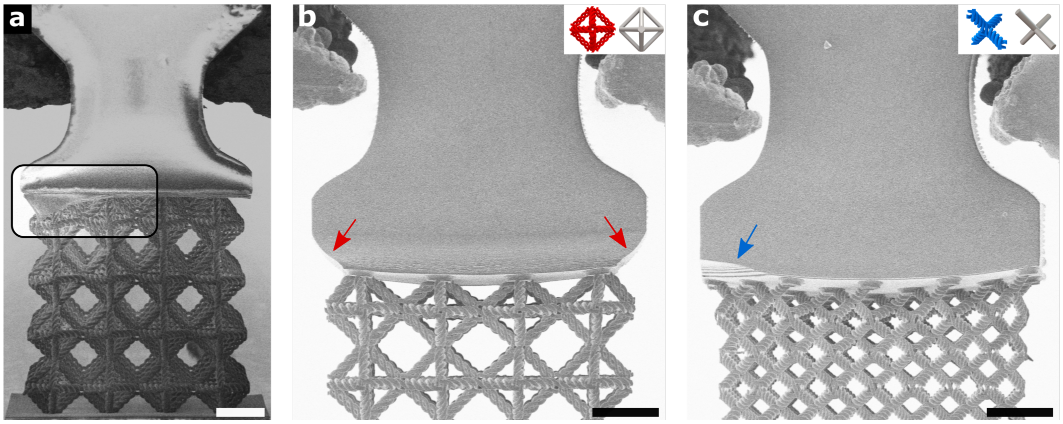

Figure 2.6: Grip design for each unit cell architecture. a) Printing failure shown in a grip head designed for tension-only experiments. For each unit cell architecture, the region of the grip where the grip meets the sample was customized to prevent printing failure. Red and blue arrows point to major differences between grips intended for b) octahedron and c) diamond unit cell architectures, respectively. Scale bars are 25 μm.

2.3 UV Irradiation

We observed variability in some of our lattices pulled in tension in Chapter 3 that had prolonged UV light exposure. While one out of every three samples tested in tension for each architecture and unit cell configuration was tested within three days after fabrication, the other two samples were tested within four to five months after fabrication. The delay in testing may have led to increased cross-linking of IP-Dip due to UV light exposure over an extended amount of time [66]. Interestingly, the only type of architecture that produced a considerable change in response due to delay in testing was monolithic octahedron, where $\sigma_{t,f}$ increased but $\varepsilon_{t,f}$ did not noticeably change (see Figure 3.2a,b). Note that the monolithic octahedron architecture is the only lattice type in this work that does not have a non-rigid hierarchy whether in the unit cell-level or beam-level, and it is safe to assume that the r/L value (which corresponds to $\bar{\rho} \cong 5$) is low enough such that the architecture is still stretching-dominated [37, 38].

In Chapter 4, we used a Spectro UV lamp model ENF-240C (120 V, 60 Hz, 0.2 Amp) set to the short wave setting (wavelength 254 nm, UV-C radiation) at a distance of maximally 5 cm from the top of the sample to perform UV-irradiation on our samples. One set of rhombus frames and pillars combined was fabricated in one batch (i.e., on one Si substrate within one printing run), and some of the rhombus frames and pillars were tested in tension within seven days from fabrication. Rhombus frames and pillars that had not undergone mechanical testing were then UV-irradiated for 5 hr and some of them underwent mechanical testing. The rest of the untested rhombus frames in the same batch were then UV-irradiated for an additional 24 hr and were marked as 29-hr UV-irradiated samples. Pillars marked as 29-hr UV-irradiated samples came from a separate set of pillars that underwent UV-irradiation for 29 continuous hours. UV-irradiation was performed within eight days from the previous fabrication/post-processing step, and mechanical testing was performed within two days of UV-irradiation.

2.4 Numerical Methods

Simulation results in Figure 3.4e,f, were obtained via linear perturbation simulations of a 3-fiber cantilever woven strut with varying geometric parameters. Each fiber was constrained to undergo one full rotation (i.e., the pitch was the same as the strut length L), and the effective beam radius was solved to attain a given solid volume (determined by a choice of fiber radius and a comparison monolithic beam). The fibers were meshed using 10-node quadratic tetrahedral elements (C3D10), with a minimum of 4 elements across the fiber diameter, corresponding to 3,000–24,000 elements per fiber depending on geometric features. The DOFs of the nodes on one side of the fibers were fixed, while the DOFs on the opposite side were coupled to a single dummy node for all three fibers. A displacement was then imposed on the dummy node, as shown in Figure 3.4e,f, for the stretching and bending cases. The normalized effective axial and bending stiffnesses were computed by dividing the reaction force at the dummy node by the displacement amplitude, and then normalizing by EL, where E is the Young's modulus. To directly compare to their monolithic counterparts, these normalized effective axial and bending stiffnesses were divided by the corresponding normalized stiffnesses of the monolithic beams, and are presented as surface plots in Figure 3.4e,f.

Chapter 3

MECHANICAL CHARACTERIZATION OF HIERARCHICAL WOVEN LATTICES

This chapter is adapted from:

W.P. Moestopo, A.J. Mateos, R.M. Fuller, J.R. Greer, & C.M. Portela. "Pushing and Pulling on Ropes: Hierarchical Woven Materials". *Advanced Science* **7**, 20, (2020).

Contributions: Participated in the conception of the project, designed and fabricated the samples, conducted the experiments, analyzed the data, and wrote the manuscript.

3.1 Chapter Summary

Hierarchy in natural and synthetic materials has been shown to grant these architected materials properties unattainable independently by their constituent materials. While exceptional mechanical properties such as extreme resilience and high deformability have been realized in many human-made three-dimensional (3D) architected materials using beam-and-junction-based architectures, stress concentrations and constraints induced by the junctions limit their mechanical performance. A new type of hierarchical architecture in which fibers are interwoven to construct effective beams is presented. In situ tension and compression experiments of additively manufactured woven and monolithic lattices with 30-µm unit cells demonstrate the superior ability of woven architectures to achieve high tensile and compressive strains (>50%)—without failure events—via smooth reconfiguration of woven microfibers in the effective beams and junctions. Cyclic compression experiments reveal that woven lattices accrue less damage compared to lattices with monolithic beams. Structural redundancy, from having multiple fibers in an effective beam, also showed the potential for woven microlattices to elongate further after ultimate tensile failure points were reached. Through finite element models, maps of axial and bending stiffnesses of woven beams with varying geometric parameters present new design spaces to develop architected materials with tailored compli-

ance that is unachievable by similarly configured monolithic-beam architectures. The demonstrated capabilities of woven hierarchical architecture offers a pathway to make traditionally stiff and brittle materials more deformable, thus making it a great candidate for materials in high-deformation or load-sensitive systems. Contact interaction between fibers in effective beams and junctions offers a building block for materials with complex nonlinear mechanics such as selective damping.

3.2 Introduction: Searching for Architected Materials with High Deformability and Hierarchical Design

Materials with hierarchy are abundant in nature, and their combination of structural hierarchy at different length scales gives rise to bulk properties unattainable independently by their constituent materials [1]. While architectural hierarchy has been shown to enhance damage tolerance such as in mantis shrimp claw and elk antler bone [67, 68], hierarchical structures in bone and nacre lead to fracture toughness values that are higher than their respective building blocks [1, 69, 70]. Advances in fabrication methods have enabled the creation of synthetic materials with similar structural hierarchy down to the micro- or nanometer scale, leading to desirable properties such as extreme resilience and high deformability [9, 71, 72]. Beyond static mechanical properties, hierarchical architected materials have also opened up new material properties such as tunable ultrasonic band gaps [73, 74], ultralow or tunable thermal response [8, 75, 76], and impact resistance [77].

Despite this broad property space enabled by structural hierarchy, most three-dimensional (3D) synthetic architected materials have drawn from beam-and-junction-based design principles [6, 9, 23, 78]. These types of designs have been studied extensively both experimentally and computationally [37, 79, 80], and are characterized for their high stiffness- or strength-to-weight ratios. Even with enabling these properties, the presence of nodes has been identified to be detrimental in some cases, particularly at higher relative densities (i.e., fill fractions) where nominally stretching-dominated architectures (as defined by the kinematic rigidity of the unit cells) [31] exhibit a less-desirable bending-dominated response [37, 38]. These materials are appealing in a number of applications where maximal linear mechanical properties are required, but lose their optimality in large deformations due to their failure mechanisms and constrained kinematics. In particular, few architected materials made of materials stiffer than elastomers have been reported to withstand deformations greater than 20% strain [7, 81], and most of them fail catastrophically or accumulate significant damage [5, 8, 82, 83]. The geometries in these materials lead to stress concentration at junctions or nodes where damage nucleates [8, 39, 84], commonly resulting in significantly weaker or compliant responses after the initial deformation. While higher stiffness- and strength-to-weight ratios can be achieved by choosing closed-cell, plate-based designs over beam-and-junction-based designs, the deformability of such architected materials is still limited [85–87]. As an alternative, architected materials that lack junctions or nodes, such as triply periodic minimal surface and stochastic spinodal shell designs [40, 81, 88, 89], more evenly distribute stresses throughout their components but have not yet enabled repeatable large deformations without significant degradation except for designs with very low material fill fraction [90]. Wire-woven architected materials have recently been reported to have desirable energy absorption capabilities and buckling suppression [45, 47], presenting a potential approach to enable repeatable deformability, but have lacked the introduction of hierarchy to further enhance these properties.

3.3 Design and Fabrication of Hierarchical Woven Lattices

Here, we present a new type of hierarchy in lattice architectures that consists of weaving structural components to assemble an effective beam, replacing the classical monolithic- or hollow-beam design (Figure 3.1) [6, 9]. Using these hierarchical woven beams as building blocks in a periodic unit cell, of the same type as their monolithic and hollow counterparts, results in woven lattice architectures. At the effective beam junctions (i.e., nodes) of woven lattices, fibers are not combined to form monolithic junctions but are instead interwoven into adjacent beams. Since these woven lattice architectures open up many previously unexplored design spaces in fiber geometry and connectivity, we fixed certain design parameters to allow a systematic study of their mechanical response. For instance, each woven beam of length L is designed to consist of three fibers, which are woven in the form of a full helical rotation with pitch $\lambda = L$, that extend beyond a given beam to also make up the three closest neighboring woven beams (Figure 3.1a). In this work, we design, fabricate, and compare the mechanical response of woven and monolithic lattices of two common unit-cell configurations: (i) the kinematically rigid octahedron, and (ii) the non-rigid diamond unit cell. To understand the fundamental effect of fiber geometry on the mechanical properties, we also perform numerical studies on the axial and bending stiffnesses of woven beams with varying geometric parameters while maintaining constant relative density (i.e., fill fraction).

The samples were fabricated at the microscale using two-photon lithography out of acrylic-based polymer IP-Dip photoresist (Nanoscribe GmbH), which enabled

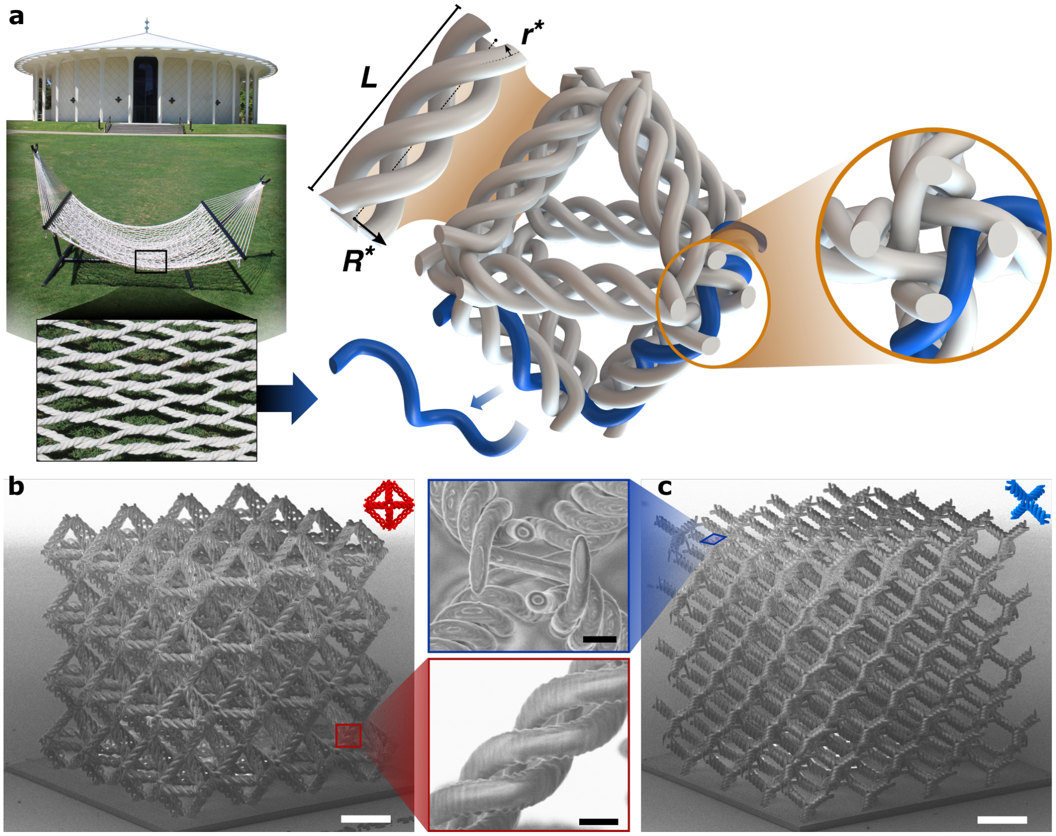

Figure 3.1: Design and realization of hierarchical micro-woven lattices, whose beam and junction geometries are analogous to woven ropes. a) Computer-aided design (CAD) images of the octahedron unit cell of a woven lattice showing non-intersecting fibers that form its beams and junctions. SEM images of the b) woven octahedron and c) woven diamond lattices ($\bar{\rho} \approx 5\%$) with their corresponding CAD representations, and detailed views of a woven beam and a junction in a woven diamond lattice. Scale bars in white correspond to 20 µm, and black bars in insets are 2 µm.

the creation of intricate fiber geometries with sub-micron radii r^*. These samples consisted of 4×4×4 tessellations of 30-µm unit cells, with intended relative densities $\bar{\rho}$ of 3.3% to 5% for diamond lattices and 5% to 8% for octahedron lattices. While the unit cell size was held constant, the fiber radius r^* and the beam radius R^* were designed to vary from 0.6 to 0.9 µm and 1.85 to 2.8 µm, respectively, to attain different relative densities. To enable tension-to-compression nanomechanical experiments, custom grips were fabricated on top of the woven lattices while a plate was used at the base of the samples to promote adhesion to the Si substrate. For comparison purposes, we also fabricated monolithic octahedron and diamond samples of identical tessellations and relative densities to the woven samples, with monolithic beam radii ranging from 1.2 to 1.8 µm.

3.4 Tension Experiments of Monolithic and Hierarchical Woven Lattices

3.4.1 Uniaxial Tension

We performed in situ uniaxial tension experiments on at least three samples per configuration, which showcased an enhanced extensibility of woven architectures compared to their monolithic beam-and-junction-based counterparts. For this comparative study, we chose the stiffest experimentally viable set of parameters for a woven lattice of a given $\bar{\rho}$ and unit cell configuration. Figure 3.2a,b show the tensile responses up to failure for woven and monolithic lattices at a relative density of $\bar{\rho} \approx 5\%$, with insets showing the progression of deformation along the experiments. These experiments show that woven lattices in tension attain a ~70–120% increase in strain at the point of ultimate failure compared to monolithic lattices, for both octahedron and diamond geometries, with the non-rigid diamond configuration exhibiting the largest average extensibility of 64% strain. The architectural redundancy from having three fibers in an effective beam—as opposed to a single continuous body—is also shown to allow woven lattices to elongate further upon ultimate failure instead of completely rupturing (Figure 3.2a.IV,b.IV and Figure 3.3). In addition, smooth structural reconfiguration through uncoiling and reorientation of fibers in the woven beams and junctions enabled enhanced elongation (Figure 3.2a.I-IV,b.I-IV). Woven lattices with octahedron unit cells (Figure 3.2, bold red) reached ultimate tensile failure strain $\varepsilon_{t,f}$ of 40.6 ± 1.0%, and ultimate tensile strength $\sigma_{t,f}$ of 515 ± 52 kPa, while woven lattices with diamond unit cells (Figure 3.2, bold blue) had $\varepsilon_{t,f}$ = 64 ± 9% and $\sigma_{t,f}$ = 277 ± 4 kPa. In comparison, monolithic samples resulted in $\varepsilon_{t,f}$ = 23.4 ± 0.7% and $\sigma_{t,f}$ = 1113 ± 206 kPa for the octahedron configuration, and $\varepsilon_{t,f}$ = 28.9 ± 0.6% and $\sigma_{t,f}$ = 759 ± 72 kPa for the diamond configuration.

3.4.2 Tension-to-Compression

To further showcase the versatility of these woven lattices, we performed continuous tension-to-compression experiments corresponding to absolute strain changes $\Delta\varepsilon$ of up to 118% without sample failure. Figure 3.2c presents a comparison between the woven octahedron and diamond geometries (both of $\bar{\rho} \approx 5\%$) undergoing quasi-static tension-to-compression deformation (corresponding movies are shown in Supplementary Movies 1 and 2 in Appendix A). Regions of maximum tension and maximum compression are designated by Regions 1 and 3 in Figure 3.2c, respectively. At maximum tensile strains (Region 1, Figure 3.2c) of 32% and 50% in the octahedron and diamond geometries, respectively—beyond $\varepsilon_{t,f}$ of each geometry's corresponding monolithic lattices—woven beams were observed to accommodate

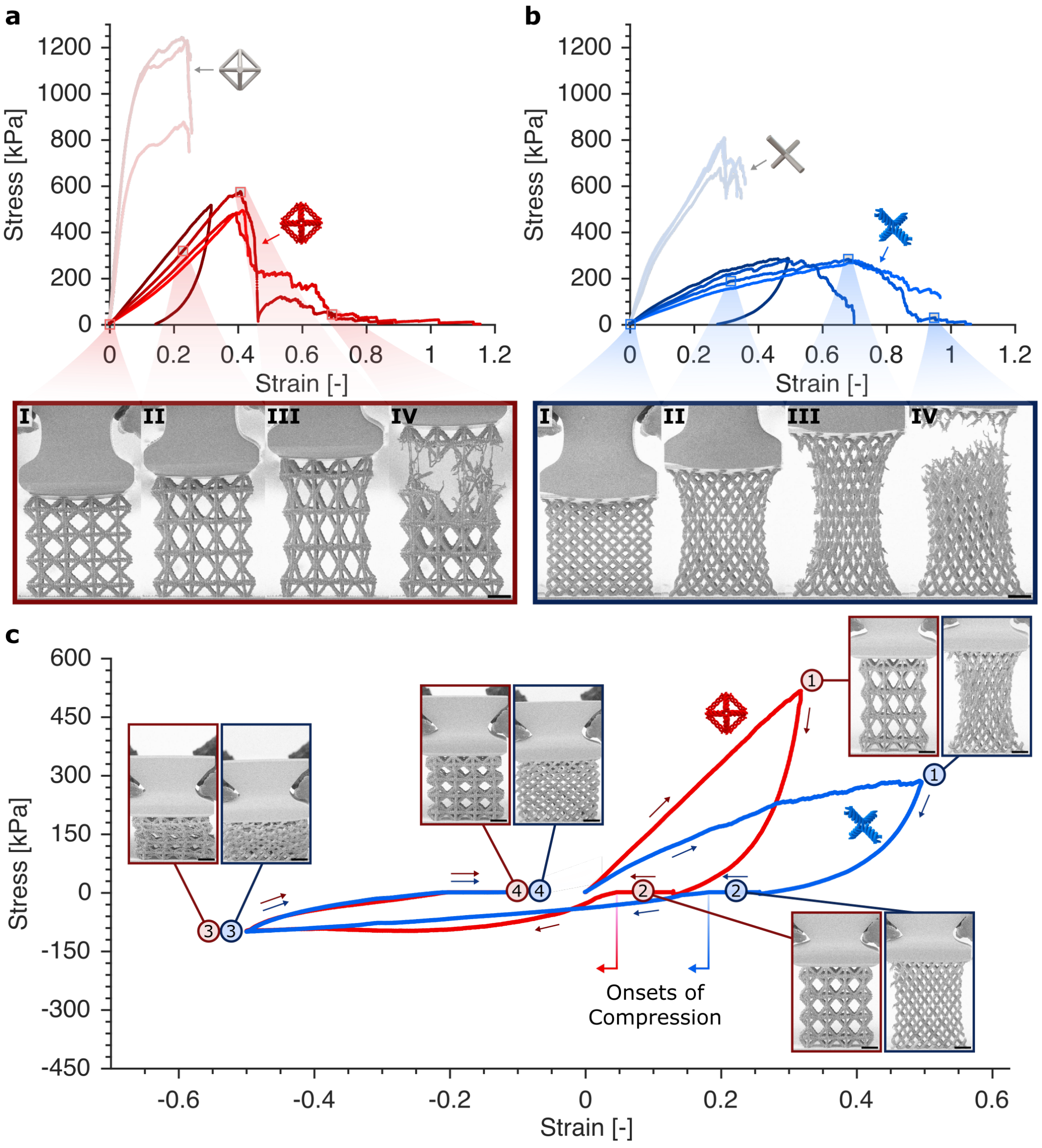

Figure 3.2: Tension experiments of woven and monolithic lattices ($\bar{\rho} \approx 5\%$), and combined tension-to-compression experiments of woven lattices. Tensile responses of woven and monolithic lattices with a) rigid, octahedron and b) non-rigid, diamond unit cell configurations loaded up to failure. Red and blue data points correspond to octahedron and diamond configurations, respectively. Faint colors indicate monolithic lattices, and bold colors are for woven lattices, with the boldest showing the tensile portion of the tension-to-compression data in (c). Insets show still frames from two tensile experiments (one for each woven architecture) corresponding to locations in the graphs. c) Tension-to-compression experiments of woven octahedron and diamond lattices with insets for each labeled region. Scale bars correspond to 25 μm.

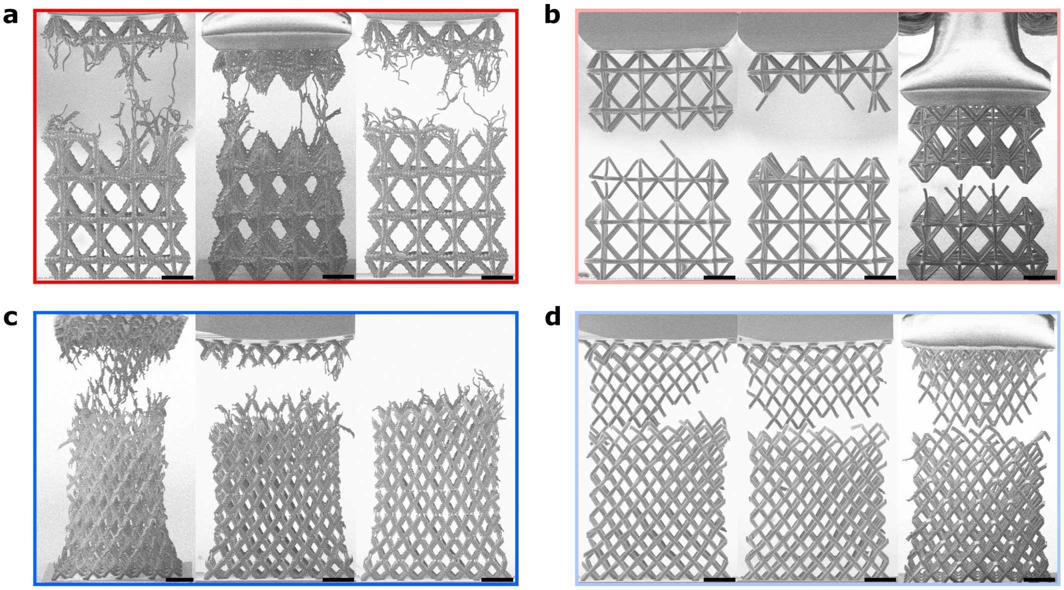

Figure 3.3: Fractographs of woven and monolithic lattices ($\bar{\rho} \approx 5\%$) loaded in tension: a) woven octahedron, b) monolithic octahedron, c) woven diamond, and d) monolithic diamond lattices. Scale bars are 25 μm.

for the Poisson effect by reorienting and uncoiling in the direction of applied load. Plateaus in Regions 2 and 4 correspond to transitions between strain type (i.e., tension or compression), where the indenter tip was not in contact with the top or bottom edges of the printed grip on top of the lattice. Upon full tensile unloading (end of Region 2), the viscoelastic response of IP-Dip accelerated the onset of compression (see Figure 2.4), which is indicated by an arrow corresponding to each woven lattice geometry. Smooth reorientation of beams was again observed at the maximum compression point (Region 3), accommodating for deformation without significant permanent damage. As in the tensile unloading region, the compressive unloading region (Region 4) came with a concomitant viscoelastic response.

3.5 Mechanical Behaviors Under Cyclic Loading

3.5.1 Cyclic Compression

We probed the response of woven lattices upon repeated deformation by performing additional cyclic compression experiments to 35% strain while comparing them to monolithic samples of both octahedron and diamond geometries. The response of each monolithic configuration was characterized by catastrophic failure events or significant plastic buckling in the first cycle, resulting in drastically different subsequent cycles due to accumulated damage (Figure 3.4a,b). In contrast, the woven octahedron and diamond samples had more self-similar loading cycles despite a pronounced viscoelastic effect, exhibiting no beam or fiber failure after ten cycles. To quantify their mechanical resilience, we calculated the dissipated energy density per i-th compression, ΔU_i, as the area enclosed by each stress (σ) vs. strain (ε) cycle,

$$\Delta U_i = \oint \sigma \, d\varepsilon, \tag{3.1}$$

and report the first-cycle-normalized quantities Π_i, defined as

$$\Pi_i = \frac{\Delta U_i}{\Delta U_1}. \tag{3.2}$$

Figure 3.4c shows that by the end of the tenth cycle, the normalized energy absorption values for woven lattices with $\bar{\rho} \approx 5\%$ settled at 24–30%, values ~2–3 times higher than those for monolithic lattices of the same unit cell configurations. Although for woven lattices these normalized energy absorption values correspond to less than 3 kJ m^{-3} in absolute absorbed energy densities W_{abs} and less than half the W_{abs} for monolithic lattices (Figure 3.1), the average W_{abs} for woven lattices in tension-to-failure experiments differs by no more than 10–35% of the average W_{abs} for monolithic lattices (Figure 3.6). In addition, the evolution of effective Young's modulus per cycle in Figure 3.4d shows that the effective moduli for woven configurations settled after ~3 cycles (see Figure 3.7 for cyclic compression of lattices with different relative densities). Higher tenth-cycle energy values, and this early settling of the effective Young's modulus, indicate that woven lattices accrued less damage during cyclic loading. These cyclic compressions also show that octahedron lattices generally had lower normalized energy values compared to diamond lattices for both woven and monolithic configurations, despite having first-cycle absolute energy absorption values that were 39% and 135% higher for woven and monolithic configurations, respectively.

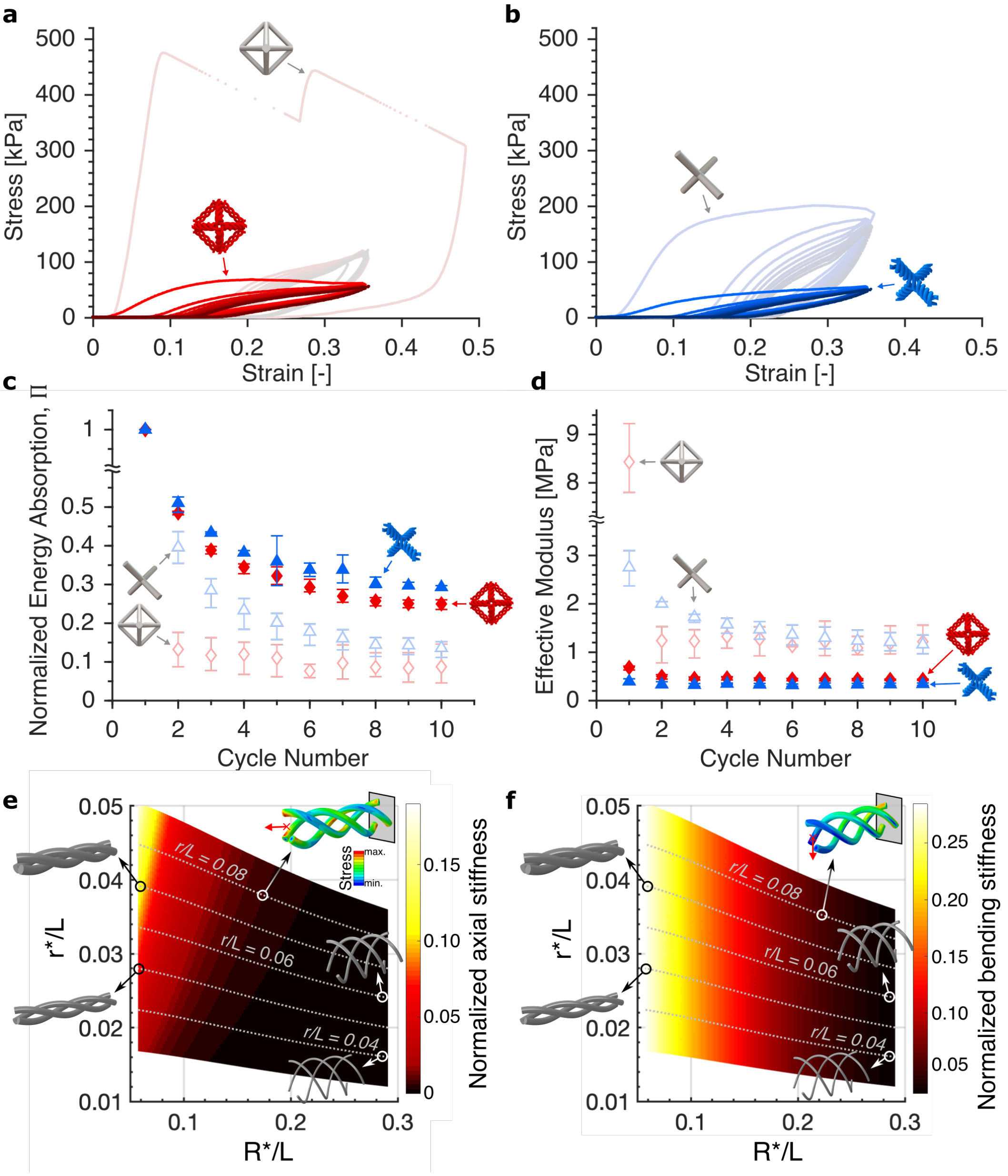

Figure 3.4: Compression responses and numerical studies of woven and monolithic architectures. Representative mechanical responses from cyclic compression of a) octahedron and b) diamond lattices ($\bar{\rho} \approx 5\%$) of both woven and monolithic architectures for ten cycles. Darker color represents a later cycle. c) Normalized energy absorption of each lattice architecture as a function of load-unload cycle showing higher resiliency for woven lattices. d) Effective modulus of each lattice architecture as a function of load-unload cycle. Error bars indicate the extrema of the data sets. Numerical studies on e) axial and f) bending stiffnesses of woven beams as functions of woven beam dimensionless geometric parameters r^*/L and R^*/L. The dashed grey lines represent constant-volume paths corresponding to the volume of a given monolithic strut with slenderness r/L. Woven-beam stiffnesses were normalized by those of the corresponding equal-volume monolithic strut, showing the ability of woven architecture to reach higher compliance and decouple variations in axial and bending stiffnesses.

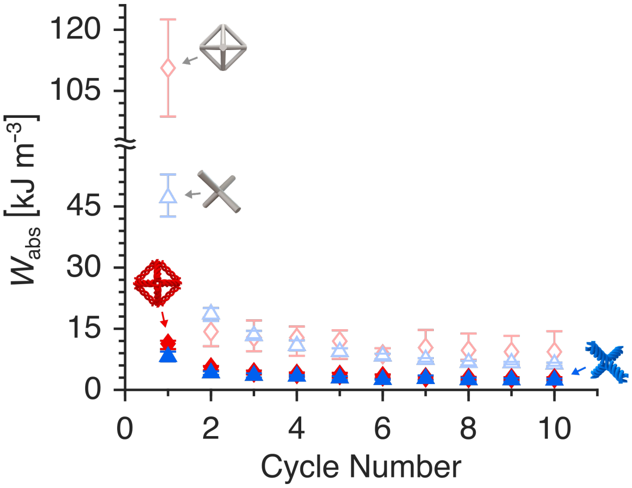

Figure 3.5: Absolute absorbed energy densities (W_{abs}) of lattices in Figure 3.4a–d as a function of load-unload cycle. Error bars indicate the extrema of the data sets.

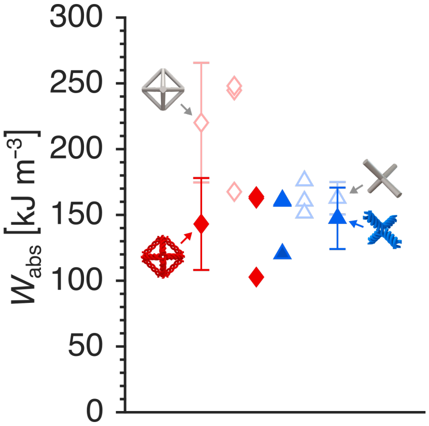

Figure 3.6: Absolute absorbed energy densities (W_{abs}) of lattices loaded in tension up to failure as shown in Figure 3.2a,b. Error bars represent the standard deviation of the data sets.

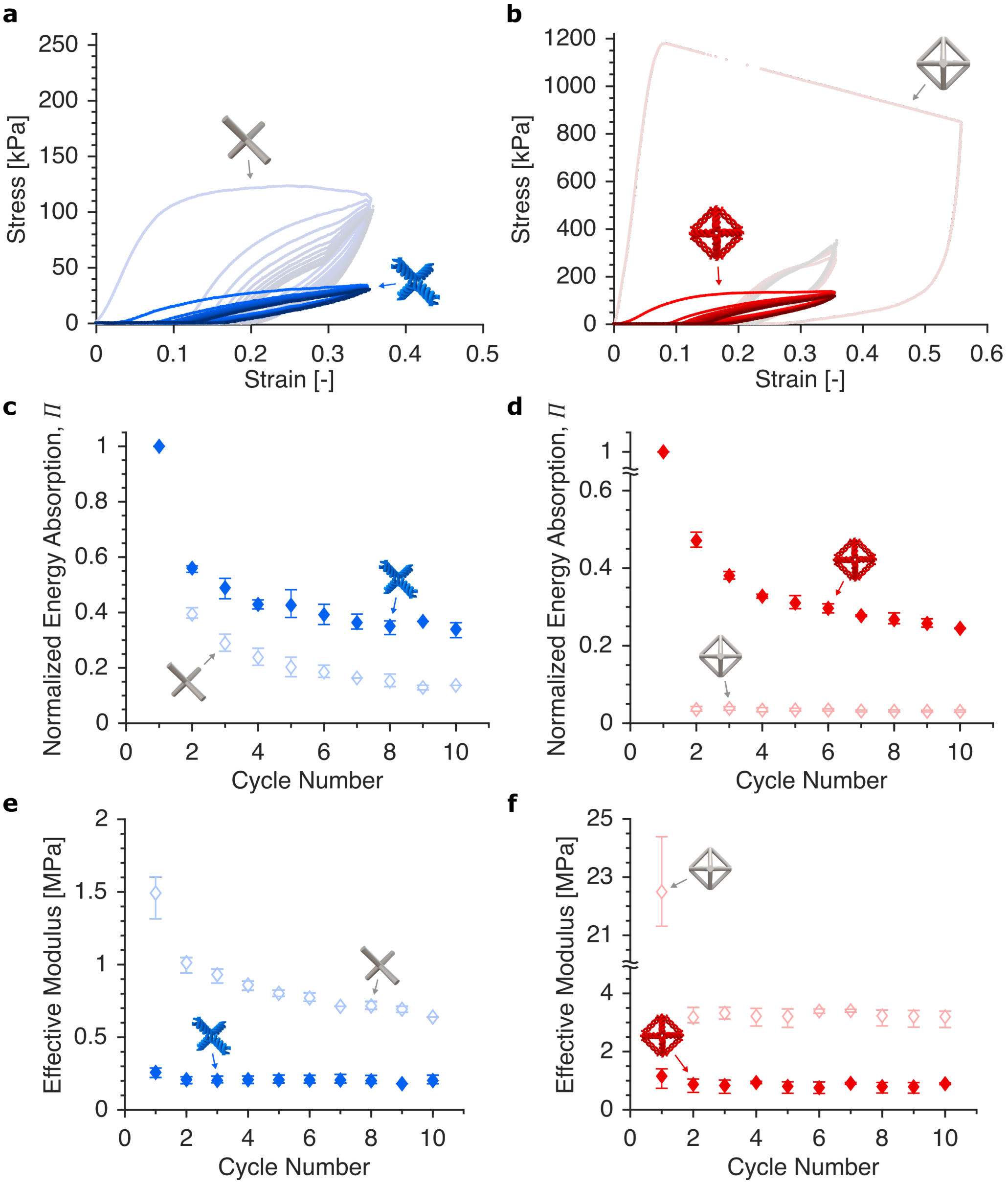

Figure 3.7: Representative cyclic compression responses and the calculated mechanical properties of woven and monolithic (a, c, e) diamond lattices with $\bar{\rho} \approx 3.3\%$, and (b, d, f) octahedron lattices with $\bar{\rho} \approx 8\%$. Error bars indicate the extrema of the data sets. Faint colors indicate monolithic lattices, and bold colors are for woven lattices. Darker color in a,b indicates a later cycle.

3.5.2 Cyclic Tension

To further explore the energy absorption capability of woven lattices in tension, we performed additional cyclic tensile experiments on woven octahedron and diamond lattices up to five cycles (Figure 3.8). We tested one woven octahedron lattice ($\bar{\rho} \approx 5\%$) up to 26% strain and one woven diamond lattice of the same relative density up to 40% strain, which corresponded to ~62–65% of each lattice's average ultimate failure strain. Lattice geometry was observed to play a minor role since the added compliance in the diamond lattice was offset by an increased extensibility compared to the octahedron lattice, resulting in almost identical absolute energy absorption values. Direct comparison of the energy densities in Figure 3.5 (compression) and Figure 3.8c (tension) shows that the woven octahedron lattice can attain higher absorbed energy densities in tension throughout 5 cycles, despite being deformed to lower strains.

Unlike the trend seen in Figure 3.4d, Figure 3.8b shows that for both lattices, there was an increase in stiffness in subsequent cycles. In the corresponding movies shown in Supplementary Movies 3 and 4 (Appendix A), smooth reorientation of the beams can be observed during loading, but the beams had not fully returned to their initial configuration before the next cycle began. Since in the beginning of the subsequent cycle the beams were more aligned toward the loading direction compared to the previous cycle, the calculated effective modulus for the subsequent cycle understandably became higher than the calculated value from the previous cycle.

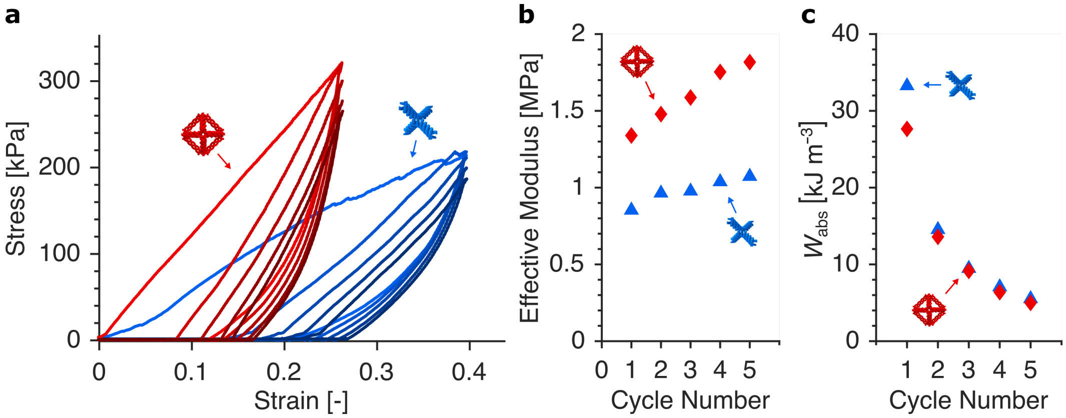

Figure 3.8: Cyclic tension responses of woven architectures. a) Mechanical responses from cyclically loading a woven octahedron and a woven diamond lattice ($\bar{\rho} \approx 5\%$) up to five cycles. Darker color represents a later cycle. b) Effective modulus of each lattice as a function of load-unload cycle. c) Absolute absorbed energy density (W_{abs}) of each lattice as a function of load-unload cycle.

3.6 Numerical Investigation

Besides improving the extensibility and minimizing the mechanical degradation of the architectures, woven hierarchy enables linear mechanical properties that are unachievable using monolithic geometries, such as those desired in materials for flexible electronics or wearable devices [91, 92]. We explored the range of properties enabled by this type of hierarchy by performing a numerical study on the woven-beam component that makes up these architectures. Using the finite element method, we computed maps of axial and bending stiffnesses of a cantilever woven beam as a function of (i) the ratio between the effective beam radius and beam length, R^*/L, and (ii) the ratio between the fiber radius and beam length, r^*/L. For comparison to its monolithic counterpart, the computed woven stiffnesses were normalized by the corresponding stiffnesses of a monolithic cantilever beam with the same material volume and length (Figure 3.4e,f). The stress contours in these simulations indicate that woven beams are inherently bending-dominated, implying that unit cell architecture and kinematic rigidity should play a minor role in the linear mechanical response. This explains the similarity in modulus and energy absorption for the woven octahedron and diamond configurations, since both are bending-dominated, opposite of what is expected and observed for rigid and non-rigid monolithic configurations. In addition to introducing bending deformation, woven hierarchy also allows the transition from catastrophic to non-catastrophic failure in the octahedron geometry by mitigating stress concentration at nodes. Since failure stresses are not reached at nodes anymore, the added compliance of woven nodes facilitates beam alignment in the direction of the applied load, which together with uncoiling of helical fibers enables the observed extreme extensibility. The stiffness maps also exhibit a markedly different evolution of stretching and bending stiffnesses as functions of r^*/L and R^*/L, where normalized stretching stiffness increases while normalized bending stiffness stays relatively constant as r^*/L rises on a given R^*/L. The decoupling of the beam's axial and bending stiffnesses via woven architecture opens up new ways to prescribe directional compliance in an architected material that are inaccessible to classical beam-and-junction-based designs [93].

3.7 Comparison to Previously Reported Architected Materials

The ability to increase the compliance and deformability of a given material is intriguing as it opens up possibilities to incorporate stiff and brittle materials in high-deformation and load-sensitive applications [91]. Early successes have been shown in the field of stretchable electronics, where researchers have incorporated thin and wavy planar architectures to allow a considerable amount of stretching, bending, and twisting in devices containing brittle silicon. Yet such pronounced deformability is not easily attainable for thick materials of arbitrary shapes; increasing the tensile failure strain of a given material via 3D architecture has proven to be a non-trivial task, as evidenced by recent works on metallic and polymeric bending-dominated foams which counterintuitively achieved a lower tensile failure strain than their constituent materials [94]. As an alternative to the stochastic structures present in foams, woven hierarchy provides one method to achieve extensibility beyond that of the constituent materials, in addition to an already superior extensibility compared to other periodic architected materials (Figure 3.10a,b) [7, 39, 95, 96].

To allow comparison across architectures and materials (Figure 3.10b), we define a normalized tensile stress at failure $\bar{\sigma}_{t,f}$ as the tensile stress at failure $\sigma_{t,f}$ normalized by the relative density of the architected material and the tensile strength of the constituent material σ_s, and we simply define a normalized tensile strain at failure $\bar{\varepsilon}_{t,f}$ as the tensile strain at failure $\varepsilon_{t,f}$ normalized by the maximum tensile strain of the constituent material ε_s. We determine the mechanical properties of the constituent IP-Dip by performing tension experiments up to failure on three IP-Dip pillars with average sample height of 69.90 ± 0.15 μm and average sample diameter of 13.43 ± 0.03 μm (see Figure 3.9 and Supplementary Movie 5 in Appendix A). As with lattice experiments, the displacement data from the experiments were corrected accordingly by taking into account the compliance of the IP-Dip grip heads and bases. We observed yielding behaviors and obtained the following material properties: tensile stress at failure, $\sigma_{t,f}$ = 84.2 ± 4.1 MPa, tensile strain at failure, $\varepsilon_{t,f}$ = 33.7 ± 2.0%, Young's Modulus = 1.49 ± 0.34 GPa, and yield stress, σ_{yield} = 26.8 ± 5.9 MPa, which was determined via 0.2% yield offset of the engineering stress-strain curves.

We now compare the mechanical properties of our IP-Dip pillars to reported values of pillars with similar dimensions and predicted "degree of conversion" (DC), which is a measure of the amount of polymer chain cross-linking as described in Reference [97]. Compared to a pillar tested in tension with DC of 23%, our pillars had comparable Young's Modulus (1.49 GPa vs 1.5 GPa) and lower $\sigma_{t,f}$ (84.2 MPa vs 115 MPa), which may have resulted from having a larger hatching distance (i.e., distance between printed lines in a layer) during the printing of our pillars. When compared to pillars of similar printing parameters that were tested in

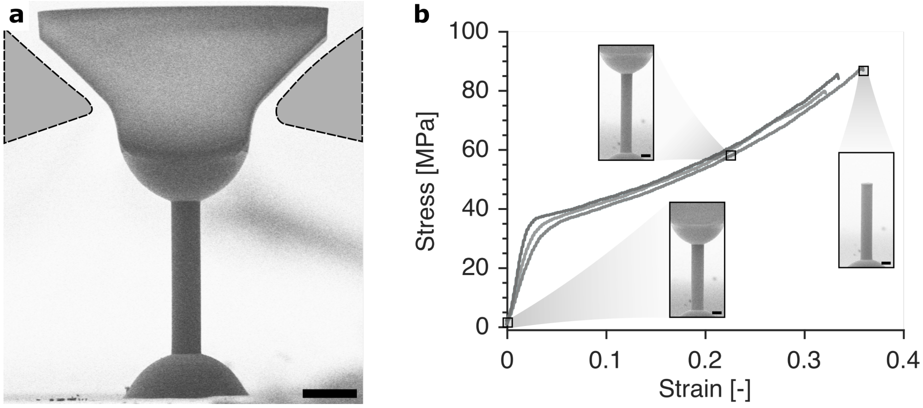

Figure 3.9: Tensile testing of IP-Dip pillars. a) Micrograph showing a pillar with an attached custom grip for tensile testing. b) Mechanical responses of pillars tested to determine the mechanical properties of IP-Dip in this study. Scale bars in a) and b) are 25 µm and 10 µm, respectively.

compression, our pillars had lower σ_{yield} and Young's Modulus (72 MPa and 2.68 GPa, respectively), corresponding to a less than 3% elastic elastic limit [38]. In Chapter 4, we show tension testing of IP-Dip pillars that are more similar in size and fabrication parameters to the constituent fibers in this chapter. These pillars have smoother edges at their interface with the top and bottom supports, and they show higher load levels for a given strain and ~44% larger tensile strain at failure.

After determining the σ_s and ε_s of the constitutive material in our lattices by testing IP-Dip pillars in tension (see Figure 3.9 and Supplementary Movie 5 in Appendix A), we arrived at normalized failure strength and strain values for comparison to other reported architected materials [95, 98–101]. An initial comparison between the samples in our study shows that the tensile failure strain $\varepsilon_{t,f}$ of IP-Dip monolithic octahedron and diamond lattices were lower than that of IP-Dip pillars, whereas woven IP-Dip lattices were able to deform past the tensile failure strain of IP-Dip, with the diamond configuration deforming up to 73% strain. Compared to the most extensible non-elastomeric architected material in literature, IP-Dip lattices in this work attained 5–25 times higher tensile strength while also outperforming its extensibility by more than 5% and up to 221%. Beyond merely joining a special class of architected materials that can elongate farther than their constituent materials, the woven lattices presented in this work achieve this feat while providing an alternate and wider design parameter space via their added compliance and the tunability of their effective beams' axial and bending stiffnesses; an even higher elongation of woven lattices with equal mass could potentially be achieved by opting for larger fiber arc lengths and more separation between each fiber.

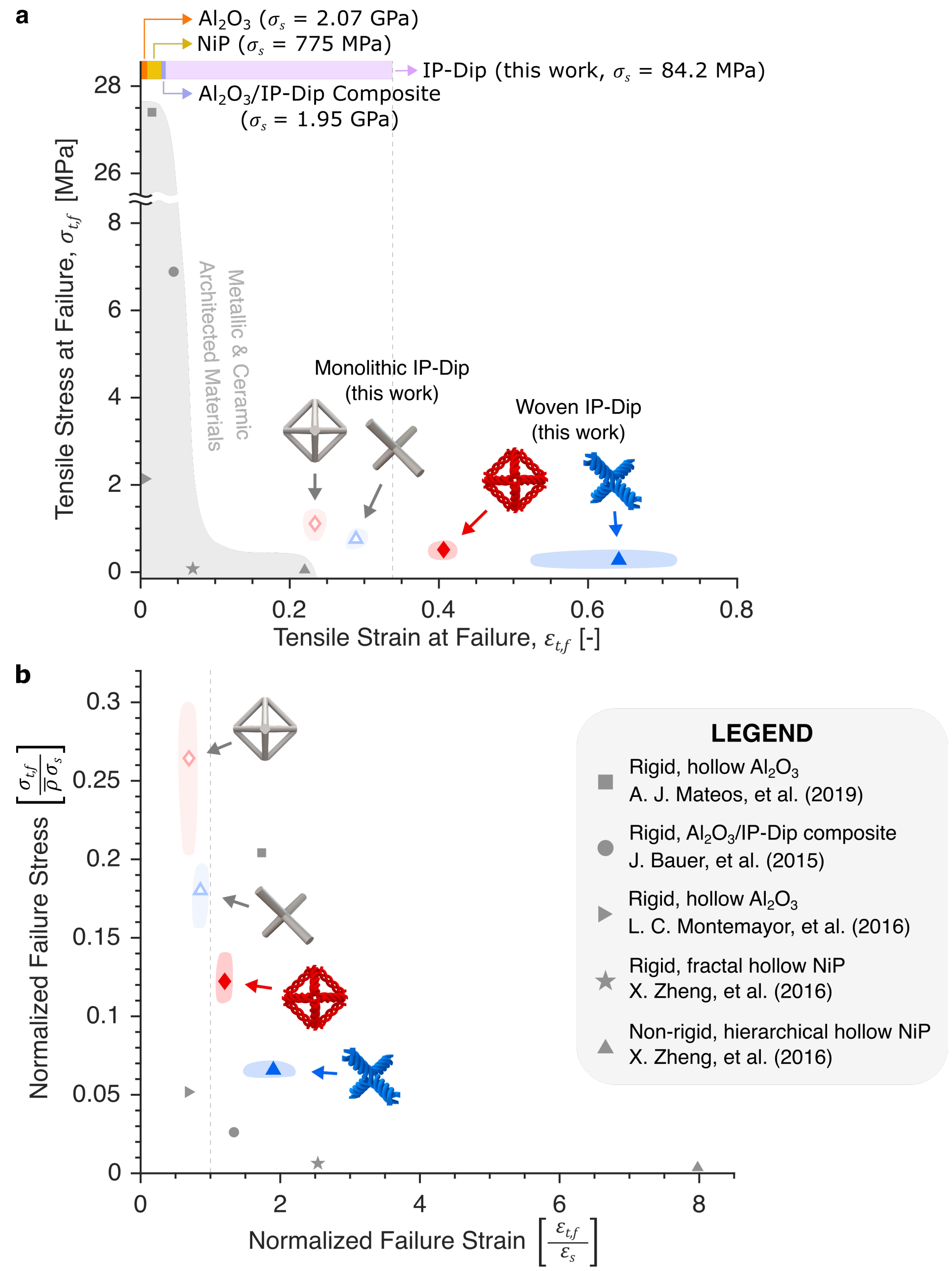

Figure 3.10: Performance comparison between lattices in this work and other architected materials in literature. a) Tensile stress at failure $\sigma_{t,f}$ versus elongation to failure $\varepsilon_{t,f}$ of woven and monolithic IP-Dip lattices in Figure 3.2a,b compared to other architected materials. The bars at the top of the graph show the maximum tensile strains ε_s of the relevant constituent materials. b) Normalized tensile stress at failure $\bar{\sigma}_{t,f}$) versus normalized tensile strain at failure $\bar{\varepsilon}_{t,f}$) of architected materials in a). The failure strain $\varepsilon_{t,f}$ for Reference [39] was measured from video of experiment. The constituent material strength σ_s for Al_2O_3 and NiP were calculated by taking the average of the values reported in References [98] and [100], respectively. An estimate in Reference [101] was used for ε_s of Al_2O_3, while ε_s of NiP was taken from the reported value in Reference [99]. For the Al_2O_3/IP-Dip composite, the ε_s was calculated by dividing the average alumina fracture stress with the average elastic modulus of the alumina reported in Reference [95] along with the σ_s.

Chapter 4

INFLUENCE OF TOPOLOGY AND CONSTITUENT MATERIALS IN HIERARCHICAL INTERTWINED STRUCTURES

This chapter is adapted from:

W.P. Moestopo, S. Shaker, & J.R. Greer. "Knots are Not for Naught: Design, Properties, and Topology of Intertwined Micro-Architected Materials". In preparation.
Contributions: Conceived the project, designed and fabricated the samples, conducted the experiments, analyzed the data, and wrote the manuscript.

4.1 Chapter Summary

A close look into natural materials reveals various architectures hierarchically ordered to achieve multifunctionality, yet most human-made three-dimensional (3D) hierarchical materials are designed with interconnected structural members whose junctions induce deformation constraints and stress concentrations. We weave the concept of knots into a hierarchical architecture framework, study how fiber topology and constituent materials influence the mechanical behaviors of hierarchical intertwined structures, and compare our results with theory. Tensile experiments of microscale additively manufactured structures reveal that knot topology allows a new regime of deformation capable of shape-retention, leading to ~92% increase in absorbed energy and up to ~107% increase in failure strain compared to woven structures. By varying the bulk and surface properties of the polymeric constituent materials in hierarchical intertwined structures via passivation and UV-irradiation, we find that the extensibility of the constituent material is crucial in the early stage of structural deformation and becomes less so in subsequent stages. Agreements between experimental results and a model for long overhand knots suggest that the model can aid the optimization of the mechanical performance of microwoven materials, although further exploration is necessary to accurately model the effects of material and nodal geometrical properties on the deformation and energy absorption

mechanisms in hierarchical intertwined materials. The unique tightening mechanism demonstrated in this work unlocks new ways to create shape-reconfigurable, highly extensible, and extremely energy absorbing bulk, 3D architected materials with mechanical properties that can be tuned not only by their geometries and bulk properties, but also by the surface interactions experienced by the structural elements. Such capabilities can be highly advantageous in applications such as flexible electronics and medical devices where repeated large deformations are encountered and traditionally stiff and brittle constituent materials still need to be incorporated.

4.2 Introduction: Beyond Architected Materials with Interconnected Structural Members

Many naturally formed composites are able to attain unique mechanical properties, such as high strength and fracture toughness, that surpass the performance of individual components by utilizing intricate hierarchical ordering [1]. Architectural hierarchy has been known to allow the activation of multi-scale toughening mechanisms in bone and enhance the structural stability of hexactinellid sponges [69, 102–105]. Attaining full hierarchical ordering of natural materials remains a challenge; progress has been enabled by modern fabrication methods capable of manufacturing synthetic materials with complex prescribed geometries and multiple orders of hierarchy [4, 5, 7, 106]. Precisely architected arrangements of constituent materials have led to unique material properties including photonic and acoustic band gaps [11, 107], tunable thermal response [16], and impact resistance [108, 109]. Incorporating hierarchy into synthetic architected materials, such as by forming structural elements out of beams at a distinctly smaller length scale, has also enabled other desirable mechanical properties, namely high energy absorption and deterministic failure behavior [9, 23]. As advancements in manufacturing techniques continue to expand the available design space, hierarchical architected materials have mostly drawn from interconnected design principles where structural members are fused together at their junctions [23, 110–113], such as beam-based lattices whose members are composed of periodic unit cells [7, 9]. Extensive experimental, computational, and analytical studies have been conducted on periodic architected materials (e.g., beam-based, plate-based, triply periodic minimal surface lattices) and non-periodic ones (e.g., foams, spinodal architectures), most of which have interconnected designs [37, 40, 41, 79, 85, 87, 88, 90, 114]. These studies reveal that the unique mechanical attributes, such as multi-stable reconfigurability and high stiffness- and strength-to-weight ratios, arise from the combination of stretching, bending, and buckling among the structural members [115–118], as well as from energy dissipation within the constituent materials [119]. These types of interconnected architected materials suffer from the development of inevitable stress concentrations at the junctions upon global mechanical loading, which deteriorates their strength and stiffness at greater-than-theoretical rate and accumulates damage (i.e., micro-cracks and localized deformations).

Interpenetrating lattice designs have recently been explored as alternatives to interconnected design [42, 43], showing the potential to achieve multifunctionality while being composed of mostly two interconnected lattices. Exploiting friction between structural members has also been shown as a method to absorb energy without accumulating significant damage [46, 47, 120, 121], but most designs lack hierarchy to further augment their properties. A different hierarchical design framework has been introduced, in which multiple interweaving fibers are arranged into effective beams within a micro-lattice that contains no junctions [122]. These interwoven lattices outperform classical monolithic, interconnected lattices with equivalent unit cell designs by offering 2–3 times higher absorbed energy per cycle when normalized to the first cycle, >70% greater deformability upon tension, >50% compressive strain without catastrophic failure, and directional compliance unachievable in their monolithic counterparts. The separation among the fibers within each effective beam opens the possibility to implement new kinematics beyond beam-joint and plate-hinge mechanisms [32, 116, 123]. For example, several lessons can be taken from knots, which can be found in a wide range of length scales—from sailing, climbing, and sutures to the entanglement of DNA, protein, and polymer strands [49–52]. The topology of knots has long been a topic of mathematical interest because it uniquely incorporates geometry and noncommutative algebra [53, 54], and researchers have discovered, for example, that even in two similarly configured knots, a slightly different twist can lead to diametrically opposite stabilities [55–57]. Mechanics-based studies on physical tight knots have revealed the importance of accounting for constituent material properties in knot failure predictions [59–61], and analyses of loose knots show their potential to increase energy dissipation and introduce stable tightening and untying mechanisms through careful selection of knot geometry and constituent materials [62–65].

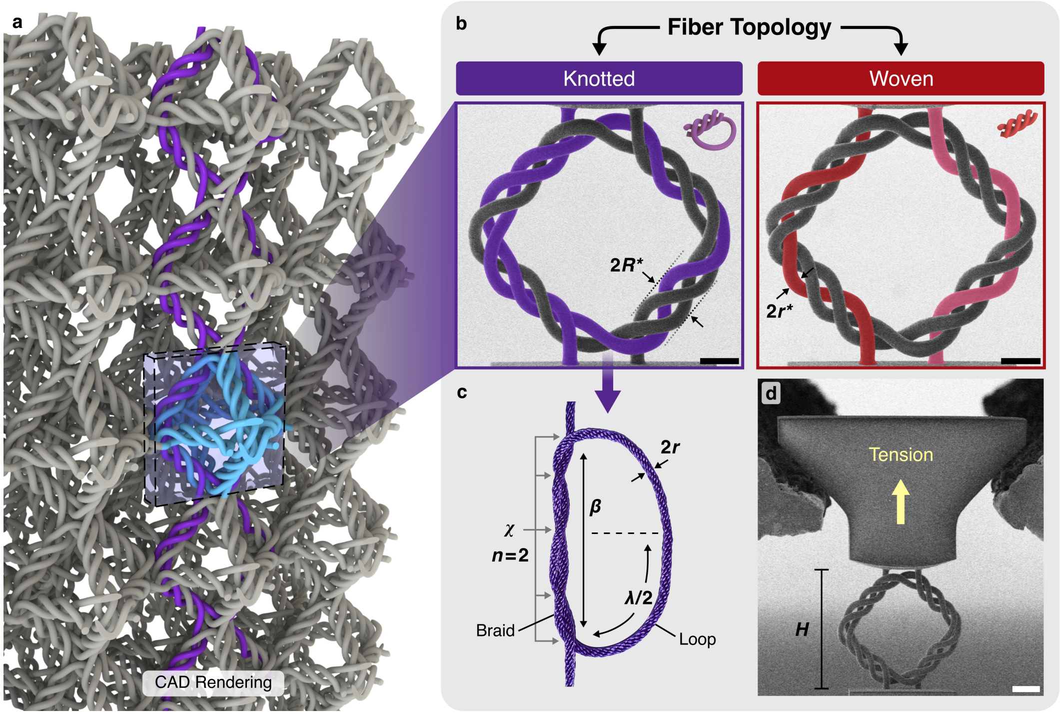

Figure 4.1: Knotted and woven fiber topologies in hierarchical intertwined materials. a) Computer-aided design (CAD) rendering of a hierarchical octahedron lattice where each unit cell is composed of three rhombuses. The rhombus in the rectangular box is formed by two knotted fibers, one being highlighted in purple and tessellated vertically. b) Scanning electron microscope (SEM) images with color shading overlaid onto a single fiber in the knotted (left) and woven (right) hierarchical rhombuses, each with two vertically connected fibers. An overhand knot is formed by each of the two fibers (one colored purple, the other uncolored) in the knotted rhombus. Vertical fibers in the woven rhombus are colored in red and pink, respectively. c) Photograph of an overhand knot that resembles the purple knot in a). d) An in situ experimental set-up inside an SEM on a representative intertwined rhombus frame. Scale bars: 10 µm (b), 20 µm (d).

4.3 Design and Fabrication of Hierarchical Intertwined Materials with Knotted and Woven Fiber Topologies

Here, we combine two previously independent concepts, hierarchical architected materials and fiber knotting, to develop building blocks for architected materials with simultaneous high deformability under every loading mode, energy dissipation, fracture resistance, and shape-reconfigurability. We classify the fiber topology of hierarchical intertwined materials into two fundamental topologies: knotted and woven (Figure 4.1). To elucidate the influence of fiber topology on the mechanical properties of hierarchical intertwined structures, we designed, fabricated, mechanically probed, and analyzed hierarchical woven and knotted rhombus-shaped frames with equal diagonals under quasi-static tension. The probing of a 2D frame with intertwined beams focuses on an identical sub-structure inside of a 3D unit cell in the lattice, in this case a rhombus inside of an octahedron, while maintaining identical hierarchy of each beam being comprised of three intertwined, separate fibers. Our experiments and theory show that the knotted fiber topology enables a new regime of deformation and reconfiguration in architected materials space, i.e., *knot tightening*. We investigated the effect of inter-fiber friction on the tying process by (i) applying different surface treatments to the fibers: passivation with a thin (~5-nm thick) layer of alumina (Al_2O_3), systematic irradiation with UV light (254-nm wavelength), and aging, and by (ii) conducting quasi-static in situ tensile experiments on all these samples with different surface treatments. We compare the mechanical response of UV-irradiated vs. aged rhombuses, as well as rhombuses with different linear dimensions, to investigate aging mechanisms and size effects in the intertwined polymeric structures.

Intertwined rhombus frames were fabricated out of IP-Dip photoresist using two-photon lithography (Nanoscribe GmbH) with an intended fiber radius r^* of 1.69 μm, beam radius R^* of 3.5 μm, and rhombus height H of 70 μm, as well as rhombuses with twice the linear dimensions ($H = 140$ μm). A 3D octahedron cube unit cell with a relative density (i.e., fill fraction) $\bar{\rho}$ of 5%, calculated as the volume of material in the unit cell compared to the total volume of the unit cell, and width equal to $H = 70$ μm was formed by assembling three rhombuses together, each aligned with one of the three Cartesian principal axes (see Figures 4.1a and 4.12 for representation in a lattice and in a single unit cell, respectively). Each beam in the rhombus was composed of three interwoven fibers, and a custom grip was fabricated on top of each rhombus (see Figure 4.1d) to enable in situ tensile experiments using a nanoindenter inside a scanning electron microscope (SEM).

4.4 Results

4.4.1 Influence of Hierarchical Topology: Knotted vs. Woven

The influence of fiber topology on the mechanical response of intertwined structures is highlighted in Figure 4.2 which shows applied uniaxial load F vs. strain ε, and the corresponding time-lapse images during the in situ uniaxial tension experiments on knotted vs. woven rhombus frames with a designed height H of 70 μm pulled to failure (see also Supplementary Movie 6). Tensile experiments demonstrate distinct regimes of deformation to failure, with the woven topology (Figure 4.2a) first undergoing fiber alignment, characterized by a nearly linear region with a slope

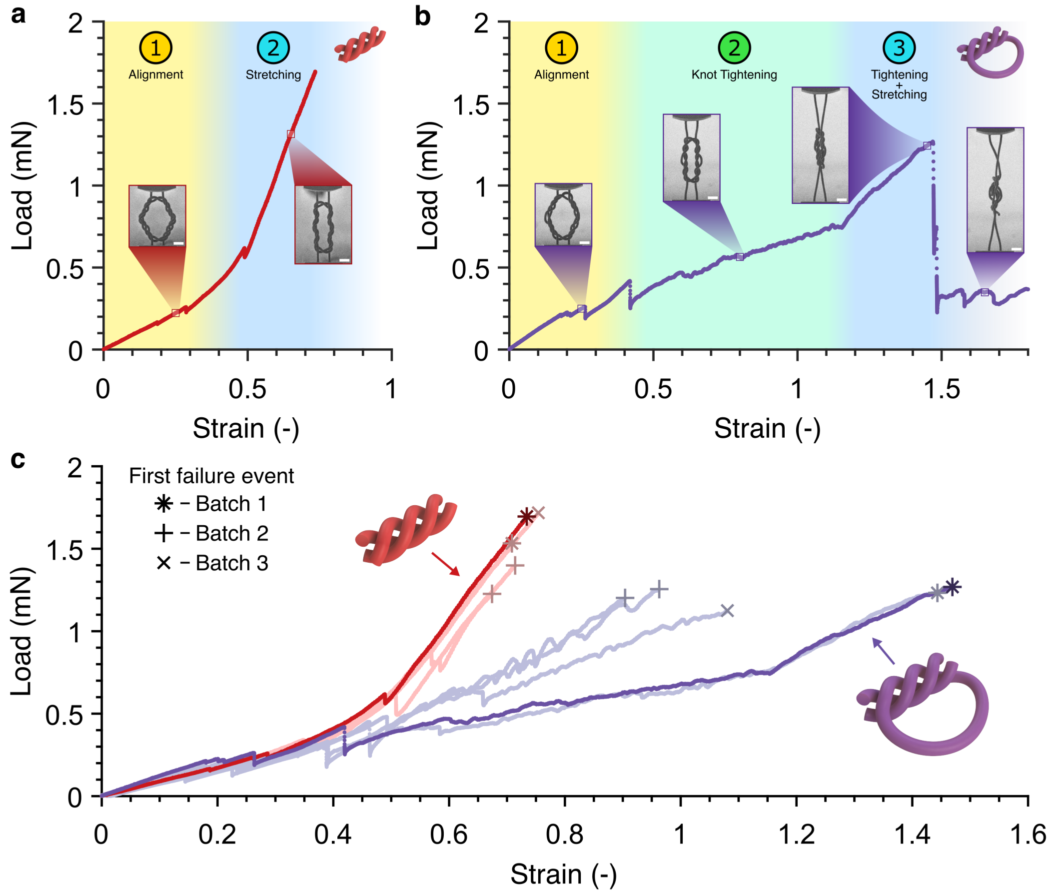

Figure 4.2: Microscale tensile experiments of hierarchical knotted and woven rhombus frames. Mechanical data and time-lapse images during tension of a representative a) woven and b) knotted frames pulled up to failure, showing distinct deformation regimes in each fiber topology. Throughout this figure, red data points correspond to woven geometry and purple to the knotted one. In b), mechanical data beyond ~147% strain corresponds to the unraveling of broken fiber(s) after the first failure event. c) Combined tensile response up to first failure event of five knotted and five woven rhombus frames from three separate rounds of fabrication. Bolder data sets come from the same tests shown in a) and b). Scale bars: 15 µm.

of ~0.9 mN (Regime 1) up to a strain of ~40%, followed by fiber stretching (Regime 2) at a 5 times higher slope in the data up to failure at 73.4% strain. The knotted frame (Figure 4.2b) also first underwent fiber alignment (Regime 1) with a similar signature up to a strain of ~40%, followed by knot tightening (Regime 2) characterized by smoother deformation at a steady stiffness of ~0.5 mN, and the combination of knot tightening and engaged fiber stretching from the strain of ~115% up to failure at 146.9% (Regime 3). Figure 4.2c contains data for five woven and five knotted samples fabricated in three separate batches, and it demonstrates that in the fiber alignment regime, rhombuses of both topologies show similar mechanical signature up to ε ~40%. All woven rhombuses then entered the fiber stretching regime indicated by a 5 times increase in the load-strain slope, up to incipient failure at the ultimate failure load F_f of 1.22–1.72 mN and a corresponding failure strain ε_f of 67.4–75.4%. At the transition strain of ε ~40%, the knotted rhombuses were also aligned along the loading direction and continued to deform past the failure strain ε_f of the woven rhombuses via the knot tightening mechanism available to this geometry. Two knotted rhombuses originating from the first batch showed a distinct transition between the knot tightening and fiber stretching regimes at a strain of ε ~115% up to failure at a strain of 144.3–146.9% and an applied failure load of 1.23–1.27 mN. Knotted rhombuses from different batches contained a less defined tightening-to-stretching transition, failing at a lower strain (90.4–96.3% for the second batch, 108.1% for the third) and similar failure loads. The first (ultimate) failure events, depicted with symbols corresponding to the samples' batch numbers, did not always invoke the breaking of all vertically oriented fibers, with some samples being able to bear load beyond their reported ultimate failure strains (see example in Figure 4.2b).

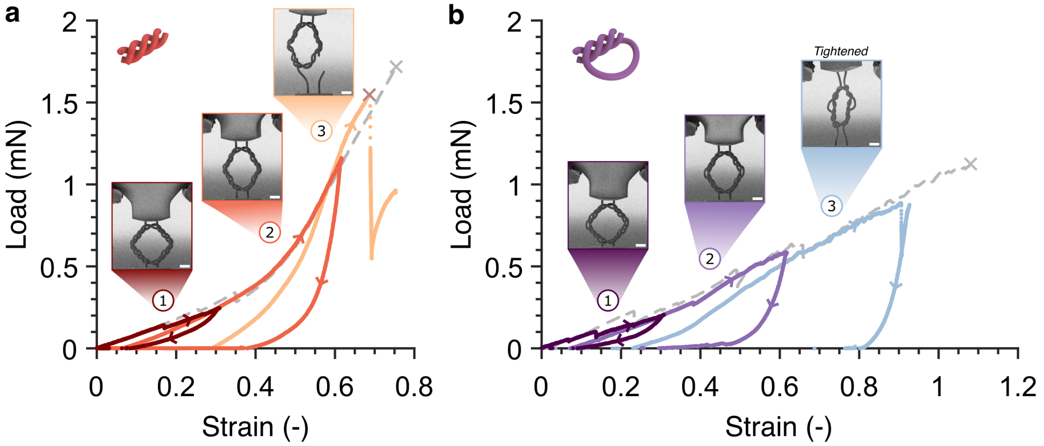

Figure 4.3: Microscale cyclic experiments of hierarchical knotted and woven rhombus frames. Load vs. strain for a) woven and b) knotted rhombuses cyclically loaded in tension, pre-strained to incrementally higher extents in each subsequent cycle. The still frames correspond to sample images at the end of each cycle, showing failure in the woven rhombus and stable reconfiguration via knot tightening in the knotted rhombus during the third cycle. Tensile responses up to failure of rhombuses with identical fiber topology originating from the same batch are shown in gray dashed lines. Scale bars: 15 µm.

The unique reconfiguration mechanism in hierarchical knotted topology is further showcased in Figure 4.3 , which contains the tensile response of knotted and woven rhombuses from the same batch subjected to several loading/unloading cycles at

∼30% strain increments per cycle and under monotonic loading to failure at a strain rate of 1 x 10^{-3} s^{-1} (see also Supplementary Movie 7). These plots indicate that the mechanical response of cyclically and monotonically loaded rhombuses of the same fiber topology matched one another closely at strains beyond the maximum strain of the previous loading cycle. In the first two loading cycles, both the knotted and woven rhombuses elongated via fiber reorientation and uncoiling before returning to their original shapes upon load removal, with slight twisting of the rhombus and a concomitant viscoelastic response present in the unloading region in both topologies. In the third cycle, the woven rhombus failed via fiber rupture around the same failure strain ε_f and failure load F_f as monotonically loaded samples. The knotted rhombus retained its knotted shape following unloading from ε ∼90% in the third cycle without any evidence of failure.

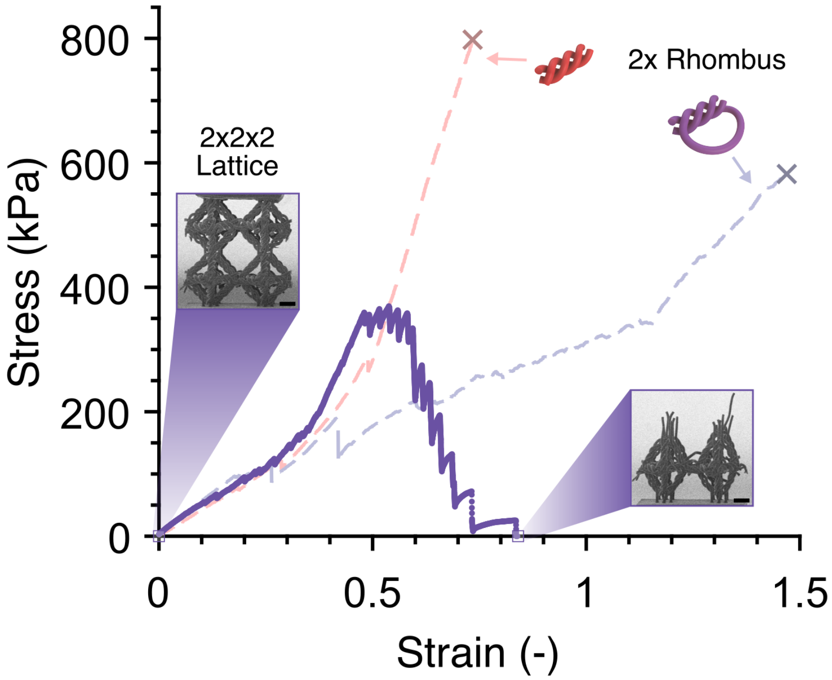

Figure 4.4: Tensile response of a knotted lattice. Load vs. strain response of a 2x2x2 tessellation of octahedron unit cells with two knotted rhombus frames aligned vertically and one horizontal woven frame per unit cell tested in tension up to failure in the knot tightening direction of both knotted frames. Predicted responses of a lattice consisting of woven and knotted frames are shown in dashed curves. Scale bars: 20 µm.

As a first attempt in adapting the hierarchical knotted framework in a lattice, a 2x2x2 tessellation of octahedron unit cells with two knotted rhombus frames and one woven frame per unit cell was fabricated and tested in tension up to failure in the knot tightening direction of both knotted frames (Figure 4.4). The number of fibers connecting one unit cell to an adjacent one is maintained at four, which is identical to previous work. The lattice stress σ vs. strain ε response is overlaid on top of the predicted stress σ vs. strain ε behavior obtained by multiplying the tensile responses of knotted and woven rhombus frames in this work by two since there are two knotted frames assembled vertically in each unit cell. The lattice stress vs. strain response followed the predicted trajectory for a woven lattice instead of the trajectory for a lattice consisting of knotted rhombuses, and it reached an ultimate tensile stress of 370 kPa with corresponding failure strain of 53.9%, both lower than the predicted failure stress of ~582 kPa and failure strain of ~147% for two knotted rhombuses in a unit cell (indicated by a purple "x" in Figure 4.4).

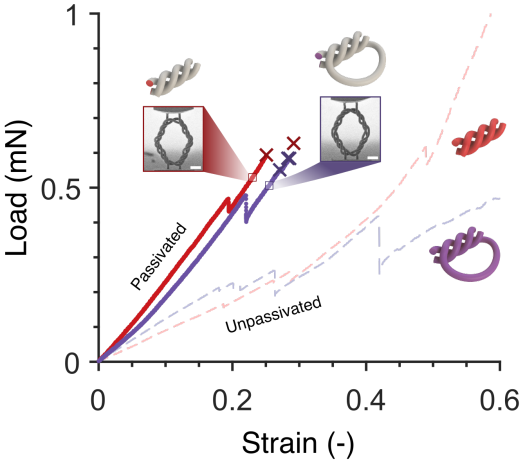

Figure 4.5: Effects of passivation and UV-irradiation on the mechanical behavior of intertwined architectures. Representative tensile responses up to first failure and corresponding still frames of knotted and woven rhombuses passivated with 5-nm thick Al_2O_3 film. The response of equivalent as-fabricated (unpassivated) rhombuses from Figure 4.2 is also shown. First failure events from all experiments are marked with "x". Scale bars: 15 µm.

4.4.2 Passivation of Hierarchical Fibers

To elucidate the effect of inter-fiber friction on the mechanical behavior of intertwined structures, we first passivated the samples identical to rhombuses in Figure 4.2c with a 5-nm thick alumina film deposited via Atomic Layer Deposition (ALD) at 200 °C and compared their F vs. ε response with that of the as-fabricated rhombuses (Figure 4.5). We observed nearly identical load-strain behavior between the two geometries, with the initial slope a factor of ~2.5–2.6 times higher than that of the as-fabricated samples, followed by ultimate failure in Regime 1 (fiber alignment) at a strain of ~25–30%. Passivated knotted rhombuses failed at ε_f = 27.1–28.6% and F_f = 0.55–0.58 mN, and woven samples at ε_f = 25.1–29.2% and F_f = 0.59–0.63 mN which are ~2–3 times lower than those of unpassivated woven frames. We observed a similar trend in the tensile response of cylindrical pillars made of the same IP-Dip resist with radii of 1.69 µm and heights of 10 µm subjected to different post-processing procedures: (1) as-fabricated samples (termed pristine) and, (2) ones passivated with a 5-nm thick ALD alumina immediately after fabrication (Figure S1); tensile experiments on the passivated pillars show ~144% and ~43% increase in Young's Modulus E and yield stress σ_y compared to pristine pillars, respectively, as well as ~27% decrease in ultimate tensile strength (UTS, σ_{UTS}) and ~88% drop in strain at UTS (ε_{UTS}).

4.4.3 UV Radiation

Figure 4.2 highlights the knot tightening mechanism that is unique to the knotted topology; it requires fibers to slide past one another and helices to tighten to result in a shrunken rhombus as fibers are being pulled along the loading direction. To explore how varying fiber bulk and surface properties affect the mechanical behaviors of intertwined structures beyond the fiber alignment regime, we pulled to failure knotted and woven rhombuses of H = 70 µm from the same batch that had undergone the following treatments: (i) pristine, (ii) irradiated under UV for 5-hr, and (iii) irradiated under UV for 29-hr (Figure 4.7, see Chapter 2 for details on UV-irradiation process). These experiments revealed that in the fiber alignment regime, i.e. at strains below 40%, the loads of UV-irradiated (ii and iii) woven frames are up to ~80% higher than those of pristine (i) samples (Figure 4.8a). Increasing the UV radiation time strengthened the woven frames in the fiber stretching regime, which failed around the same ε_f: 67.4–71.4% strain for pristine samples, 68.5–69.9% for the 5-hr UV-irradiated samples, and 70.3–72.1% for the 29-hr UV-irradiated ones, with corresponding F_f of 1.23–1.40 mN, 1.60–1.66 mN, and 2.49–2.57 mN, respectively.

No clear trend in the difference between pristine and 5-hr UV-irradiated knotted samples was observed; the loads for 29-hr UV-irradiated knotted samples are up to ~90% higher than those of other knotted rhombuses in all regimes of deformation for a given strain (Figs. 3C and S2B). All knotted frames experienced first failure events at higher strains compared to all woven rhombuses, at similar or lower F_f compared to woven rhombuses that underwent the same post-processing procedures: ε_f = 90.4–96.3% and F_f = 1.20–1.26 mN for pristine samples, ε_f = 81.7–126.2% and F_f = 1.14–1.66 mN for 5-hr UV-irradiated samples, and ε_f = 81.0–111.4%

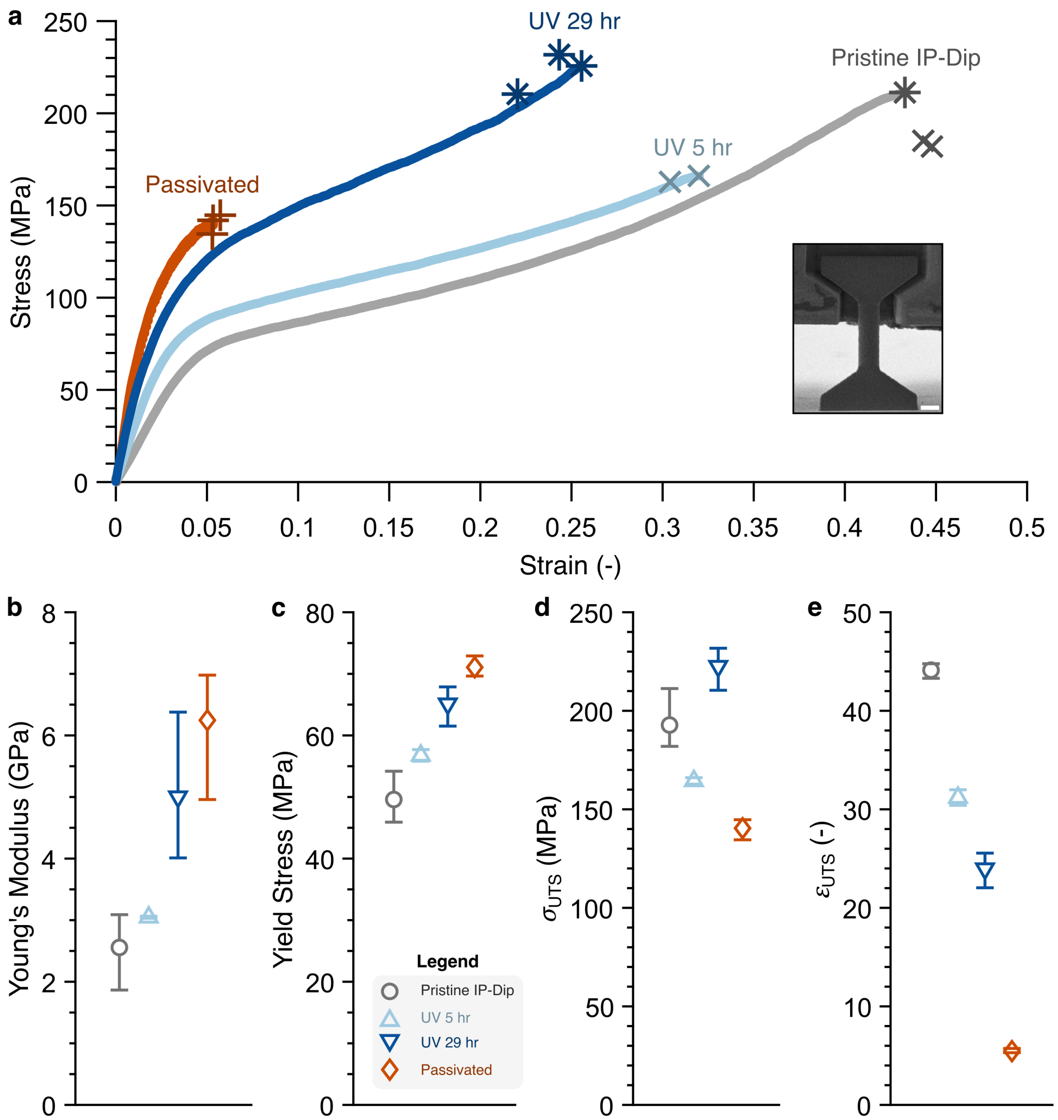

Figure 4.6: Tensile testing of IP-Dip pillars. a) Mechanical behaviors of IP-Dip pillars that underwent various post-treatment procedures. The pillars had a designed radius of 1.69 µm, identical to the intended fiber radius r^* in hierarchical rhombuses with designed height H of 70 µm. Inset shows in situ tensile testing set-up inside a scanning electron microscope (SEM). b) Young's Modulus, c) yield stress, d) ultimate tensile stress (UTS), and e) strain at UTS of IP-Dip pillars shown in a). Markers and error bars represent mean and extrema of the data sets, respectively. Scale bar: 3 µm.

corresponding to F_f = 1.41–2.12 mN for 29-hr UV-irradiated ones. We investigated the mechanical and surface properties of (i) pristine, (ii) 5-hr UV-irradiated, and (iii) 29-hr UV-irradiated IP-Dip 3.38 µm-diameter pillars via in situ tensile testing (Figure 4.61) and X-ray photo-electron spectroscopy (XPS) characterization (Figure 4.9, see Chapter 2 for details on XPS characterization). These experiments uncov-

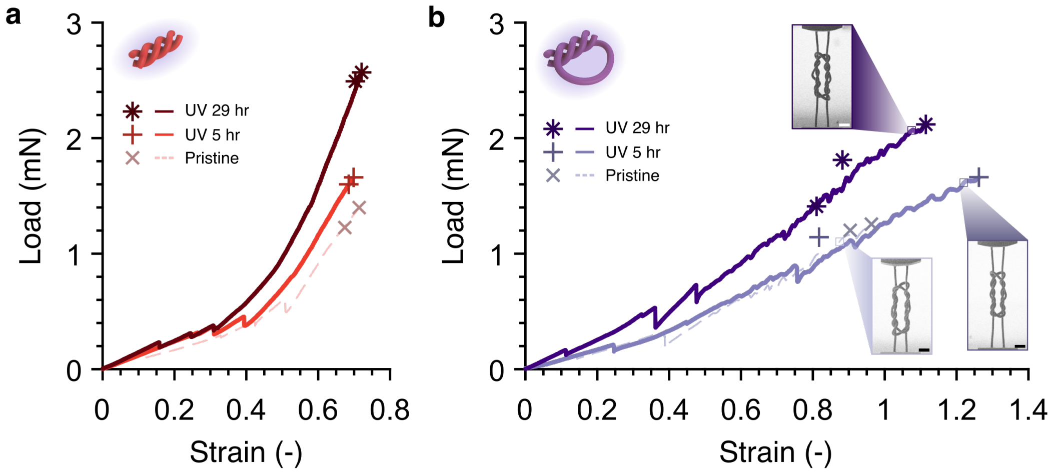

Figure 4.7: Effects of UV-irradiation on the mechanical behavior of intertwined architectures. Representative tensile responses up to first failure events of UV-irradiated and pristine hierarchical a) woven and b) knotted rhombuses with corresponding still frames. All samples in a) and b) originated from the same batch and their first failure events are marked with indicated symbols. Mechanical data for pristine hierarchical rhombuses are also shown in Figure 4.2c. Scale bars: 15 µm.

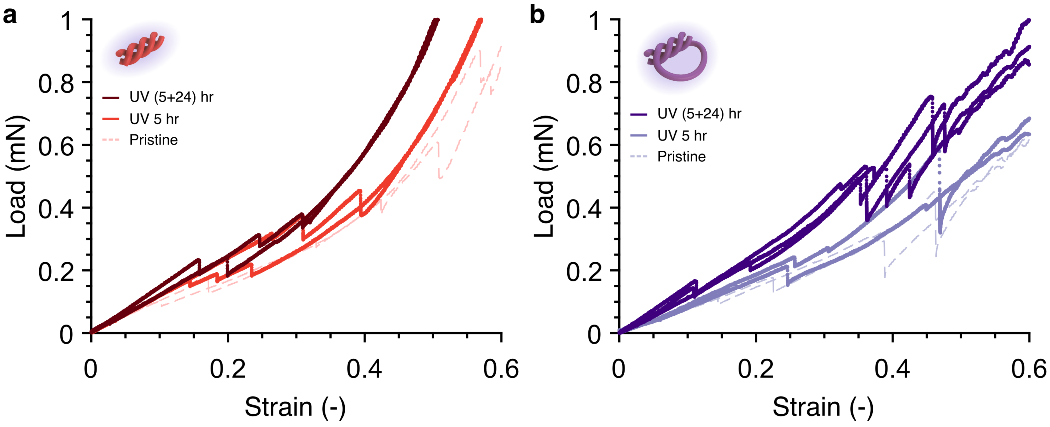

Figure 4.8: Effects of UV-irradiation on the fiber alignment regime of knotted and woven rhombus frames. Tensile responses within the fiber alignment regime of all UV-irradiated and pristine hierarchical a) woven and b) knotted rhombuses originating from the same batch.

ered that greater irradiation time increases the modulus E and the yield strength σ_y with a concomitant reduction in tensile strain ε_{UTS}. The ultimate tensile stress σ_{UTS} of pillars irradiated for 5-hr decreased by ~10% while σ_{UTS} of 29-hr UV-irradiated pillars on another chip increased by ~5% compared with pristine IP-Dip pillars on their corresponding chips.

XPS performed on as-printed and 29-hr irradiated samples revealed slight differences in peaks assigned to carbon in several oxidation states, as demonstrated in Tables 4.1 and 4.2 below. However, the C 1s signal as assigned to the as-printed sample was not consistent between different as-printed samples as seen between Tables 4.1 and 4.3 below, indicating a lack of an unambiguous signal corresponding to surface transformations, such as chain scission [124], occurring on a given sample.

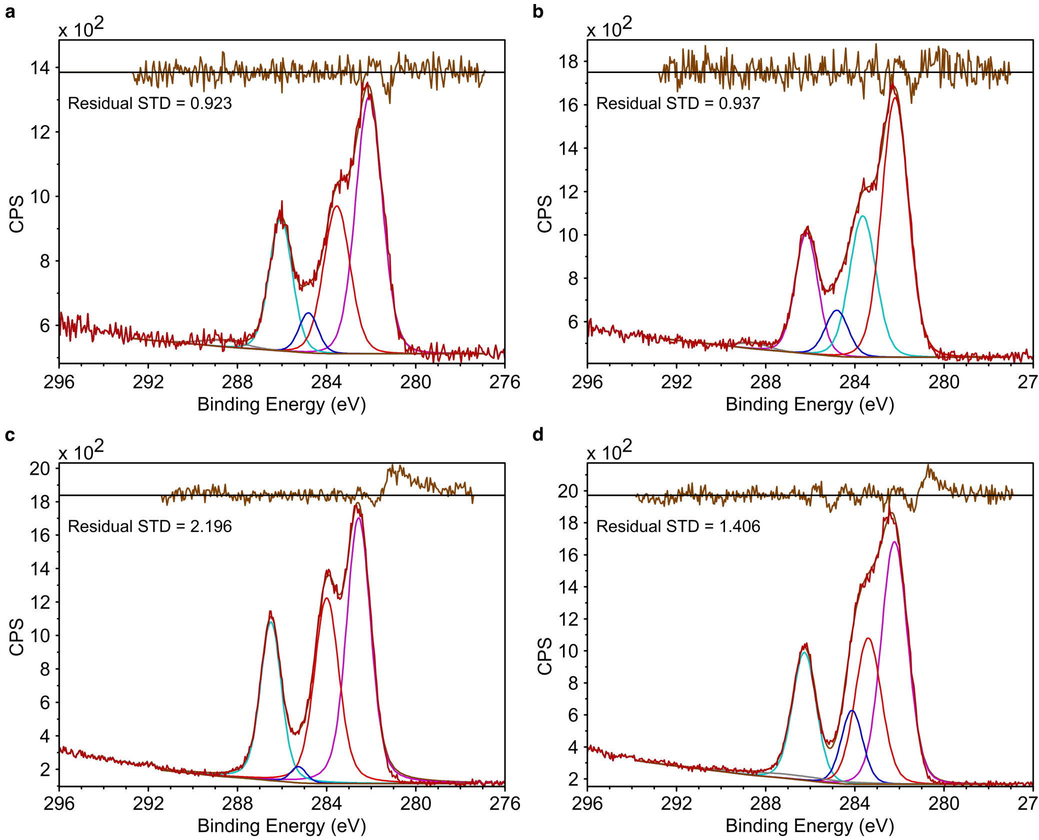

Figure 4.9: XPS characterization of IP-Dip plates. C 1s spectrum of a set of IP-Dip plates a) without UV-irradiation and b) after 29-hr UV-irradiation, and a second set of IP-Dip plates c) without UV-irradiation and d) after 29-hr UV-irradiation. CPS is photoelectron counts in counts per second.

Assignment	Line Shape	Intensity (RSF Adj.)	FWHM (eV)	FWHM Const. (eV)	Position (eV)	Area %
C-C, C-H	LA	2348.4	1.4	0.8-1.4	282.2	45.83
C-O	LA	1332.1	1.4	0.8-1.4	283.5	25.95
C=O	LA	364.9	1.3	0.8-1.4	284.9	7.14
O-C=O	LA	944.3	1.1	0.8-1.4	286.1	18.41
$\pi - \pi*$	LA	137.2	3.4	-	288.1	2.68

Table 4.1: Assignments to a C 1s signal from XPS characterization of a pristine IP-Dip plate shown in Figure 4.9a.

XPS performed on a single site on one sample measured near the time of synthesis yielded a C 1s signal composed of five elements assigned in Table 4.1 above. Full width at half maximum (FWHM) of all peaks other than the $\pi - \pi^*$ shake-up was constrained between 0.8-1.4 eV as appropriate for a modern instrument. Notably, a stretch at the expected position of a C=O signal was present despite the absence of carbonyls in the known composition of the photoresist. This may be due to the presence of carbonyls in the undeclared 10% of the IP-Dip photoresist as per the MSDS. See References [125] and [126] for more information on conducting and interpreting XPS results. We record the ratio of the C-O:C-C/C-H and O-C=O:C-C/C-H intensities (RSF adjusted) for further analysis:

C-O:C-C/C-H: 944.3/2348.4 = 0.4017,
O-C=O:C-C/C-H: 1332.1/2348.4 = 0.5662.

Assignment	Line Shape	Intensity (RSF Adj.)	FWHM	FWHM Const. (eV)	Position (eV)	Area %
C-C, C-H	LA	3539.5	1.4	0.8-1.4	282.2	47.14
C-O	LA	1927.8	1.4	0.8-1.4	283.6	25.67
C=O	LA	546.6	1.2	0.8-1.4	284.8	7.28
O-C=O	LA	1402.6	1.2	0.8-1.4	286.2	18.68
$\pi - \pi^*$	LA	92.3	1.7	-	288.6	1.23

Table 4.2: Assignments to a C 1s signal from XPS characterization of a 29-hr UV-irradiated IP-Dip plate shown in Figure 4.9b.

XPS performed on a single site on one sample irradiated for 29 hr yielded a C 1s signal composed of five elements assigned in Table 4.2 above. FWHM of all peaks other than the $\pi - \pi^*$ shake-up was constrained between 0.8-1.4 eV as appropriate for a modern instrument. Again, a stretch at the expected position of a C=O signal was present despite the absence of carbonyls in the known composition of the photoresist. With respect to the pre-irradiation sample, we noted that the ratios C-O:C-C/C-H and O-C=O:C-C/C-H with respect to peak intensities (RSF adjusted) decreased after irradiation; however, given the differing results for the pre-treatment and post-treatment conditions in Tables 4.3 and 4.4 below, we are skeptical of the utility or clarity of this result. The ratio of the C-O:C-C/C-H and O-C=O:C-C/C-H adjusted) are as follow:

C-O:C-C/C-H: 1402.6/3539.5 = 0.39627,
O-C=O:C-C/C-H: 1927.8/3539.5 = 0.54465.

The computations below, following the attempted method of quantifying the degree

Assignment	Line Shape	Intensity (RSF Adj.)	FWHM (eV)	FWHM Const. (eV)	Position (eV)	Area %
C-C, C-H	LA	4483.4	1.4	0.8-1.4	282.2	47.11
C-O	LA	2697.8	1.4	0.8-1.4	283.4	25.13
C=O	LA	1108.4	1.1	0.8-1.4	284.1	10.33
O-C=O	LA	2113.3	1.2	0.8-1.4	286.3	19.69
$\pi - \pi^*$	LA	330.9	5.3	-	286.9	3.083

Table 4.3: Assignments to a C 1s signal from XPS characterization of a pristine IP-Dip plate shown in Figure 4.9c.

of transformation of C-O and O-C=O functional groups in the irradiation process, demonstrate the potentially widely varying value of the ratio of these components between scans of samples produced under identical conditions. Given the inherent difficulty in differentiating between carbon deriving from an adventitious source versus carbon in a known polymer, these values shed doubt on the ability to accurately derive transformation of surface polymer chains from the collected XPS data, especially when compared to data obtained from 29-hr UV-irradiation of the previous sample. The ratio of the C-O:C-C/C-H and O-C=O:C-C/C-H intensities (RSF adjusted) corresponding to Table 4.3 are as follows:

C-O:C-C/C-H: 2697.8/4483.4 = 0.60173,
O-C=O:C-C/C-H: 2113.3/4483.4 = 0.47136.

Assignment	Line Shape	Intensity (RSF Adj.)	FWHM (eV)	FWHM Const. (eV)	Position (eV)	Area %
C-C, C-H	LA	4623.1	1.3	0.8-1.4	282.6	44.02
C-O	LA	3300.2	1.3	0.8-1.4	284.0	31.42
C=O	LA	187.1	0.84	0.8-1.4	285.3	1.78
O-C=O	LA	2392.5	1.1	0.8-1.4	286.5	22.78
$\pi - \pi^*$	LA	1.9×10^{-20}	7.58	-	291.4	0.0

Table 4.4: Assignments to a C 1s signal from XPS characterization of a 29-hr UV-irradiated IP-Dip plate shown in Figure 4.9d.

The computations below, following the attempted method of quantifying the degree of transformation of C-O and O-C=O functional groups in the irradiation process as described below Tables 4.1 and 4.2, demonstrate the potentially widely varying value of the ratios calculated between pristine samples and the same samples after 29-hr of UV-irradiation, exhibiting the unreliability of the measure as a gauge of chain scission on sample surfaces:

C-O:C-C/C-H: 3300.2/4623.1 = 0.71385,
O-C=O:C-C/C-H: 2392.5/4623.1 = 0.51751.

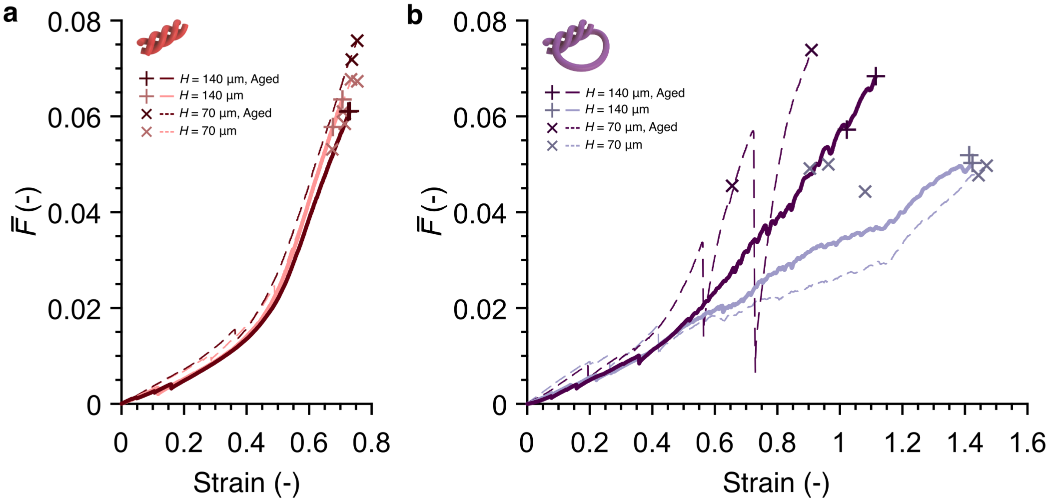

Figure 4.10: Effects of varying linear dimensions and aging. Representative tensile responses of pristine and aged a) woven and b) knotted rhombus frames with designed rhombus height H of 70 µm and 140 µm. Mechanical data for pristine frames of H = 70 µm originated from the data shown in Figure 4.2c. First failure events from all samples are marked according to the indicated symbols. The four pristine knotted frames in b) with ε_f > 140% were fabricated within two days of each other on two separate chips and tested within a 24 hr period while the other knotted rhombuses originated from different batches.

4.4.4 Effects of Microscale Feature Sizes and Aging

We probed into the influence of feature size on the mechanical behavior of architected materials comprised of IP-Dip fibers, which have been reported to lack size effects in modulus and yield strength within 1-10 µm [97]. We fabricated and tested one batch of larger self-similar pristine knotted and woven frames with designs and printing parameters identical to those shown in Figure 4.2 with double the linear dimensions, H = 140 µm. We define a normalized load $\bar{F}$ as the applied load F divided by the product of the Young's Modulus of IP-Dip E_{pr} and the fiber cross-sectional area $A = \pi\,(r^*)^2$. Figure 4.10 conveys $\bar{F}$ vs. ε data for woven and knotted frames and does not show discernible differences between their mechanical response. These experiments also show that pristine knotted frames attain an average of $\sim$75%, and a maximum of $\sim$107% increase in ε_f compared to pristine woven samples.

We also performed tensile-to-failure experiments on the knotted and woven frames that had been aged under normal laboratory conditions for more than 75 days and compare their $\bar{F}$ vs. ε response in Figure 4.10. Pristine samples were tested not

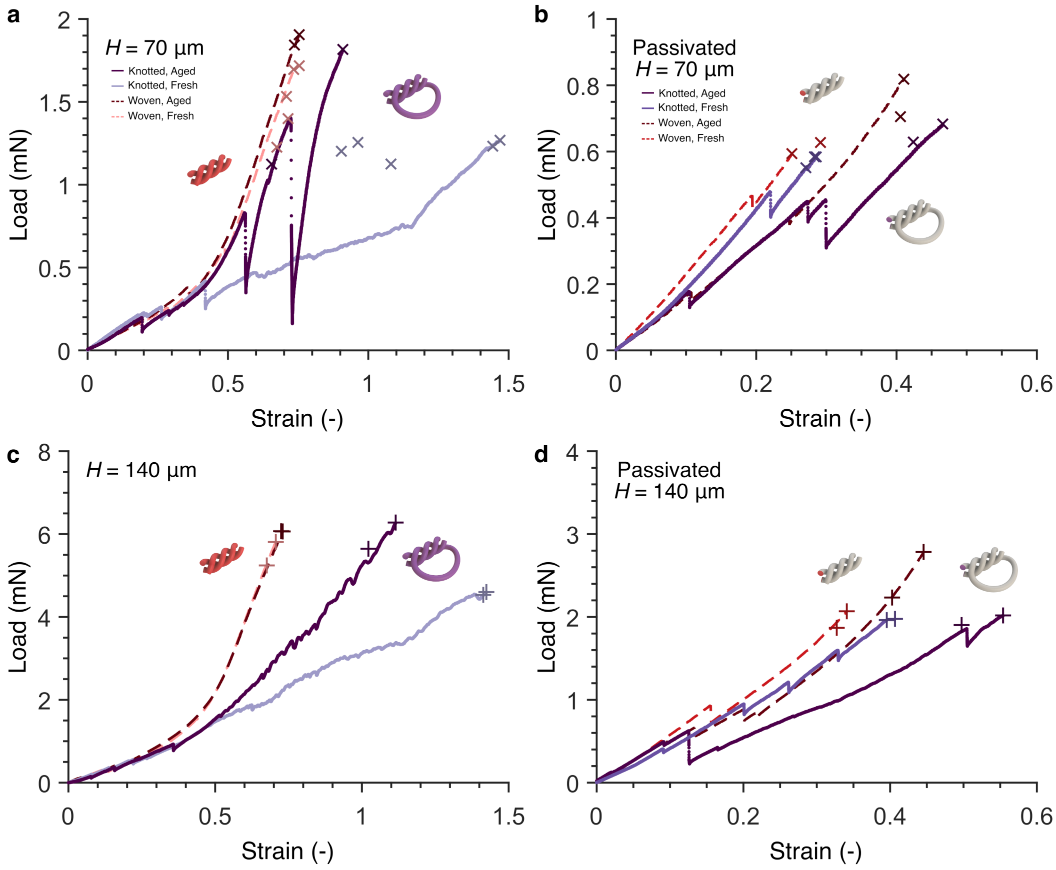

Figure 4.11: Effects of aging on unpassivated and passivated intertwined architectures of varying sizes. Representative tensile responses up to first failure events of pristine and aged a) unpassivated and b) passivated rhombuses of H = 70 µm. First failure events are marked by "x". Representative tensile responses up to first failure events of pristine and aged c) unpassivated and d) passivated rhombuses of H = 140 µm. First failure events are marked by "+".

more than nine days after fabrication, and the mechanical behavior of pristine vs. aged woven frames is virtually identical with the latter failing at an average of ~10% greater $\bar{F}$ compared to pristine woven samples of the same size. Significant discrepancies can be observed in $\bar{F}$ vs. ε data for knotted frames, with the aged samples generally being more than 40% stronger than the pristine ones at a given strain past the fiber alignment regime, and the smaller (H = 70 µm) knotted frames deforming via a more pronounced stick–and–slip mechanism. The aged knotted frames with H = 70 µm experienced first failure events around ε_f of 65.5–90.9% and a normalized ultimate failure load $\bar{F}_f$ of 0.046–0.074, while the larger, aged knotted samples (H = 140 µm) had ε_f of 102.2–111.5% and $\bar{F}_f$ of 0.057–0.068 (see Figure 4.11, a and c, for F vs. ε plots corresponding to Figure 4.10). Tension-to-failure of all aged passivated (Figure 4.11, b and d) samples were somewhat more compliant and deformable compared with their pristine counterparts and also experienced first failure events generally within the fiber alignment regime.

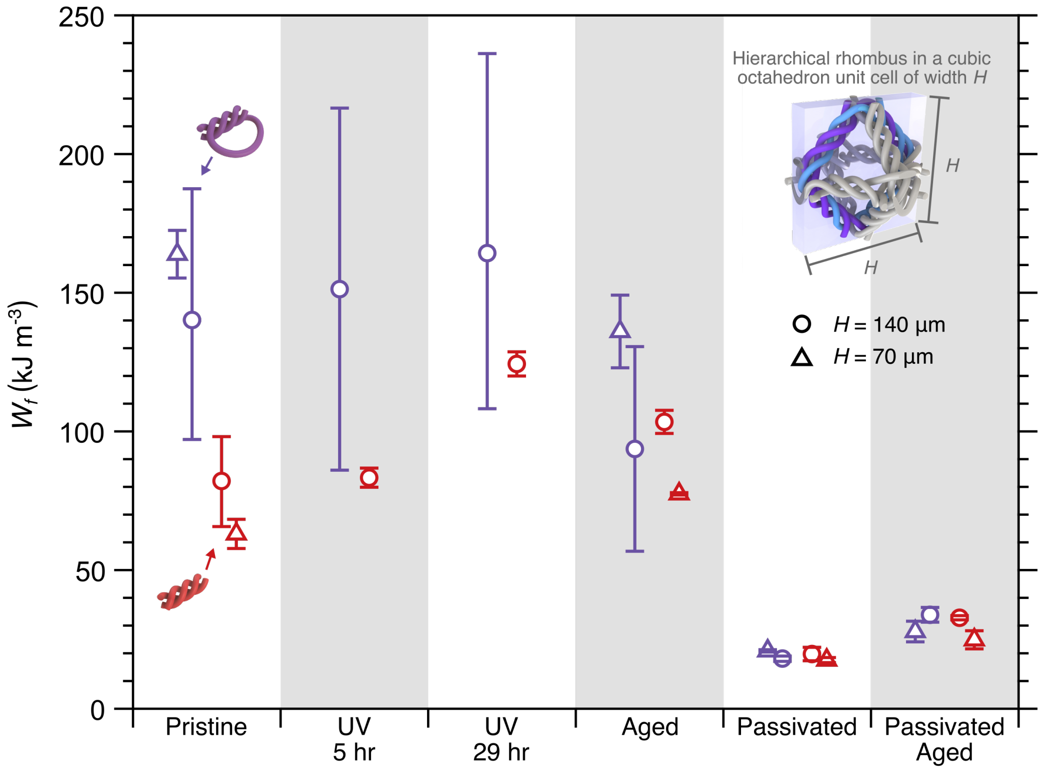

Figure 4.12: Energy absorption capability of intertwined architectures. Absorbed energy density up to first (ultimate) failure load, W_f, of all hierarchical intertwined frames tested in this work. The variable W_f represents the contribution of a rhombus frame inscribed in a cubic unit cell with side length H to energy absorption. Markers and error bars denote mean and extrema of the data sets, respectively (n ≥ 2).

4.4.5 Energy Absorption of Intertwined Architectures

To meaningfully compare the energy absorption properties of the intertwined frames with other materials, we introduce the absorbed energy density variable W_f and plot the W_f values for each type of sample tested in this work in Figure 4.12. W_f is defined as the absorbed energy density up to first (ultimate) failure event and is calculated by taking the area under the F vs. ε curve up to the strain at first failure and dividing it by H^2 which essentially equate W_f as the energy absorption contribution of the frame to a cubic unit cell with side length H up to the first failure event. The absorbed energy density up to maximum failure load W_f and the absolute absorbed energy density W_{abs} are calculated using the following equations:

$$W_f = \int_0^{\varepsilon_f} \frac{F}{H^2}\, d\varepsilon, \tag{4.1}$$

$$W_{abs} = \int_0^{\varepsilon^*} \sigma\, d\varepsilon, \tag{4.2}$$

where ε_f is the strain at first failure load, σ is the engineering stress on a lattice structure, and ε^* is the maximum tensile strain achieved by the structure during testing.

Pristine knotted frames are shown to possess 71–160% higher average W_f compared to pristine woven samples of the same H (Figure 4.12). UV-irradiation increases the average W_f of intertwined frames, with knotted samples (H = 70 µm) having 17% higher average W_f after 29-hr UV-irradiation and woven samples with identical H and UV-irradiation time having 51% higher average W_f compared to their pristine counterparts. Aged knotted and woven samples of all sizes have 22% lower and 18% higher average W_f than their corresponding pristine samples, respectively. We also observed large drops of average W_f for passivated samples, with passivated pristine knotted samples experiencing the largest drop of ~87% compared to unpassivated ones.

4.5 Discussion

4.5.1 Enhanced Extensibility and Energy Dissipation in Knotted Architectures

The differences in deformation regimes between knotted and woven frames indicate that fiber topology allows for greater tunability of the mechanical behavior when architected materials are made interwoven without changing the configuration of the higher hierarchical levels, such as the nodal connectivity and unit cell configuration. The ~75% higher average failure strain ε_f in pristine knotted frames compared to woven ones is likely translatable to a lattice framework since ε_f of woven frames falls within ε_f of the most extensible IP-Dip hierarchical woven lattices in [122]. The knotted shape retention upon unloading from the knot tightening regime (Figure 4.3b) also presents a novel shape transformation mechanism in an architected material. The ~92% increase in W_f of pristine knotted frames compared to pristine woven frames suggests that friction has a more significant role in dissipating energy within the knotted geometry than in the woven one due to the addition of the knot tightening deformation regime.

Based on average W_f values reported in 4.12, and without considering constriction caused by other fibers from other frames in a hypothetical unit cell, each pristine knotted frame in a unit cell is expected to contribute an average W_f of ~147 kJ m^{-3} when pulled in the direction of knot tightening. Thus, for an octahedron unit cell with two perpendicular rhombus frames aligned on the pulling axis (Figure 4.12), the unit cell may attain up to W_f ~294 kJ m^{-3} in that direction, which is ~34% higher than the average absolute (i.e., up to maximum strain beyond strain at maximum failure load) absorbed energy densities W_{abs} of monolithic (non-intertwined) octahedron lattices with similar relative density, and ~105% higher than the average W_{abs} of previously reported hierarchical woven lattices [122]. The 2x2x2 lattice designed with this unit cell (Figure 4.4) obtained an absorbed energy density W_{abs} of 125.4 kJ m^{-3}, which is in the range of W_{abs} of hierarchical woven lattices from previous work. This result, combined with the lower failure stress and strain compared to the prediction for knotted frames assembled in a unit cell, indicates that fiber constriction and manufacturing defects (e.g., fiber fusing, shape deviations) may have prevented the knotting mechanism to be activated in the lattice.

4.5.2 Effects of Varying Surface and Bulk Properties

4.5.2.1 Passivation

The similarity in the mechanical behavior of passivated woven and knotted frames, combined with the ~2–4 times lower ε_f and ~2–3 times lower F_f compared to their non-passivated counterparts, suggests that alumina coating diminishes mechanical performance, in contrast to the trend seen in passivated IP-Dip/alumina beam-based microlattices, which become brittle as thicker ALD alumina film is deposited [127]. The similar mechanical behavior corresponds to nearly identical absorbed energy density W_f between knotted and woven passivated frames, and the lower ε_f and F_f lead to lower W_f between passivated samples and other samples of the same topology and age. The low ε_f and F_f exhibited by the passivated interwoven frames can be explained by the relatively large drop of ~88% in ε_f accompanied by marginal reduction in σ_f during tension of the pristine passivated pillars, likely resulting from the brittle nature of alumina encapsulation [128]. The ~150–160% increase in the initial loads of the pristine passivated frames can also be attributed to the material effect: the higher modulus E of 6.25 GPa for passivated pillars results from ~2 orders of magnitude difference between ALD alumina (~165 GPa) and IP-Dip (~2.56 GPa), as well as the potential effect of thermal curing during the ALD process [129]. The drop of up to 76% in the failure strain of passivated frames can be explained by the fiber bending-initiated cracks that formed in the ALD alumina film during fiber realignment, which reduced overall load-bearing capability of the sample through a more uniform load distribution. Greater fiber slenderness ratio, defined as the fiber radius r^* divided by the length of the fiber, and a lower initial curvature, as well as tailored surface properties, can be employed to induce beyond-alignment deformability in interwoven architectures comprised of brittle fibers.

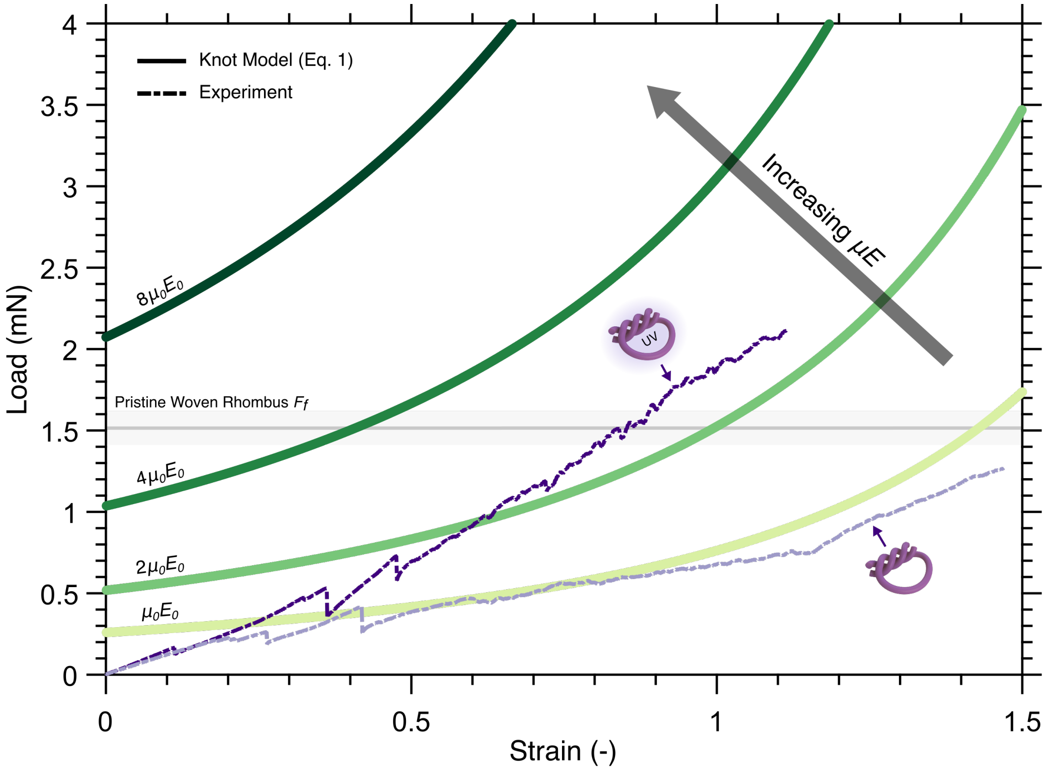

Figure 4.13: Comparison between experiments and an analytical knot model. Experimental tensile data for pristine and 29-hr UV-irradiated knotted frames of H = 70 µm are shown alongside analytical predictions with varying fiber properties. The predictions model the tightening of two separate, parallel knots with similar geometries to the experimental comparisons. The horizontal dark gray line and light gray region represent the mean and standard deviation of the force at first failure events of woven frames (H = 70 µm).

4.5.2.2 Theoretical Predictions

For frames that can deform past the fiber alignment regime, the additional fiber contact and sliding allowed by the knot tightening mechanism in knotted topology grants more control of mechanical behavior via the modification of fiber surface and bulk properties. We apply an analytical knot model for long overhand elastic knots to quantify their deformation and compare it to the load F vs. strain ε data of knots with varying fiber surface and bulk mechanical properties, as well as knot topology (Figure 4.13). According to the knot model developed by Jawed et al. [62], the tensile load F required to tighten a long overhand elastic knot to a certain end-to-end length $e = \lambda + \beta$ (analogous to knot size, see schematic in Figure 4.1c), where λ is the loop arclength and β is the braid length, can be expressed implicitly as

$$n^2 \frac{r}{e} = \frac{1}{8\sqrt{3}\pi^2} g\left(\left[\frac{384\sqrt{3}\pi}{\mu} \cdot \frac{n^2 F}{E r^2}\right]^{\frac{1}{3}}\right), \tag{4.3}$$

where $n = \frac{\chi - 1}{2}$ is the unknotting number (i.e., the number of times the fiber must be passed through itself to untie the knot), χ is the crossing number (i.e., the number of times the fiber crosses over itself), μ is the dynamic friction coefficient, E is the Young's Modulus of the fiber, and $g(x)$ is a nonlinear function mapping $\frac{\beta}{R}$ to $\frac{\beta^2}{eR}$ with R being the radius of the knot's loop. In our adaptation, the tensile strain ε is calculated by dividing the tensile displacement $(e_0 - e)$, where e_0 is the initial end-to-end length, with the initial height H_0. When the model is compared with experimental results, we multiply the tensile load F of the model by 2 to compare it with the tensile load of the frame since there are two intertwined overhand knots in each knotted frame.

The overhand knot model assumes friction to follow Amontons-Coulomb laws of friction (friction force $\propto$ normal force), and it also assumes an initially straight fiber deformed into an overhand knot with a tight braid of length β, unknotting number n, and loop arclength λ. The model predicts that when two separate, parallel overhand knots with geometries similar to experiments in this work ($n = 2$, $r = 1.69$ µm, starting e = combined rhombus side lengths ≈ 198 µm) are tightened, the difference in magnitude of the applied load F for a given strain is roughly proportional to the change in μE. Using $\mu = \mu_0 = 0.1$ and $E = E_0 = 2$ GPa, which is around the Young's Modulus of pristine IP-Dip pillars in this work, the model predicts that an increase in μ of four times and larger on an otherwise identical knot may result in a low strain at failure (<50%) and lower absorbed energy since the frame would already reach the failure load of a woven frame (gray horizontal region in Figure 4.13) at a strain below 50%. The effect of the unknotting number n in the overhand knot model manifests itself in the loop radius R as a function of strain ε: $R \to r$ as $\varepsilon \to 150\%$ for $n = 2$ in the model, and $R \to r$ as $\varepsilon \to 94\%$ for $n = 3$. These strains represent initiation of transition from knot tightening to fiber stretching regime (Figure 4.2b); beyond them the model no longer applies. We measured the highest failure strain of pristine and UV-irradiated knotted rhombuses in our experiments to be ~147%, rendering $n < 3$ to be more appropriate for comparison with experiments.

Using the same values as mentioned above, the model predicts analytical form of F vs. ε that is similar to experimental data (Figure 4.13). Close quantitative agreement does not immediately validate the use of the overhand knot model for knotted architectures because the model: (i) assumes full contact only within the braid of one knot, (ii) does not take into account material nonlinearity and initial curvatures in the undeformed fibers, and (iii) contains restrictions on μ. These limitations, along with a potentially high computational cost for a comprehensive numerical study on knotted architectures, suggest that subsequent studies are necessary to fully untangle the effects of geometrical parameters and material properties on the deformation and energy absorption mechanisms in hierarchical microwoven materials.

4.5.2.3 UV Radiation

The lack of conclusive correlation among the failure strains of frames and pillars with different UV-irradiation times suggests that there is a transition in rhombus failure initiation mechanism from being primarily influenced by the ductility of the constituent material during bending in Regime 1 to potentially being initiated by more localized deformation when initially curved fibers are straightened in Regime 2 while in contact with other fibers. In knotted fibers, the knot tightening mechanism may induce more complex stress states when fibers are crimped. Similarities in the mechanical behavior of pristine and 5-hr UV-irradiated knotted rhombuses suggest that the combined effects of surface and bulk mechanical properties of fibers in both types of structures are also similar, which is confirmed through comparisons between pristine and 5-hr UV-irradiated pillars (Figure 4.6) and surface characterizations. Using the overhand knot model as guidance, the higher load levels for 29-hr UV-irradiated knotted rhombuses can be attributed to the 1.3–2.1 times higher pillar modulus and post-yield stress compared to pristine and 5-hr UV-irradiated pillars. Polymer chain scission on the surface of 29-hr UV-irradiated fibers may have also increased the dynamic coefficient of friction μ of the fibers, which in turn also increases the required load to tighten the knotted rhombuses.

4.5.3 Effects of Varying Microscale Feature Sizes and Aging

In previously reported architected materials, smaller-is-stronger size effects have been previously shown with a mechanism that relies on utilizing constituent materials with changing bulk mechanical properties in sufficiently small feature sizes [96, 127, 130]. In contrast, the enhanced contact interactions unique to the knotted geometry offers new ways to induce size effects via size-dependent tribological phenomena. Treating friction between the knotted fibers as coulombic, where the friction force is proportional to the force normal to the friction surface, the knot model effectively predicts that the change in feature size will not affect the size-normalized load $\bar{F}$ as a function of ε, with all other parameters being equal. This prediction is confirmed by the close resemblance between $\bar{F}$ vs. ε data for pristine knotted rhombuses with $H = 70$ μm and $H = 140$ μm fabricated within two days of each other (Figure 4.10b and Supplementary Movie 8). Any potential of material size effects between these two rhombus sizes can be ruled out by the similarities in the $\bar{F}$ vs. ε data.

Tensile experiments on the aged woven frames also do not show any dependence on rhombus size. Compared to the ~14% increase in $\bar{F}$ at failure between pristine and 5-hr UV-irradiated woven samples from the same batch (Figure 4.7a), the increase in $\bar{F}$ at failure between all pristine and aged woven rhombuses is ~27% less, indicating that the bulk tensile properties of aged IP-Dip are closer to the properties of pristine IP-Dip than the UV-irradiated one. For the knotted samples, similarities between $\bar{F}$ vs. ε data within the fiber alignment regime of equivalently-sized pristine and aged rhombuses suggest that the similarities in the mechanical properties of their constituent materials holds. The higher loads in aged knotted frames compared to pristine ones of the same size may have been caused by an increase in surface friction due to environmentally–induced changes in surface properties. A substantial increase in friction interaction can lead to a sufficiently large increase in required load for fiber tightening, leading to sticking behaviors and early failures. Full quantification of the effects of environmental parameters on the mechanical behavior of hierarchical intertwined structures will require a suite of systematically controlled aging experiments within the same batch to rule out sample-to-sample variability.

Chapter 5

SIZE EFFECTS IN FRICTIONAL ARCHITECTED MATERIALS

This chapter is adapted from:

W.P. Moestopo, W. Deng, & J.R. Greer. "Adhesion-Friction Size Effects in Mechanical Metamaterials". In preparation.
CONTRIBUTIONS: Conceived the project, derived the analytical model, designed the samples, fabricated a portion of the samples, analyzed the data, and wrote the manuscript.

5.1 Chapter Summary

Further explorations into unique mechanisms and architectures possessed by natural materials have inspired the creation of human-made materials with unique functionalities and superb mechanical properties. Reducing the length scale of the smallest surface structures in animal body parts has been shown to allow animals to increase friction and attach to objects better via the maximization of surface forces, yet the performance of frictional architected materials seems to be size agnostic. Here, we utilize well-known contact mechanics and adhesion models to explore the influence of the size of structural elements in a frictional architected material on its energy dissipation capability. Our model shows that the loss factor of our frictional architected material can be >250% higher when it is scaled down from the mm-scale to the sub-micron length scale. The work of adhesion γ is deemed to be the most important factor in determining the existence of size effects in our frictional architected material framework. This work shows the potential of producing materials with high and tunable energy absorption, as well as shape-retention capability, via carefully architected structural elements.

5.2 Introduction: Unique Mechanical Properties Emerging from Hierarchical Surface Structures

As human understanding of natural materials continues to grow with the help of powerful characterization techniques, we learn that natural materials are able to achieve their remarkable functionalities using unique combinations of mechanisms, architectures, and constituent materials. For example, active tuning of nanocrystal spacing in chameleon skin enables camouflage [131] while mechanical instability allows the Venus flytrap to quickly capture its prey [132]. Unique architectures across various length scales have also allowed nacre [70, 133, 134], wood [135], mantis shrimp [67, 136], scorpion [137], diatom [3, 138], red-bellied woodpecker [139], and diabolical ironclad beetle [140], to name a few, to have structural parts composed of materials that are lightweight yet stiff, strong, and/or tough. The building blocks of these organisms have inspired novel architected material designs that are functional and mechanically stable [7, 9, 42, 122, 141–143].

In the nascent field of frictional architected materials, structures that are specifically designed to dissipate energy via friction mechanisms have been realized [120, 121, 144]. Friction force has been treated as proportional to the normal force in these works, and it is suggested that the energy dissipation capability of frictional architected materials is independent of its size with other conditions and parameters being equal. In this work, we are inspired by the hierarchical architecture of gecko feet which allows geckos to climb walls and walk on ceilings by maximizing short-range van der Waals interactions between the feet and walking surface [145, 146]. Simple planar structures mimicking gecko feet have been engineered [147, 148], but here we extend the application of contact mechanics models that take into account adhesion to the field of three-dimensional (3D) architected materials. We first show through analytical modeling that if friction interactions follow Amontons-Coulomb laws of friction, our frictional architected material framework is predicted to also be size agnostic. Modeling friction interactions using well-known contact mechanics models shows that the energy dissipation capability of our frictional architected material can be increased by more than 250% when the length scale of the structural components is scaled down from the mm-scale to within 100 nm.

5.3 Analytical Model to Study Adhesion-Friction Size Effects in Architected Materials

To elucidate the fundamental effects of the length scale of the frictional element upon the mechanical behaviors of architected materials, we begin by considering a simple unit cell first introduced by Garland et al. [120] consisting of a honeycomb ("hex") unit cell with friction elements added. When deformed, frictional elements will make contact with a base and dissipate energy before returning to undeformed configurations upon unloading. While Garland et al. assumed the frictional elements to follow Coulomb friction interaction, leading to a 2D design extruded to a thickness d, we designed frictional elements composed of bending arms with spherical ends to allow us to model the contact interaction as a circular contact (Figure 5.1). To simplify our first model, we assume the contact surfaces to be smooth, rendering effects of surface roughness negligible. While the DMT model can be applied in the same way, here we show the application of the JKR model in our frictional unit cell since it is deemed more suitable to the resulting contact events between polymeric structural elements in our experiments.

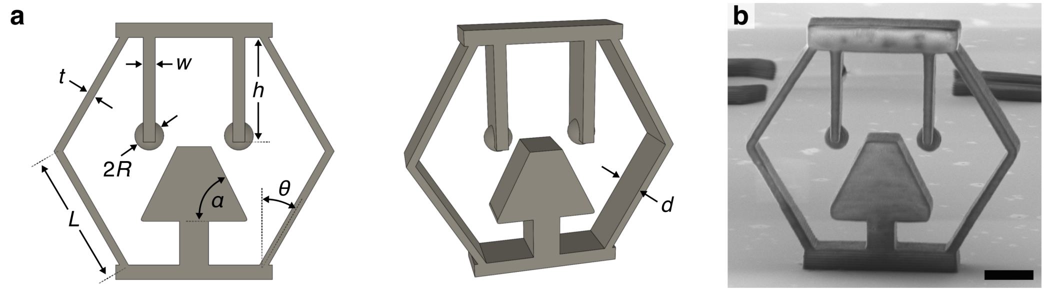

Figure 5.1: Design of a frictional unit cell with a sphere on the end of each frictional arm. a) Geometrical parameters of the frictional unit cell. b) Scanning electron microscope (SEM) image of a micro-sized additively manufactured frictional unit cell. Scale bar is 5 μm.

We model half of the frictional unit cell as shown in Figure 5.2a and use a symmetry argument along the vertical axis (v-axis) dividing the frictional unit cell in half to obtain the relevant forces and displacement values for the whole unit cell. When Amontons-Coulomb friction laws are applied, the relationship between the friction force on the sphere, F_f, and the normal force exerted on the sphere by the base, F_n, is modeled such that

$$F_f = \mu \cdot F_n, \tag{5.1}$$

where μ is the dynamic coefficient of friction. As we consider nano-scale contact area, the friction force can instead be modeled as

$$F_f = \tau \cdot A, \tag{5.2}$$

where τ is the interfacial shear strength and A is the interfacial contact area [149]. Assuming a circular contact area between the sphere of the frictional arm and the base, Equation 5.2 becomes

$$F_f = \tau \cdot \pi r^2, \tag{5.3}$$

and r can be modeled using the JKR method as

$$r = r\left(R, F_f, \gamma, K\right) = \left(\frac{R}{K}\left(F_n + 3\gamma\pi R + \sqrt{6\gamma\pi R F_n + (3\gamma\pi R)^2}\right)\right)^{1/3}, \tag{5.4}$$

$$K = \frac{4}{3}\left(\frac{1-\nu_1^2}{E_1} + \frac{1-\nu_2^2}{E_2}\right)^{-1}, \tag{5.5}$$

where R is the radius of the sphere, γ is the work of adhesion (or Dupré energy of adhesion), ν is the Poisson's ratio of the constituent material, E is the Young's Modulus of the constituent material, and 1 and 2 denote the base and the frictional arm, respectively.

Assuming that the friction base is rigid, the displacement of the sphere in the x-direction (δ_x) and the sliding distance of the sphere on the base (δ_{slid}) have the following relations:

$$\delta_x = \frac{\delta}{\tan(\theta)} = \delta\cot(\theta), \tag{5.6}$$

$$\delta_{slid} = \frac{\delta}{\sin(\theta)} = \delta\csc(\theta), \tag{5.7}$$

where δ is the honeycomb displacement in the y-direction and θ is the base angle as shown in Figure 5.2. If we cannot assume a rigid base, we can model the deformation of the base and the sphere according to the JKR model.

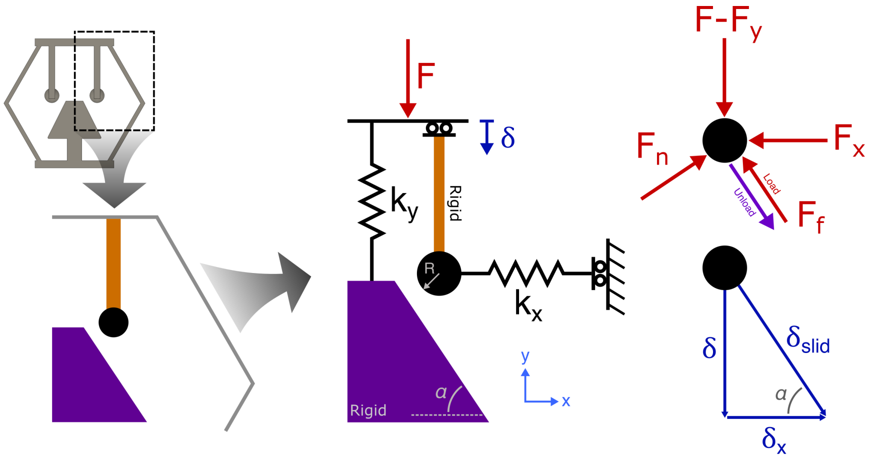

Figure 5.2: Force balance in half of the frictional unit cell (colored in ube boba milk tea color scheme) along with variables used in the model. By using a symmetry argument along the vertical axis dividing the frictional unit cell in half, we model the full frictional unit cell by treating k_y as the hexagon honeycomb stiffness in the y-direction and k_x as twice the bending stiffness of the frictional arm.

Since the direction of the friction force F_f is dependent on the loading direction (Figure 5.2b), we can obtain two different sets of equilibrium equations depending on whether the frictional unit cell is being loaded in compression or unloaded. During loading, the equilibrium equations are as follows:

$$F_x = k_x \cdot \delta \cot(\theta) = F_n \sin(\theta) - F_f \cos(\theta), \tag{5.8}$$

$$F = F_y + F_n \cos(\theta) + F_f \sin(\theta) = (k_y \cdot \delta) + F_n \cos(\theta) + F_f \sin(\theta), \tag{5.9}$$

where k_x is the stiffness in the x-direction analogous to the bending stiffness of the friction arm, k_y is the stiffness in the y-direction analogous to the honeycomb compressive stiffness, and F is the compression force aligned with the y-axis that is exerted on the unit cell. By using symmetry argument, we can combine two unit cell halves into one model by taking k_x as twice the bending stiffness of the friction arm while still treating k_y as the honeycomb compressive stiffness and F as the exerted compressive force on the unit cell. During unloading, the equilibrium equations become:

$$F_x = k_x \cdot \delta \cot(\theta) = F_n \sin(\theta) + F_f \cos(\theta), \tag{5.10}$$

$$F = F_y + F_n \cos(\theta) - F_f \sin(\theta) = (k_y \cdot \delta) + F_n \cos(\theta) - F_f \sin(\theta). \tag{5.11}$$

We have now found three equations (Equation 5.3 (adhesion-based model) or Equation 5.1 (Coulomb friction model), and two equilibrium equations) to calculate the values of four variables (F, F_f, F_n, δ). Note that the values of k_x and k_y can be calculated based on the geometry and constituent material properties of the frictional unit cell. If the base cannot be assumed as rigid and JKR/DMT contact model is used to model the deformation of the base and the sphere, the formulation will generate an equal number of equations and unknown variables, thus still allowing us to calculate the four aforementioned variables. To obtain the values for the other three unknown variables, we can prescribe values for either F or δ. In this work, we set the value of δ to ease the calculation for energy-related variables. One particular variable of interest is the loss coefficient η defined as

$$\eta = \frac{U_{dissipated}}{2\pi U_{elastic}}, \tag{5.12}$$

where $U_{dissipated}$ and $U_{elastic}$ are the dissipated energy within one loading-unloading cycle and the maximum stored elastic energy within one cycle, respectively, calculated as follows:

$$U_{dissipated} = \oint F \, d\delta = \int_0^{\delta^*} F_l \, d\delta - \int_0^{\delta^*} F_{unl} \, d\delta, \tag{5.13}$$

$$
\begin{aligned}
U_{elastic} &= \int_0^{\delta^*} (k_y \cdot \delta)\, d\delta + \int_0^{\delta_x^*} (k_x \cdot \delta_x)\, d\delta_x \\
U_{elastic} &= \int_0^{\delta^*} \left(k_y \cdot \delta + k_x \cdot \delta \cot^2(\theta)\right)\, d\delta.
\end{aligned} \tag{5.14}
$$

Here, δ^* and δ_x^* are the maximum honeycomb displacement and maximum δ_x within one cycle, respectively, F_l is F during loading, and F_{unl} is F during unloading. The formulation of η in Equation 5.12 can be interpreted as an approximation to the $\tan(\delta)$ variable commonly obtained from a dynamic mechanical analysis (DMA) testing [46]. Here, δ refers to the phase lag between the load and displacement signals during a cyclic testing on the material of interest, and theoretically, the variable $\tan(\delta)$ equals to the ratio of the loss modulus to the storage modulus.

To allow comparison between unit cells of various sizes, we introduce the scaling factor λ and calculate the isometric (i.e., having equal volume and amount of material) force F' as

$$F' = \lambda^2 F \tag{5.15}$$

when comparing one unit cell that has been scaled by a factor of λ to another unit cell. The number of cells N inside an isometric volume is $N = \left(\frac{1}{\lambda}\right)^3$.

As an alternative, we can compare the mechanical behaviors of frictional unit cells of varying sizes by calculating the normalized force σ' and the normalized displacement ε' as

$$\sigma' = \frac{F}{ld}, \tag{5.16}$$

$$\varepsilon' = \frac{\delta}{H}, \tag{5.17}$$

and calculate the energy terms as

$$\eta = \frac{W_{dissipated}}{2\pi W_{elastic}}, \tag{5.18}$$

$$W_{dissipated} = \oint \sigma'\, d\varepsilon', \tag{5.19}$$

$$W_{elastic} = \int_0^{\varepsilon'^*} \sigma'\, d\varepsilon', \tag{5.20}$$

where l and H are the length and height of the frictional unit cell, respectively, $W_{dissipated}$ is the dissipated energy density within one loading-unloading cycle, $W_{elastic}$ is the maximum stored elastic energy density within one cycle, and ε'^* is the maximum normalized displacement within one cycle.

5.4 Potential Size Effects Arising from Contact Interactions

5.4.1 Size Agnosticity in Coulomb Friction-Based Model

Previous work on "hex" frictional unit cell by Garland et al. [120] suspects that treating friction as Coulomb friction would result in size agnosticity (i.e., independent of size) in energy absorption assuming all else equal. In our experimental results from our work on hierarchical knotted materials [144], we showed that tensile behaviors of complex hierarchical knotted structures are identical despite having linear dimensions that differ by a factor of 2, thus matching what is predicted using a mechanical model on long overhand knots. Here, we will show that a Coulomb friction treatment on the contact interactions between frictional elements in our frictional unit cell also predicts size agnosticity.

We first solve for F for a given δ by using Equations 5.1, 5.8–5.11 to be able to compare the resulting loss factor from proportionally scaling the linear dimensions of the frictional unit cell. We obtain the loading force based on Coulomb friction $F_{l,C}$ and unloading force based on Coulomb friction $F_{unl,C}$

$$F_{l,C} = \delta \left(k_y + \frac{k_x \cos(\theta) \cdot (\cot(\theta) + \mu)}{\sin(\theta) - \mu \cos(\theta)} \right), \tag{5.21}$$

$$F_{unl,C} = \delta \left(k_y + \frac{k_x \cos(\theta) \cdot (\cot(\theta) - \mu)}{\sin(\theta) + \mu \cos(\theta)} \right). \tag{5.22}$$

We now consider the influence of varying linear dimensions on k_x and k_y assuming small displacements. By modeling the frictional arm as a classical cantilever beam [150] of length h with a constant rectangular cross-section of width w and thickness d, we obtain

$$\delta_x = \frac{F_x h^3}{3EI} = \frac{4 F_x h^3}{E d w^3}, \tag{5.23}$$

$$B = \frac{F_x}{\delta_x} = \frac{E d w^3}{4h^3}. \tag{5.24}$$

where I is the moment of inertia of the cross-sectional area of the cantilever beam about the neutral axis ($I = \frac{d \cdot w^3}{12}$) and B is the bending stiffness of the cantilever beam (frictional arm). Since we use a symmetry argument along the v-axis to model the full unit cell, we can calculate k_x as

$$k_x = 2B = 2\frac{E d w^3}{4h^3}. \tag{5.25}$$

To calculate k_y, we utilize a model for open hexagonal honeycomb with slender beams developed by Gibson et al. [25] that treats each cell wall as a separate cantilever beam:

$$\delta = \frac{FL^3 \sin^2(\theta)}{12EI} = \frac{FL^3 \sin^2(\theta)}{Edt^3}, \tag{5.26}$$

$$k_y = \frac{F}{\delta} = \frac{Edt^3}{L^3 \sin^2(\theta)}. \tag{5.27}$$

As we scale the linear dimensions of all geometrical parameters by a constant λ, the unit cell stiffnesses become

$$k_x \longrightarrow k'_x = 2\frac{E(\lambda \cdot d)(\lambda \cdot w)^3}{4(\lambda \cdot h)^3} = 2\lambda \frac{Edw^3}{4h^3} = \lambda \cdot k_x, \tag{5.28}$$

$$k_y \longrightarrow k'_y = \frac{E(\lambda \cdot d)(\lambda \cdot t)^3}{(\lambda \cdot L)^3 \sin^2(\theta)} = \lambda \frac{Edt^3}{L^3 \sin^2(\theta)} = \lambda \cdot k_y, \tag{5.29}$$

where k'_x and k'_y are the x- and y-stiffness components of the scaled unit cell, respectively. Here, we note that k_x and k_y also scale linearly with λ. Plugging in Equations 5.28 and 5.29 to Equations 5.21 and 5.22 result in scaled loading ($F'_{l,C}$) and unloading ($F'_{unl,C}$) forces

$$F'_{l,C} = \delta\lambda \left(k_y + \frac{k_x \cos(\theta) \cdot (\cot(\theta) + \mu)}{\sin(\theta) - \mu \cos(\theta)} \right), \tag{5.30}$$

$$F'_{unl,C} = \delta\lambda \left(k_y + \frac{k_x \cos(\theta) \cdot (\cot(\theta) - \mu)}{\sin(\theta) + \mu \cos(\theta)} \right). \tag{5.31}$$

We now compare the loss factor of one unit cell (η_1) to another that is scaled by λ (η_λ), both cyclically compressed to a certain effective strain $\varepsilon = \frac{\delta}{h} = \frac{\lambda\delta}{\lambda h}$:

$$\frac{\eta_1}{\eta_\lambda} = \frac{\frac{\oint F\, d\delta}{2\pi U_{elastic}}}{\frac{\oint F'\, d\delta}{2\pi U'_{elastic}}}, \tag{5.32}$$

where F' is the y-direction force on the honeycomb and $U'_{elastic}$ is the maximum elastic energy of the scaled unit cell. Inserting Equations 5.13-5.14, 5.21-5.22, and 5.28-5.31 to Equation 5.32 and calculating the integrations in η and η_λ up to $\delta^* = \varepsilon h$ and $\delta^* = \lambda\varepsilon h$, respectively, result in

$$\frac{\eta_1}{\eta_\lambda} = \frac{\eta_1}{\frac{\lambda^3}{\lambda^3}\eta_\lambda} = 1, \tag{5.33}$$

which means that loss factor η of our frictional unit cell is projected to be size-agnostic if the contact interactions follow Amontons-Coulomb friction laws.

5.4.2 Influence of Varying Surface Properties

When the length scale of contacting elements and surfaces becomes very small, Amontons-Coulomb friction laws can fail due to the presence of strong adhesion induced by forces such as van der Waals forces [151]. Our model, described earlier in this chapter, predicts that there can be pronounced size effects in the energy dissipation capability of the frictional architected material as work of adhesion λ increases and the unit cell size is scaled down. For the rest of the chapter, the standard-sized ($\lambda = 1$) frictional unit cell possesses the following geometrical parameters: honeycomb wall thickness $t = 0.8$ µm, honeycomb wall length $L = 14$ µm, unit cell thickness $d = 5$ µm, sphere radius $R = 1.5$ µm, frictional arm width $w = 1.25$ µm, frictional arm length $h = 10.8$ µm, $\theta = 30°$, and $\alpha = 63.43°$ (see Figure 5.1 for a visual representation of the geometrical parameters). The constituent material is modeled to have $E = 3$ GPa and $\nu = 0.49$, within the range of values for fabricated polymeric pillars made using two-photon lithography [152]. Wolfram Mathematica Version 12 software was used to calculate the analytical results.

Figure 5.3 shows the progression of loss factor η and normalized loss factor $\bar{\eta}$, which is η normalized by the loss factor at scale factor $\lambda = 1000$ and work of adhesion $\gamma = 0.01\frac{J}{m^2}$, with varying λ and γ values while all other parameters are held constant. To give an idea of what the scale factor represents, $\lambda = 1$ means the geometrical values in the previous paragraph are maintained, which include having honeycomb wall thickness and frictional arm width within ~ 1 µm unless otherwise noted. $\lambda = 10^3$ corresponds to a unit cell that is 10^3 times larger in each linear dimension and whose t and w are within ~ 1 mm. Similarly, $\lambda = 10^{-1}$ corresponds to a unit cell that is 10^{-1} times the size in each linear dimension and whose t and w are within ~ 100 nm. Moreover, to give an idea of what the work of adhesion γ values represent, $\gamma = 0.01\ \frac{\mathrm{J}}{\mathrm{m}^2}$ is within the range of van der Waals forces between hydrocarbons while common adhesives have $\gamma > 1\ \frac{\mathrm{J}}{\mathrm{m}^2}$.

Figure 5.3 shows that the loss factor η can increase by >250% when a mm-sized frictional unit cell is scaled down such that the wall and beam thicknesses are within 100 nm. This increase is more pronounced when the work of adhesion is sufficiently high ($>\gamma = 0.1\ \frac{\mathrm{J}}{\mathrm{m}^2}$) and the geometrical length scale is under the µm-scale ($\lambda < 1$). To understand this phenomenon better, we plot the values for each force component in our model up to the maximum compressive cyclic strain of $\varepsilon = 20\%$ for frictional unit cells of $\gamma = 1\frac{J}{m^2}$ and varying sizes (Figure 5.4). As the scale factor becomes smaller, the graphs show (i) larger gaps between loading (F_{load}) and unloading forces

(F_{unload}) corresponding to larger levels of friction force F_r compared to normal force F_n, and (ii) increases in the y-intercept values for loading force on the honeycomb F_{load} and F_r, as well as the x-intercept values for unloading force F_{unload}. These effects are more pronounced in the one order of magnitude drop between $\lambda = 1$ to $\lambda = 0.1$ than in the three orders of magnitude drop between $\lambda = 10^3$ and $\lambda = 1$. To provide more quantitative comparisons beyond η values, we can use Equation 5.15 to compare the force response of the frictional architected material with varying unit cell sizes but of the same volume and mass. Such comparisons would show that as the size of the frictional unit cell in Figure 5.4 is reduced, the isometric compressive force at maximum strain ($\varepsilon = 20\%$) increases.

Larger gaps between F_{load} and F_{unload} compared to the overall loading-unloading force levels mean that more energy is dissipated for a given elastic strain energy retained by the unit cell when it is deformed (i.e., larger $U_{dissipated}$ compared to $U_{elastic}$). Moreover, a higher isometric F_{load} y-intercept means there is a higher threshold force to start deforming the unit cell, while a higher isometric F_{unload} x-intercept means that the unit cell may be able to retain its shape around this x-intercept value. To bring the unit cell back to zero strain from this x-intercept value, a negative F_{unload} (pulling force) will need to be exerted.

Such pronounced differences in η and force values in Figures 5.3 and 5.4 as the size of the unit cell becomes smaller stem from higher adhesion effects predicted in the sub-micron regime. Figure 5.5 shows friction force F_r vs. normal force F_n graphs, up to the maximum predicted normal force, for corresponding frictional unit cells shown in Figure 5.4. Using $\gamma = 1 \frac{\mathrm{J}}{\mathrm{m}^2}$ and $\tau = 10$ MPa, we compare the predicted friction force to the Coulombic friction model with a dynamic coefficient of friction $\mu = 0.1$. At the mm-scale ($\lambda = 10^3$), F_r is slightly larger than the Coulombic friction value for F_n under ~11 N and becomes increasingly smaller than the Coulombic friction value for F_n over ~11 N. At the µm-scale ($\lambda = 1$), F_r is constantly higher than the Coulombic friction value with a y-intercept that is higher than 50% of the maximum predicted Coulombic friction. An even more pronounced difference is seen in the length scale of approximately 100 nm ($\lambda = 10^{-1}$), where the friction force predicted using the adhesion model is constantly more than twice as large as the maximum predicted Coulombic friction within one compressive cycle. Since the Coulombic friction is analogous to size agnosticity, Figure 5.5 shows that significantly higher energy dissipation via friction can be achieved as the length scale of the frictional unit cell reaches the sub-micron/nanometer regime.

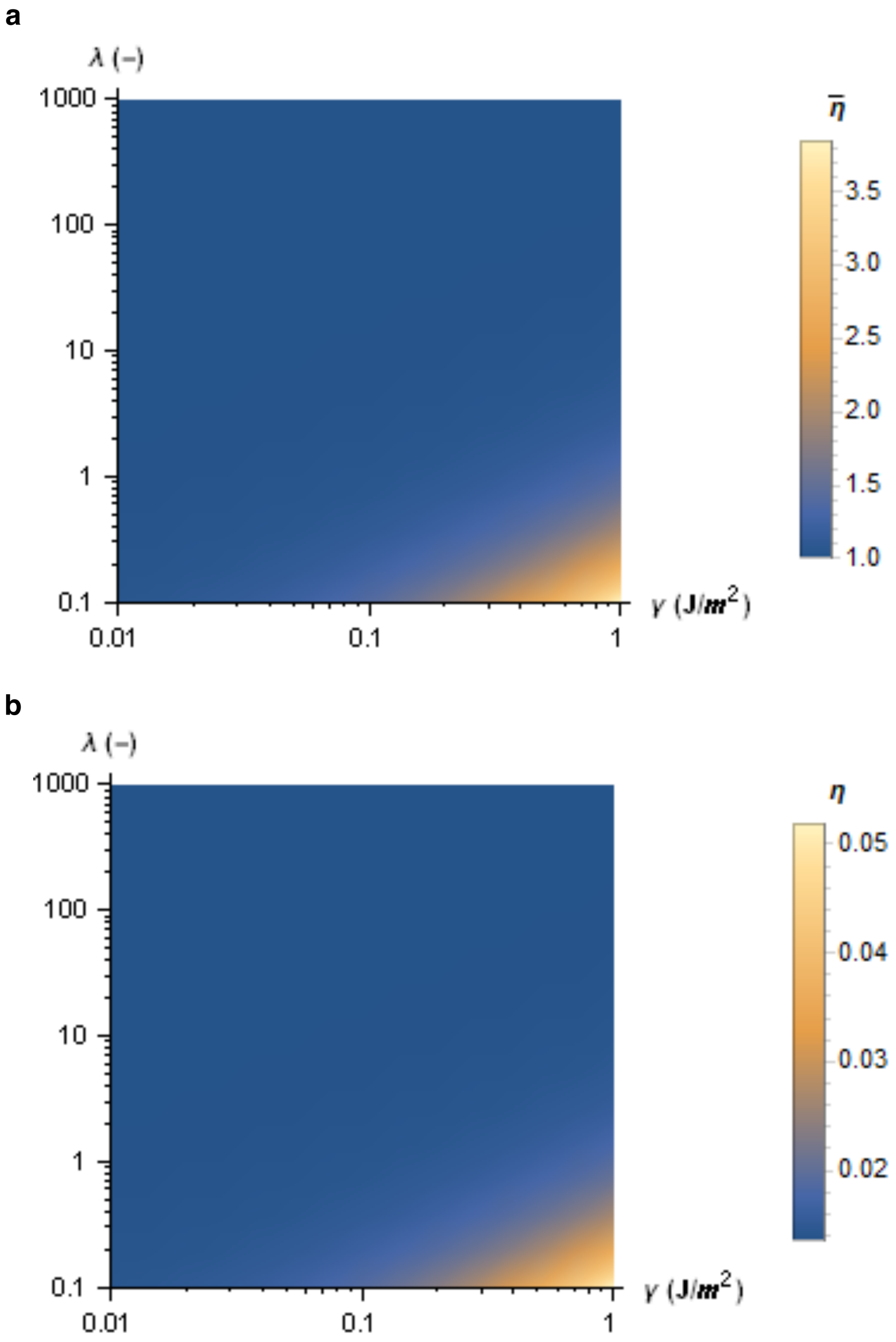

Figure 5.3: Prediction of size effects in frictional architected materials. a) Normalized loss factor $\bar{\eta}$, which is loss factor normalized by the loss factor at scale factor $\lambda = 1000$ and work of adhesion $\gamma = 0.01\frac{J}{m^2}$, as a function of λ and γ with interfacial shear strength $\tau = 10$ MPa and all other parameters held constant, showing >250% increase in η for $\gamma \sim 1\ \frac{\mathrm{J}}{\mathrm{m}^2}$ as the length scale of the frictional unit cell goes down from having beam thickness in the mm-scale ($\lambda = 1000$) to within 100 nm ($\lambda = 0.1$). b) Loss factor η as a function of λ and γ with constant $\tau = 10$ MPa. In the model, the frictional unit cell is cyclically compressed to $\varepsilon = 20\%$.

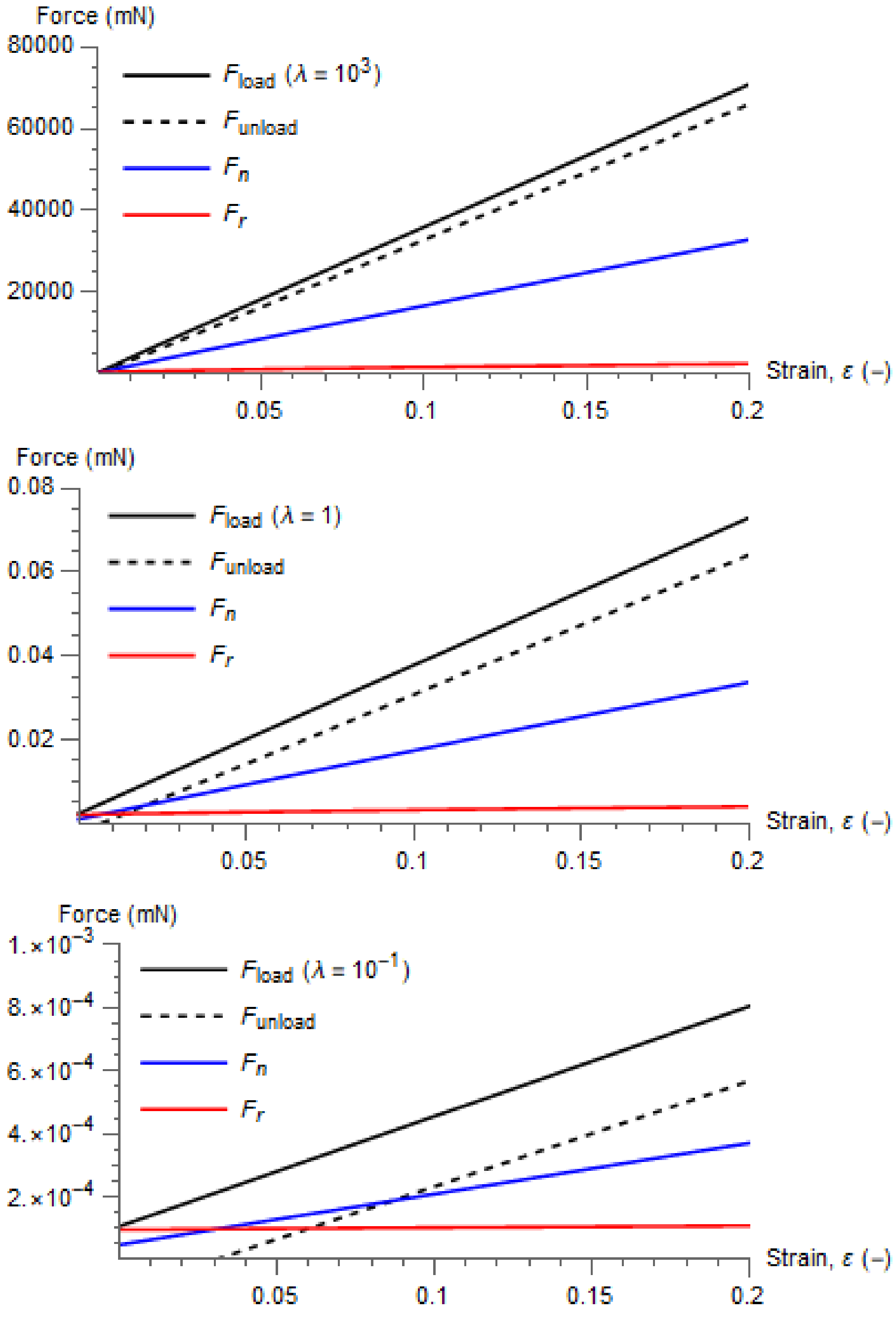

Figure 5.4: Force values vs. strain graphs up to $\varepsilon = 20\%$ of standard-geometry frictional unit cells with $\gamma = 1\ \frac{\text{J}}{\text{m}^2}$, $\tau = 10$ MPa, and varying scale factor λ. $\lambda = 10^3$, $\lambda = 1$, and $\lambda = 10^{-1}$ correspond to a unit cell with a hexagonal beam size on the order of 1 mm, 1 µm, and 100 nm, respectively.

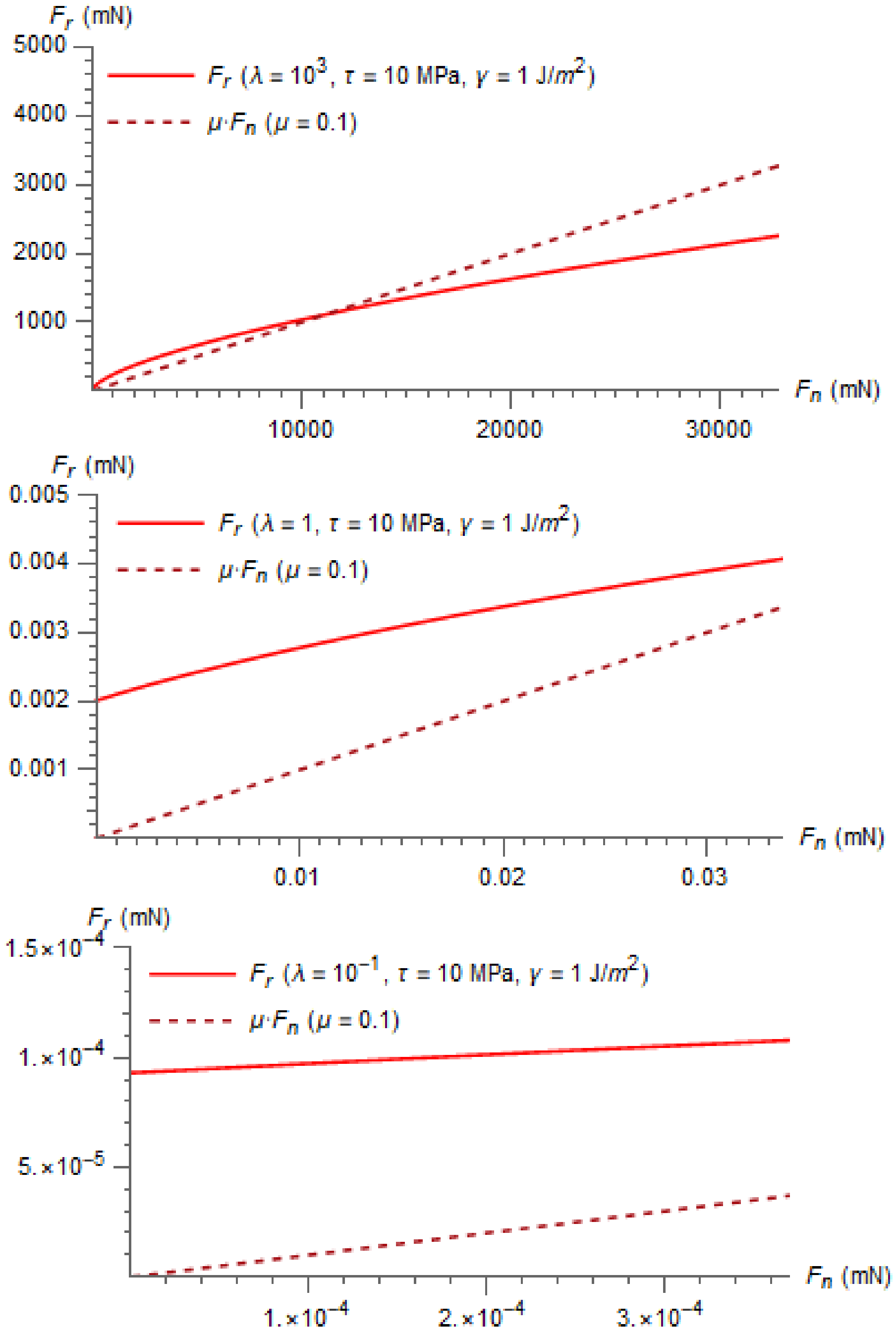

Figure 5.5: Friction force F_r vs. normal force F_n graphs up to maximum normal force values of corresponding structures modeled in Figure 5.4. Bold red lines correspond to friction force curves from the adhesion model, and red dashed lines correspond to Coulombic friction force curves with a dynamic coefficient of friction $\mu = 0.1$.

We now look into the effects of varying the interfacial shear strength τ. Figure 5.6 shows the progression of the loss factor with varying τ and shape factor λ with two different work of adhesion values: $\gamma = 0.01\ \frac{\mathrm{J}}{\mathrm{m}^2}$ in panel (a) and $\gamma = 1\ \frac{\mathrm{J}}{\mathrm{m}^2}$ in panel (b). We can observe that an increase in τ is generally followed by an increase in loss factor η, although meaningful size effect in η can only be observed for the case where $gamma = 1\ \frac{\mathrm{J}}{\mathrm{m}^2}$. These observations are consistent with Equations 5.2 and 5.4, where γ is predicted to be the most influential term in inducing size effect since it controls the contact area, whereas τ controls the force required to overcome friction based on a given contact area. An increase in τ should lead to higher friction, and therefore energy dissipation, but it does not lead to a size effect in η since the size effect arises due to an adhesion-induced increase in contact area relative to the unit cell size. Figures 5.7 and 5.8 further demonstrate these observations and explanation; there is no significant qualitative difference between the predicted force values in mm-scale and sub-micron frictional unit cells of $\gamma = 0.01\ \frac{\mathrm{J}}{\mathrm{m}^2}$ and constant τ, but there are noticeable differences between the force values of frictional unit cells of the same length scale but with varying τ values.

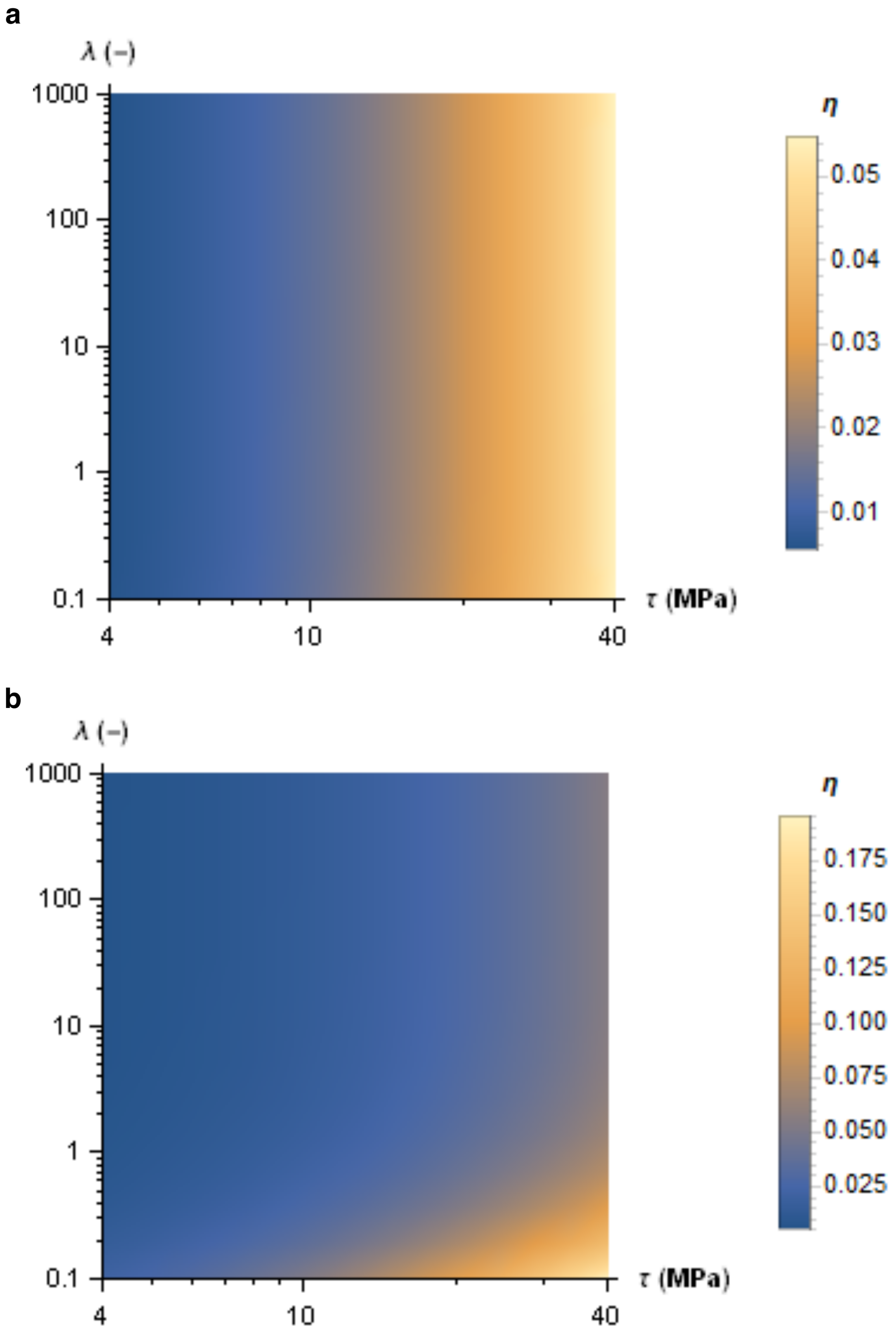

Figure 5.6: Influence of interfacial shear strength τ, work of adhesion γ, and size on the loss factor η of a frictional unit cell. a) η as a function of scale factor λ and τ with constant $\gamma = 0.01\ \frac{\mathrm{J}}{\mathrm{m}^2}$. b) Loss factor η as a function of scale factor λ and τ with constant $\gamma = 1\ \frac{\mathrm{J}}{\mathrm{m}^2}$. In the model, the frictional unit cell is cyclically compressed to $\varepsilon = 20\%$.

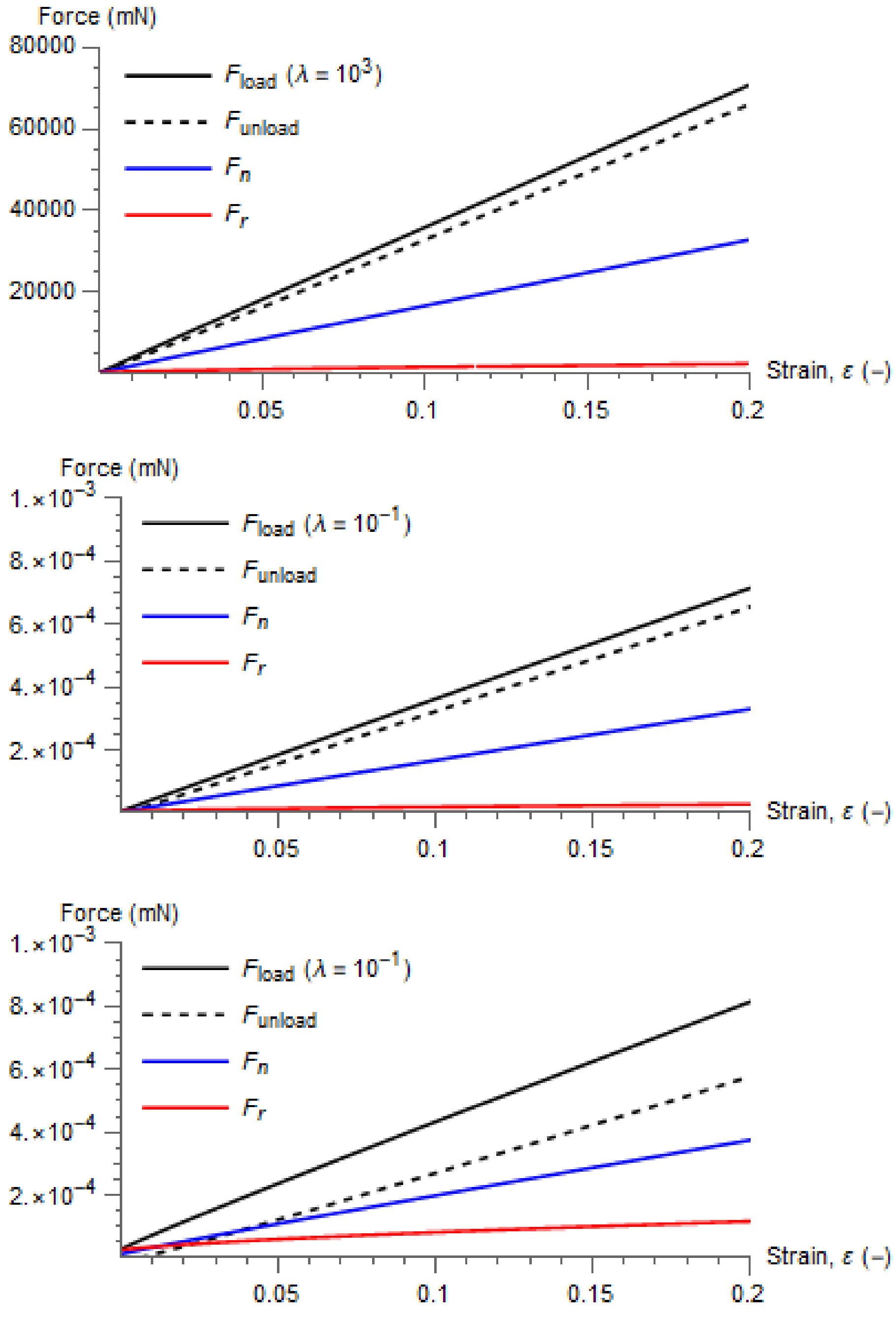

Figure 5.7: Force values vs. strain graphs up to $\varepsilon = 20\%$ of standard-geometry frictional unit cells with work of adhesion $\gamma = 0.01\ \frac{\mathrm{J}}{\mathrm{m}^2}$, and varying scale factor λ and interfacial shear strength τ. In (a-b), $\tau = 10$ MPa, whereas in (c), τ increases to 40 MPa. $\lambda = 10^3$, $\lambda = 1$, and $\lambda = 10^{-1}$ correspond to a unit cell with a hexagonal beam size on the order of 1 mm, 1 µm, and 100 nm, respectively.

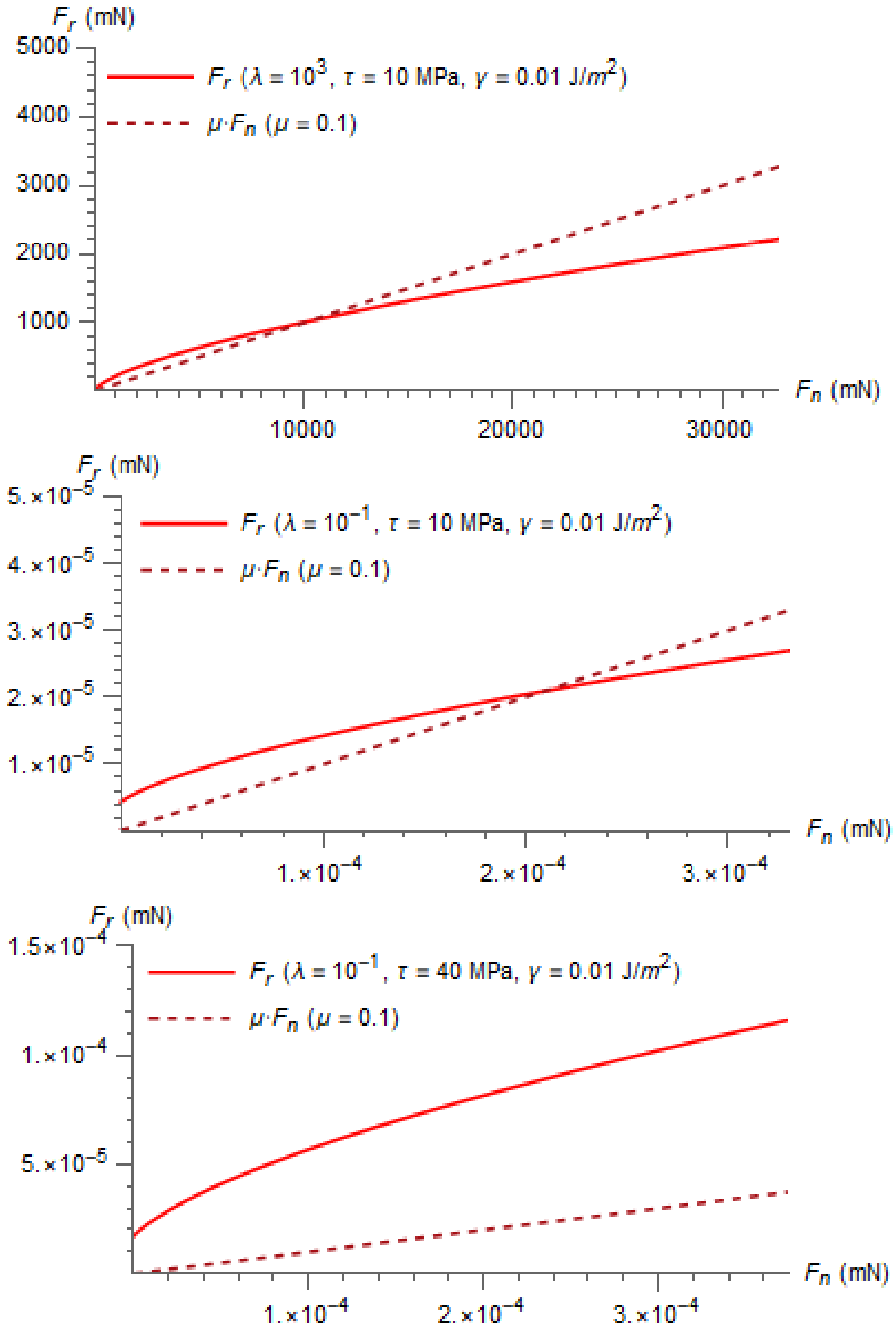

Figure 5.8: Friction force F_r vs. normal force F_n graphs up to maximum normal force values of corresponding structures modeled in Figure 5.7. Bold red lines correspond to friction force curves from the adhesion model, and red dashed lines correspond to Coulombic friction force curves with a dynamic coefficient of friction $\mu = 0.1$.

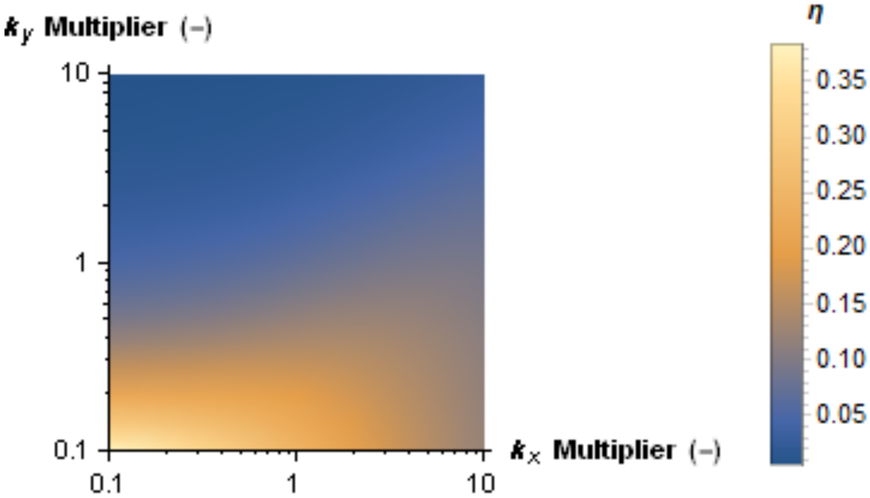

Figure 5.9: Influence of varying unit cell stiffness elements k_x and k_y on a standard-geometry frictional unit cell with scale factor $\lambda = 1$, interfacial shear strength $\tau = 40$ MPa, and work of adhesion $\gamma = 1\ \frac{\mathrm{J}}{\mathrm{m}^2}$. In the model, the frictional unit cell is cyclically compressed to $\varepsilon = 20\%$.

5.4.3 Influence of Geometrical Parameters

We also briefly study the influence of varying individual geometrical parameters within the frictional unit cells. In Figure 5.9, we show the progression of loss factor η as the unit cell stiffness elements k_x and k_y are multiplied by scalar k_x multiplier and k_y multiplier, respectively. We can observe from our model predictions that loss factor η can be increased by reducing unit cell stiffness elements k_x and k_y simultaneously. While reducing k_y, which is analogous to honeycomb stiffness, generally leads to a higher η, reducing k_x in the model independently does not always lead to a higher η as evidenced in the case where k_y is held constant at 1.

In terms of variance in sphere radius R and α, the trends in size effect are similar to that of interfacial shear strength τ where size effect on loss factor η is significantly driven by the work of adhesion γ. In Figure 5.10, although it can be observed that an increase in R generally leads to an increase in η, the progression of the η value as R increases is almost uniform across all shape factors for low γ. Meanwhile, size effect in η as R is multiplied by a higher multiplier value can be observed when γ is sufficiently large ($\gamma = 1\ \frac{\mathrm{J}}{\mathrm{m}^2}$). Similarly, a near-uniform progression of η across all scale factors as the friction base angle α increases is observed in Figure 5.11a for low γ value. Interestingly, the progression of η as α and λ are varied is more complex for the higher γ value (Figure 5.11b). For λ>1, η still gets larger as α

becomes more acute, but the trend seems to disappear if not reversed for $\lambda \rightarrow 0.1$. One potential explanation is that when adhesion is not as big of a factor (λ>1), the friction interaction behaves similarly to Coulombic friction (see examples in Figures 5.8a-b), thus resulting in a higher friction force when normal force also increases due to the friction arms being pushed against a more acute (less steep) friction base. Yet when adhesion becomes significant as $\lambda \rightarrow 0.1$, the friction arms can still experience a large friction force even at near-zero normal force (see example in 5.5c), which would be the case when the friction base is very steep. This adhesion-induced friction force seems to allow η to be optimized when the friction base is more steep, which should reduce the magnitude of the normal force F_n and the strain energy stored in the bending of friction arms.

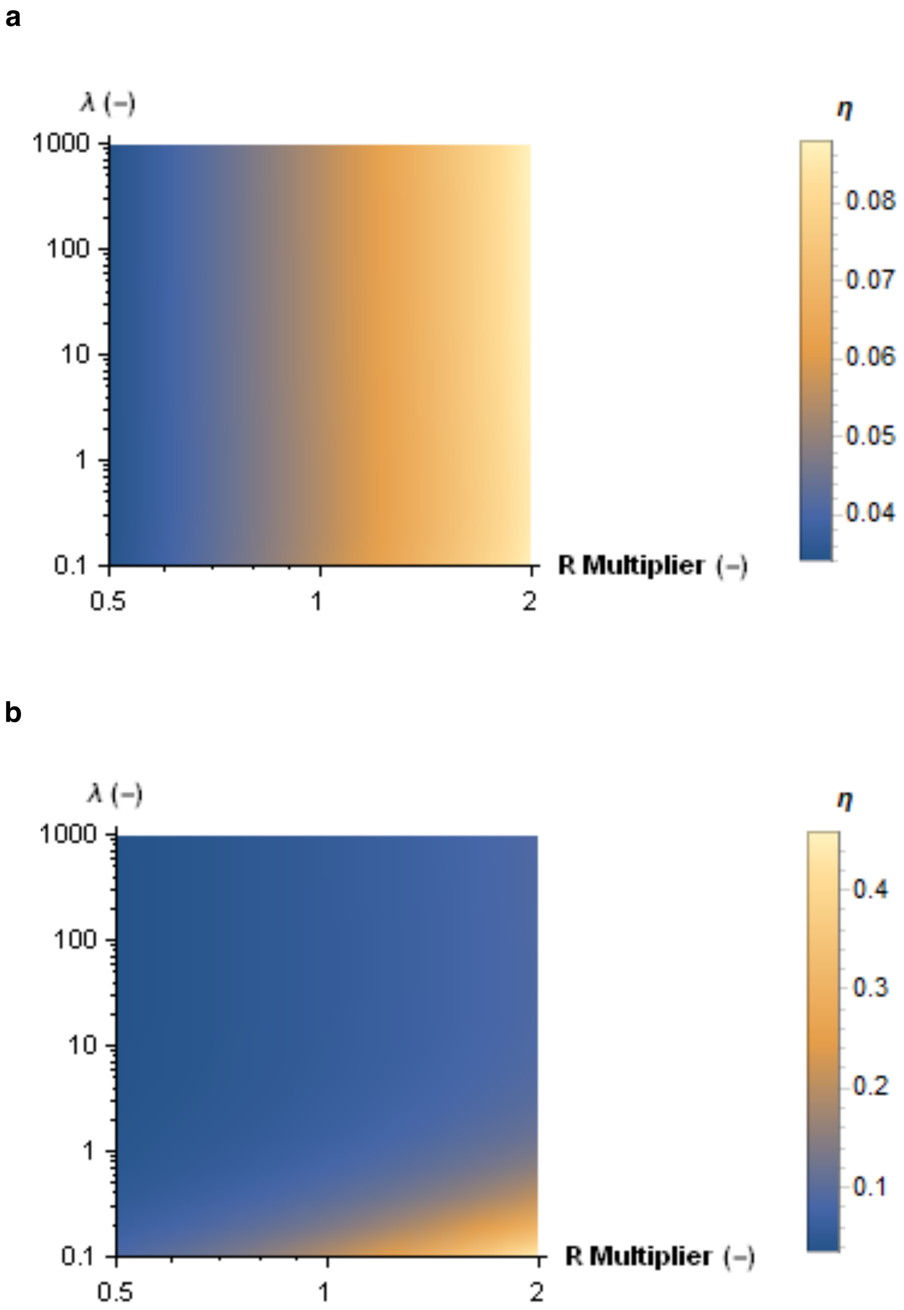

Figure 5.10: Influence of varying contacting sphere radius R and scale factor λ on the loss factor η of a standard-geometry frictional unit cell with interfacial shear strength $\tau = 40$ MPa and work of adhesion γ equal to a) 0.01 $\frac{\mathrm{J}}{\mathrm{m}^2}$, and b) 1 $\frac{\mathrm{J}}{\mathrm{m}^2}$. R multiplier is the value of a scalar multiplied to the value of R in the standard-geometry model. To calculate η, the frictional unit cell in the model is cyclically compressed to $\varepsilon = 20\%$.

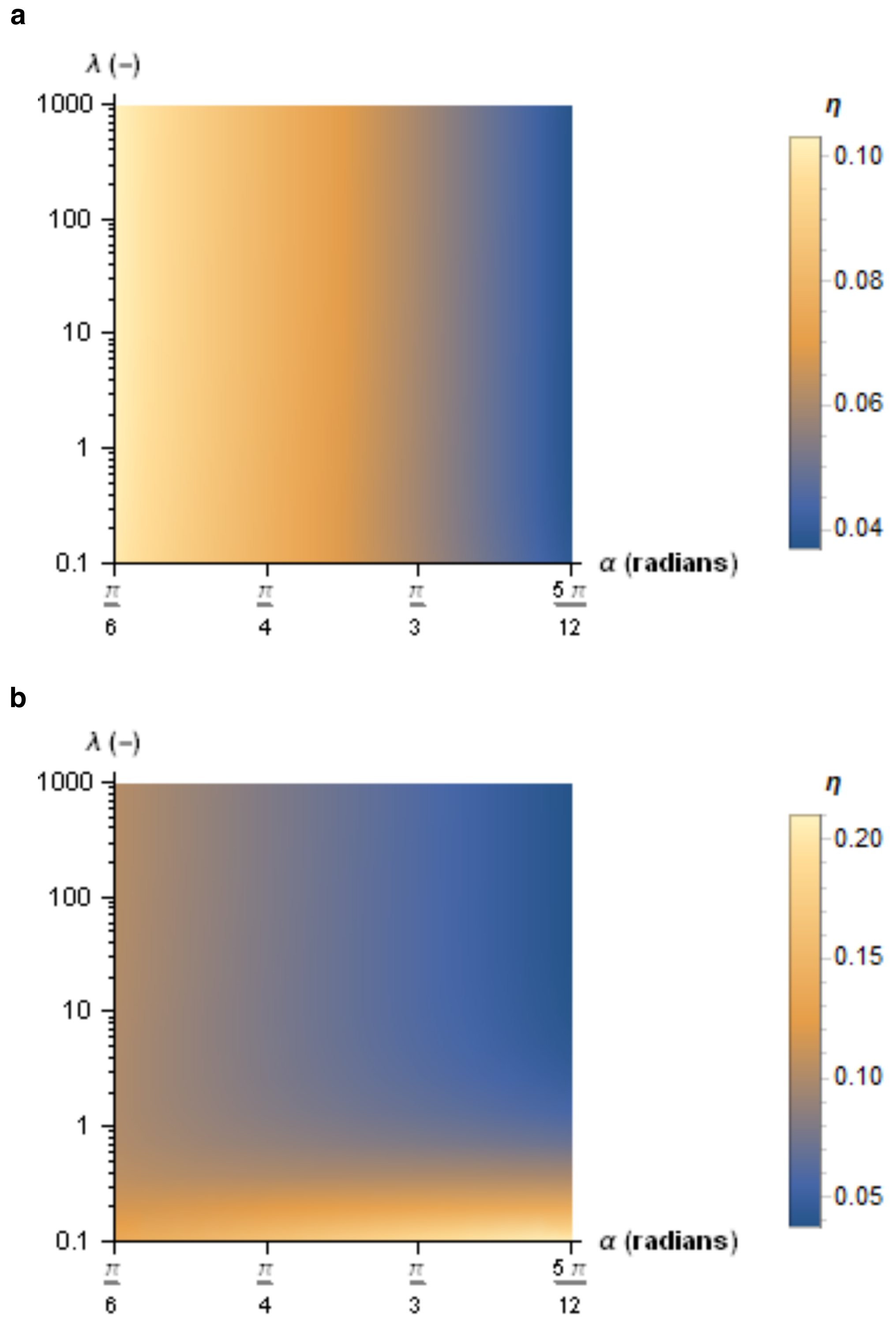

Figure 5.11: Influence of varying the angle of the surface of the friction base α and scale factor λ on the loss factor η of a standard-geometry frictional unit cell with interfacial shear strength τ = 40 MPa and work of adhesion γ equal to a) 0.01 $\frac{\mathrm{J}}{\mathrm{m}^2}$, and b) 1 $\frac{\mathrm{J}}{\mathrm{m}^2}$. In the model, the frictional unit cell is cyclically compressed to ε = 20%.

Chapter 6

SUMMARY AND OUTLOOK

6.1 Summary

In this thesis, we have explored the design space and characterized the mechanical properties of hierarchical intertwined materials. We show that by replacing monolithic beams and junctions in classical beam-based architected material design with intertwined fibers that form effective beams and junctions, we are able to produce architected materials that offer 2–3 times higher absorbed energy per cycle when normalized to the first cycle, >70% greater deformability upon tension, >50% compressive strain without catastrophic failure, and directional compliance unachievable in their monolithic counterparts. We then introduce knotted fiber topology into the hierarchical intertwined material framework capable of stable shape-retention, leading to ~92% increase in absorbed energy and up to ~107% increase in failure strain compared to woven structures.

By passivating and exposing our tested samples to UV light, we probe the behaviors of intertwined structures with different constituent material properties and discover that, to achieve optimal extensibility and energy dissipation, special attention will need to be given to the tensile strain at failure and friction properties of the constituent materials so that the intertwined materials would not experience failure before the knotting mechanism is activated. Agreements between experimental results for knotted structures and an analytical model for long overhand knots allow the model to be used as an aid in optimizing the mechanical behaviors of knotted structures, although we need to carefully consider the limitations of the model compared to intertwined structures which have more complex geometries and curvy undeformed configurations.

Moreover, analytical modeling of a simple hexagonal architected material with frictional elements shows that the energy dissipation capability of the architected material can be significantly enhanced even when density is kept constant by (i) increasing adhesion between the structural elements and (ii) reducing the feature size of the structural elements to the sub-micron scale. If the friction interaction between the structural elements follows classical Amontons-Coulomb laws of friction, the damping performance of the architected material is predicted to be independent of size. Meanwhile, if the friction interaction follows well-known contact mechanics models that take into account surface adhesion, size effects in energy dissipation are predicted to rise as the interfacial energy (work of adhesion) increases to 1 $\frac{\mathrm{J}}{\mathrm{m}^2}$ and above.

The unique deformation and energy absorption mechanisms demonstrated in this thesis unlock new ways to create shape-reconfigurable, highly extensible, and extremely energy absorbing bulk, 3D micro-architected materials with mechanical properties that can be tuned not only by their geometries and bulk constituent material properties but also by the surface-driven interactions among the structural elements. Beyond enabling the creation of flexible, tough, and lightweight 3D textiles, such capabilities can be advantageous in applications such as flexible electronics, hernia repair, and devices deployed in the bloodstream where repeated large deformations are encountered and traditionally stiff and brittle constituent materials still need to be incorporated.

6.2 Open Questions and Future Work

Intertwined and Frictional Architected Materials

The ability to design fibers with various combinations of pathways within the intertwined material provides a near limitless design space. While the general distinctions between knotted and woven fiber topologies have been explored within the context of building blocks for hierarchical intertwined materials, further studies on possible reconfiguration pathways that can be achieved within the hierarchical intertwined material framework may provide value, especially if these materials can be manufactured with conventional 3D weaving machines as opposed to additive manufacturing. Our exploration on intertwined and frictional architected materials also sheds light on the complexity of understanding contact interactions. In future works, it would be fruitful if researchers from the field of tribology and architected materials combine their expertise to understand the contact events that occur within the structural elements of 3D architected materials upon deformation and those that occur between the architected material structural elements and other objects of interest.

While our modeling work is able to predict size effects in energy absorption given self-similar unit cells of different sizes, the effects of surface roughness, adhesion, and adhesion hysteresis, among many others, still need to be explored within the context of architected materials with contact interactions; advancements in computational methods that can model contact and friction accurately and efficiently would assist these potential investigations greatly [153]. The enhanced energy dissipation exhibited by intertwined and frictional architected materials also shows that carefully designed friction mechanisms can potentially lead to materials with high fracture toughness and fatigue resistance. Instead of dissipating energy via plastic deformation, intertwined and frictional architected materials would be able to survive extreme loading conditions by dissipating energy via friction mechanisms, although explorations toward higher strain rate (for inspirations, see References [109, 154]) and carefully controlled environmental conditions will need to be conducted to fully understand their effects on the material performance. Moreover, the decoupling of relative density and compliance in intertwined materials also provides a pathway to design more sophisticated and more durable flexible and wearable electronics.

Coupling Novel Architectures with Stimuli-Responsivity

While recent progress in developing architected materials that are still static and passive (i.e., with set properties that cannot be changed after they have been fabricated) have been phenomenal, the ability to create synthetic materials that can change their properties in response to external stimuli are of great interest. In nature, stimuli-responsivity in living organisms, such as touch-sensitivity in plants [155], help them adapt and survive. When combined with mechanical instabilities arising from the organism architectures, even a small dose of stimulus could lead to a response in a larger dimension/length scale such as the snapping of the Venus flytrap upon touch [132]. Recent explorations into stimuli-responsive structures have utilized polymers due to their responsivity to biological, chemical, electromagnetic, acoustic, and light stimuli, among others [156]. Using advanced additive manufacturing techniques, researchers have been able to precisely program the shape-morphing of these printed polymers [157–163] as well as change the mechanical properties of the structures [164]. As more and more studies are conducted with a focus on contact interactions and stimuli-responsive materials, new phenomena may emerge when contact interactions are coupled with stimuli-responsivity. Potential applications for these stimuli-responsive structures include applications in drug delivery systems, smart textiles, adaptive pipes, self-assembly at large scales and in harsh environments, tissue engineering, as well as error-correct and self-repairing structures [165].

BIBLIOGRAPHY

1. Wegst, U. G., Bai, H., Saiz, E., Tomsia, A. P. & Ritchie, R. O. Bioinspired structural materials. *Nature Materials* **14,** 23–36. ISSN: 14764660 (2015).
2. Tertuliano, O. A. & Greer, J. R. The nanocomposite nature of bone drives its strength and damage resistance. *Nature Materials* **15,** 1195–1202. ISSN: 14764660 (Nov. 2016).
3. Aitken, Z. H., Luo, S., Reynolds, S. N., Thaulow, C. & Greer, J. R. Microstructure provides insights into evolutionary design and resilience of Coscinodiscus sp. frustule. *Proceedings of the National Academy of Sciences of the United States of America* **113,** 2017–2022. ISSN: 10916490. `www.pnas.org/cgi/doi/10.1073/pnas.1519790113` (2016).
4. Schaedler, T. A. *et al.* Ultralight metallic microlattices. *Science* **334,** 962–965. ISSN: 10959203. `https://www.science.org/doi/full/10.1126/science.1211649` (Nov. 2011).
5. Meza, L. R., Das, S. & Greer, J. R. Strong, lightweight, and recoverable three-dimensional ceramic nanolattices. *Science (New York, N.Y.)* **345,** 1322–6. ISSN: 1095-9203. `http://www.ncbi.nlm.nih.gov/pubmed/25214624` (2014).
6. Zheng, X. *et al.* Ultralight, ultrastiff mechanical metamaterials. *Science* **344,** 1373–1377. ISSN: 10959203 (2014).
7. Zheng, X. *et al.* Multiscale metallic metamaterials. *Nature Materials* **15,** 1100–1106. ISSN: 14764660 (Oct. 2016).
8. Dou, N. G., Jagt, R. A., Portela, C. M., Greer, J. R. & Minnich, A. J. Ultralow Thermal Conductivity and Mechanical Resilience of Architected Nanolattices. *Nano Letters* **18,** 4755–4761. ISSN: 15306992 (2018).
9. Meza, L. R. *et al.* Resilient 3D hierarchical architected metamaterials. *Proceedings of the National Academy of Sciences* **112,** 11502–11507. ISSN: 0027-8424. `http://www.pnas.org/lookup/doi/10.1073/pnas.1509120112` (2015).
10. Bertoldi, K., Vitelli, V., Christensen, J. & Van Hecke, M. Flexible mechanical metamaterials. *Nature Reviews Materials* **2.** ISSN: 20588437 (2017).
11. Krödel, S. & Daraio, C. Microlattice Metamaterials for Tailoring Ultrasonic Transmission with Elastoacoustic Hybridization. *Physical Review Applied* **6,** 1–4. ISSN: 23317019 (2016).
12. Celli, P. & Gonella, S. Manipulating waves with LEGO® bricks: A versatile experimental platform for metamaterial architectures. *Applied Physics Letters* **107,** 081901. ISSN: 0003-6951. `https://aip.scitation.org/doi/abs/10.1063/1.4929566` (Aug. 2015).

13. Kim, G., Portela, C. M., Celli, P., Palermo, A. & Daraio, C. Poroelastic microlattices for underwater wave focusing. *Extreme Mechanics Letters* **49,** 101499. ISSN: 2352-4316 (Nov. 2021).

14. Bückmann, T., Thiel, M., Kadic, M., Schittny, R. & Wegener, M. An elasto-mechanical unfeelability cloak made of pentamode metamaterials. *Nature Communications* **5,** 1–6. ISSN: 20411723 (2014).

15. Wang, L. *et al.* Mechanical cloak via data-driven aperiodic metamaterial design. *Proceedings of the National Academy of Sciences of the United States of America* **119.** ISSN: 10916490. `https://doi.org/10.1073/pnas.2122185119` (Mar. 2022).

16. Wang, Q. *et al.* Lightweight Mechanical Metamaterials with Tunable Negative Thermal Expansion. *Physical Review Letters* **117,** 1–6. ISSN: 10797114 (2016).

17. Daniel, I. M. & Ishai, O. *Engineering Mechanics of Composite Materials* `https://www.scholars.northwestern.edu/en/publications/engineering-mechanics-of-composite-materials` (Oxford University Press, 2006).

18. Lewis, J. A., Smay, J. E., Stuecker, J. & Cesarano, J. Direct Ink Writing of Three-Dimensional Ceramic Structures. *Journal of the American Ceramic Society* **89,** 3599–3609. ISSN: 0002-7820. `http://doi.wiley.com/10.1111/j.1551-2916.2006.01382.x` (Dec. 2006).

19. Tumbleston, J. R. *et al.* Continuous liquid interface production of 3D objects. *Science* **347,** 1349–1352 (Mar. 2015).

20. Toombs, J. T. *et al.* Volumetric additive manufacturing of silica glass with microscale computed axial lithography. *Science* **376,** 308–312. ISSN: 10959203. `https://www.science.org/doi/10.1126/science.abm6459` (Apr. 2022).

21. Bertsch, A., Lorenz, H. & Renaud, P. 3D microfabrication by combining microstereolithography and thick resist UV lithography. *Sensors and Actuators A: Physical* **73,** 14–23. ISSN: 0924-4247. `https://www.sciencedirect.com/science/article/pii/S0924424798002490` (Mar. 1999).

22. Sun, H. B., Matsuo, S. & Misawa, H. Three-dimensional photonic crystal structures achieved with two-photon-absorption photopolymerization of resin. *Applied Physics Letters* **74,** 786–788. ISSN: 00036951 (Feb. 1999).

23. Lakes, R. Materials with structural hierarchy. *Nature* **361,** 511–515. `http://silver.neep.wisc.edu/~lakes/Hierarch93.pdf` (1993).

24. Greer, J. R., Oliver, W. C. & Nix, W. D. Size dependence of mechanical properties of gold at the micron scale in the absence of strain gradients. *Acta Materialia* **53,** 1821–1830. ISSN: 13596454 (2005).

25. Gibson, L. J. & Ashby, M. F. *Cellular solids : structure and properties* 510. ISBN: 0521499119 (Cambridge University Press, 1997).

26. Fleck, N. A., Deshpande, V. S. & Ashby, M. F. Micro-architectured materials: Past, present and future. *Proceedings of the Royal Society A: Mathematical, Physical and Engineering Sciences* **466,** 2495–2516. ISSN: 14712946 (Sept. 2010).

27. Fleck, N. A. & Qiu, X. The damage tolerance of elastic-brittle, two-dimensional isotropic lattices. *Journal of the Mechanics and Physics of Solids* **55,** 562–588. ISSN: 00225096 (2007).

28. Deshpande, V. S., Ashby, M. F. & Fleck, N. A. Foam Topology Bending Versus Stretching Dominated Architectures. *Acta mater* **49,** 1035–1040. `www.elsevier.com/locate/actamat` (2001).

29. Shaikeea, A. J. D., Cui, H., O'Masta, M., Zheng, X. R. & Deshpande, V. S. The toughness of mechanical metamaterials. *Nature Materials 2022 21:3* **21,** 297–304. ISSN: 1476-4660. `https://www.nature.com/articles/s41563-021-01182-1` (Feb. 2022).

30. Deshpande, V. S., Fleck, N. A. & Ashby, M. F. Effective properties of the octet-truss lattice material. *Journal of the Mechanics and Physics of Solids* **49,** 1747–1769. ISSN: 00225096 (2001).

31. Pellegrino, S. & Calladine, C. R. Matrix analysis of statically and kinematically indeterminate frameworks. *International Journal of Solids and Structures* **22,** 409–428. ISSN: 00207683. `http://dx.doi.org/10.1016/0020-7683(86)90014-4` (1986).

32. Pellegrino, S. Structural Computations with the Singular Value Decomposition of the Equilibrium Matrix. *International Journal of Solids and Structures* **30,** 3025–3035 (1993).

33. Calladine, C. R. Buckminster Fuller's "Tensegrity" structures and Clerk Maxwell's rules for the construction of stiff frames. *International Journal of Solids and Structures* **14,** 161–172. ISSN: 00207683. `http://dx.doi.org/10.1016/0020-7683(78)90052-5` (1978).

34. O'Masta, M. R., Dong, L., St-Pierre, L., Wadley, H. N. & Deshpande, V. S. The fracture toughness of octet-truss lattices. *Journal of the Mechanics and Physics of Solids* **98,** 271–289. ISSN: 00225096 (Jan. 2017).

35. Maiti, S. K., Ashby, M. F. & Gibson, L. J. Fracture toughness of brittle cellular solids. *Scripta Metallurgica* **18,** 213–217 (1984).

36. Paulose, J., Meeussen, A. S. & Vitelli, V. Selective buckling via states of self-stress in topological metamaterials. *Proceedings of the National Academy of Sciences of the United States of America* **112,** 7639–7644. ISSN: 10916490 (June 2015).

37. Meza, L. R. *et al.* Reexamining the mechanical property space of three-dimensional lattice architectures. *Acta Materialia* **140,** 424–432. ISSN: 13596454 (Nov. 2017).

38. Portela, C. M., Greer, J. R. & Kochmann, D. M. Impact of node geometry on the effective stiffness of non-slender three-dimensional truss lattice architectures. *Extreme Mechanics Letters* **22,** 138–148. ISSN: 23524316. `https://doi.org/10.1016/j.eml.2018.06.004` (2018).

39. Mateos, A. J., Huang, W., Zhang, Y. W. & Greer, J. R. Discrete-Continuum Duality of Architected Materials: Failure, Flaws, and Fracture. *Advanced Functional Materials* **29.** ISSN: 16163028 (Feb. 2019).

40. Han, S. C., Lee, J. W. & Kang, K. A New Type of Low Density Material: Shellular. *Advanced Materials* **27,** 5506–5511. ISSN: 15214095 (Oct. 2015).

41. Hsieh, M. T., Endo, B., Zhang, Y., Bauer, J. & Valdevit, L. The mechanical response of cellular materials with spinodal topologies. *Journal of the Mechanics and Physics of Solids* **125,** 401–419. ISSN: 00225096 (Apr. 2019).

42. White, B. C., Garland, A., Alberdi, R. & Boyce, B. L. Interpenetrating lattices with enhanced mechanical functionality. *Additive Manufacturing* **38.** ISSN: 22148604 (Feb. 2021).

43. Indurkar, P. P. *et al.* The coupled strength and toughness of interconnected and interpenetrating multi-material gyroids. *MRS Bulletin.* ISSN: 0883-7694. `https://link.springer.com/10.1557/s43577-021-00249-3` (Apr. 2022).

44. Wang, Y., Li, L., Hofmann, D., Andrade, J. E. & Daraio, C. Structured fabrics with tunable mechanical properties. *Nature 2021 596:7871* **596,** 238–243. ISSN: 1476-4687. `https://www.nature.com/articles/s41586-021-03698-7` (Aug. 2021).

45. Li, M. Z., Stephani, G. & Kang, K. J. New cellular metals with enhanced energy absorption: Wire-woven bulk kagome (WBK)-metal hollow sphere (MHS) hybrids. *Advanced Engineering Materials* **13,** 33–37. ISSN: 14381656 (Feb. 2011).

46. Ryan, S. M. *et al.* Damping behavior of 3D woven metallic lattice materials. *Scripta Materialia* **106,** 1–4. ISSN: 13596462 (Sept. 2015).

47. Salari-Sharif, L. *et al.* Damping of selectively bonded 3D woven lattice materials. *Scientific Reports* **8,** 6–11. ISSN: 20452322 (Dec. 2018).

48. Yan, D. *et al.* Soft three-dimensional network materials with rational biomimetic designs. *Nature Communications* **11,** 1–11. ISSN: 20411723. `http://dx.doi.org/10.1038/s41467-020-14996-5` (2020).

49. Rybenkov, V. V., Cozzarelli, N. R. & Vologodskii, A. V. Probability of DNA knotting and the effective diameter of the DNA double helix. *Proceedings of the National Academy of Sciences of the United States of America* **90,** 5307–5311. ISSN: 00278424. `https://www.pnas.org` (1993).

50. Arai, Y. *et al.* Tying a molecular knot with optical tweezers. *Nature* **399,** 446–448. ISSN: 00280836 (1999).

51. Frank-Kamenetskii, M. D., Lukashin, A. V. & Vologodskii, A. V. Statistical mechanics and topology of polymer chains. *Nature* **258,** 398–402. ISSN: 00280836 (1975).

52. Saitta, A. M., Soper, P. D., Wasserman, E. & Klein, M. L. Influence of a knot on the strength of a polymer strand. *Nature* **399,** 46–48. `https://www.nature.com/articles/19935` (1999).

53. Crowell, R. H. & Fox, R. H. *Introduction to Knot Theory* (eds Halmos, P. R., Gehring, F. W. & Moore, C. C.) ISBN: 0387902724 (Springer-Verlag, New York, 1963).

54. Frank-Kamenetskii, M. D. & Vologodskii, A. V. Topological Aspects Of The Physics Of Polymers: The Theory And Its Biophysical Applications. *Soviet Physics - Uspekhi* **24,** 679–696. ISSN: 21695296 (1981).

55. Polster, B. Mathematics: What is the best way to lace your shoes? *Nature* **420,** 476. ISSN: 00280836 (2002).

56. Daily-Diamond, C. A., Gregg, C. E. & O'Reilly, O. M. The roles of impact and inertia in the failure of a shoelace knot. *Proceedings of the Royal Society A: Mathematical, Physical and Engineering Sciences* **473.** ISSN: 14712946 (Apr. 2017).

57. Patil, V. P., Sandt, J. D., Kolle, M. & Dunkel, J. Topological mechanics of knots and tangles. *Science* **367,** 71–75. ISSN: 10959203 (Jan. 2020).

58. Pieranski, P., Kasas, S., Dietler, G., Dubochet, J. & Stasiak, A. Localization of breakage points in knotted strings. *New Journal of Physics* **3.** `http://www.njp.org/` (2001).

59. Uehara, H., Kimura, H., Aoyama, A., Yamanobe, T. & Komoto, T. Effects of knot characteristics on tensile breaking of a polymeric monofilament. *New Journal of Physics* **9.** ISSN: 13672630 (Mar. 2007).

60. Przybyl, S. & Pieranski, P. Tightening of the elastic overhand knot. *Physical Review E - Statistical, Nonlinear, and Soft Matter Physics* **79,** 1–5. ISSN: 15393755 (Mar. 2009).

61. Johanns, P. *et al.* The shapes of physical trefoil knots. *Extreme Mechanics Letters* **43,** 101172. ISSN: 23524316 (Feb. 2021).

62. Jawed, M. K., Dieleman, P., Audoly, B. & Reis, P. M. Untangling the Mechanics and Topology in the Frictional Response of Long Overhand Elastic Knots. *Physical Review Letters* **115,** 1–5. ISSN: 10797114 (2015).

63. Pugno, N. M. The "Egg of Columbus" for making the world's toughest fibres. *PLoS ONE* **9,** 1–6. ISSN: 19326203 (Apr. 2014).

64. Berardo, A., Pantano, M. F. & Pugno, N. M. Slip knots and unfastening topologies enhance toughness without reducing strength of silk fibroin fibres. *Interface Focus* **6.** ISSN: 20428901 (Feb. 2016).

65. Pantano, M. F., Berardo, A. & Pugno, N. M. Tightening slip knots in raw and degummed silk to increase toughness without losing strength. *Scientific Reports* **6,** 1–8. ISSN: 20452322 (Feb. 2016).

66. Oakdale, J. S., Ye, J., Smith, W. L. & Biener, J. Post-print UV curing method for improving the mechanical properties of prototypes derived from two-photon lithography. *Optics Express* **24,** 27077. ISSN: 1094-4087 (2016).

67. Weaver, J. C. *et al.* The stomatopod dactyl club: A formidable damage-tolerant biological hammer. *Science* **336,** 1275–1280. ISSN: 10959203 (2012).

68. Launey, M. E., Chen, P. Y., McKittrick, J. & Ritchie, R. O. Mechanistic aspects of the fracture toughness of elk antler bone. *Acta Biomaterialia* **6,** 1505–1514. ISSN: 17427061. `http://dx.doi.org/10.1016/j.actbio.2009.11.026` (2010).

69. Launey, M. E., Buehler, M. J. & Ritchie, R. O. On the Mechanistic Origins of Toughness in Bone. *Annu. Rev. Mater. Res* **40,** 25–53. `www.annualreviews.org` (2010).

70. Barthelat, F. & Espinosa, H. D. An experimental investigation of deformation and fracture of nacre-mother of pearl. *Experimental Mechanics* **47,** 311–324. ISSN: 00144851 (June 2007).

71. Torrents, A., Schaedler, T. A., Jacobsen, A. J., Carter, W. B. & Valdevit, L. Characterization of nickel-based microlattice materials with structural hierarchy from the nanometer to the millimeter scale. *Acta Materialia* **60,** 3511–3523. ISSN: 13596454. `http://dx.doi.org/10.1016/j.actamat.2012.03.007` (2012).

72. Minas, C., Carnelli, D., Tervoort, E. & Studart, A. R. 3D Printing of Emulsions and Foams into Hierarchical Porous Ceramics. *Advanced Materials* **28,** 9993–9999. ISSN: 15214095 (2016).

73. Fronk, M. D. *et al.* Acoustic non-reciprocity in lattices with nonlinearity, internal hierarchy, and asymmetry: Computational study. *Journal of Vibration and Acoustics, Transactions of the ASME* **141,** 1–11. ISSN: 15288927 (2019).

74. Chen, Y. & Wang, L. Harnessing structural hierarchy to design stiff and lightweight phononic crystals. *Extreme Mechanics Letters* **9,** 91–96. ISSN: 23524316. `http://dx.doi.org/10.1016/j.eml.2016.05.009` (2016).

75. Chen, Y., Jia, Z. & Wang, L. Hierarchical honeycomb lattice metamaterials with improved thermal resistance and mechanical properties. *Composite Structures* **152,** 395–402. ISSN: 02638223 (2016).

76. Xu, H., Farag, A. & Pasini, D. Multilevel hierarchy in bi-material lattices with high specific stiffness and unbounded thermal expansion. *Acta Materialia* **134,** 155–166. ISSN: 13596454. `http://dx.doi.org/10.1016/j.actamat.2017.05.059` (2017).

77. Gu, G. X., Takaffoli, M. & Buehler, M. J. Hierarchically Enhanced Impact Resistance of Bioinspired Composites. *Advanced Materials* **29,** 1–7. ISSN: 15214095 (2017).

78. Rayneau-Kirkhope, D., Mao, Y. & Farr, R. Optimization of fractal space frames under gentle compressive load. *Physical Review E - Statistical, Nonlinear, and Soft Matter Physics* **87,** 1–7. ISSN: 15393755 (2013).

79. Tancogne-Dejean, T. & Mohr, D. Elastically-isotropic elementary cubic lattices composed of tailored hollow beams. *Extreme Mechanics Letters* **22,** 13–18. ISSN: 23524316 (July 2018).

80. Bauer, J. *et al.* Nanolattices: An Emerging Class of Mechanical Metamaterials. *Advanced Materials* **29,** 1701850. ISSN: 09359648. `http://doi.wiley.com/10.1002/adma.201701850` (Oct. 2017).

81. Guell Izard, A., Bauer, J., Crook, C., Turlo, V. & Valdevit, L. Ultrahigh Energy Absorption Multifunctional Spinodal Nanoarchitectures. *Small* **15,** 1–8. ISSN: 16136829 (2019).

82. Bauer, J., Schroer, A., Schwaiger, R. & Kraft, O. Approaching theoretical strength in glassy carbon nanolattices. *Nature Materials* **15,** 438–443. ISSN: 14764660 (2016).

83. Tancogne-Dejean, T., Spierings, A. B. & Mohr, D. Additively-manufactured metallic micro-lattice materials for high specific energy absorption under static and dynamic loading. *Acta Materialia* **116,** 14–28. ISSN: 13596454. `http://dx.doi.org/10.1016/j.actamat.2016.05.054` (2016).

84. Bonatti, C. & Mohr, D. Large deformation response of additively-manufactured FCC metamaterials: From octet truss lattices towards continuous shell mesostructures. *International Journal of Plasticity* **92,** 122–147. ISSN: 07496419 (2017).

85. Berger, J. B., Wadley, H. N. & McMeeking, R. M. Mechanical metamaterials at the theoretical limit of isotropic elastic stiffness. *Nature 2016 543:7646* **543,** 533–537. ISSN: 1476-4687. `https://www.nature.com/articles/nature21075` (Feb. 2017).

86. Tancogne-Dejean, T., Diamantopoulou, M., Gorji, M. B., Bonatti, C. & Mohr, D. 3D Plate-Lattices: An Emerging Class of Low-Density Metamaterial Exhibiting Optimal Isotropic Stiffness. *Advanced Materials* **30,** 1–6. ISSN: 15214095 (2018).

87. Crook, C. *et al.* Plate-nanolattices at the theoretical limit of stiffness and strength. *Nature Communications* **11.** ISSN: 20411723 (Dec. 2020).

88. Bonatti, C. & Mohr, D. Mechanical performance of additively-manufactured anisotropic and isotropic smooth shell-lattice materials: Simulations & experiments. *Journal of the Mechanics and Physics of Solids* **122,** 1–26. ISSN: 00225096 (Jan. 2019).

89. Al-Ketan, O. *et al.* Microarchitected Stretching-Dominated Mechanical Metamaterials with Minimal Surface Topologies. *Advanced Engineering Materials* **20.** ISSN: 15272648 (2018).

90. Portela, C. M. *et al.* Extreme mechanical resilience of self-assembled nanolabyrinthine materials. *Proceedings of the National Academy of Sciences of the United States of America* **117,** 5686–5693 (2020).

91. Rogers, J. A., Someya, T. & Huang, Y. Materials and mechanics for stretchable electronics. *Science* **327,** 1603–1607. ISSN: 00368075 (2010).

92. Ko, H. C. *et al.* A hemispherical electronic eye camera based on compressible silicon optoelectronics. *Nature* **454,** 748–753. ISSN: 14764687 (2008).

93. Shaw, L. A. *et al.* Computationally efficient design of directionally compliant metamaterials. *Nature Communications* **10,** 1–13. ISSN: 20411723. `http://dx.doi.org/10.1038/s41467-018-08049-1` (2019).

94. Ronan, W., Deshpande, V. S. & Fleck, N. A. The tensile ductility of cellular Solids: The role of imperfections. *International Journal of Solids and Structures* **102-103,** 200–213. ISSN: 00207683. `http://dx.doi.org/10.1016/j.ijsolstr.2016.10.004` (2016).

95. Bauer, J. *et al.* Push-to-pull tensile testing of ultra-strong nanoscale ceramic-polymer composites made by additive manufacturing. *Extreme Mechanics Letters* **3,** 105–112. ISSN: 23524316 (2015).

96. Montemayor, L. C., Wong, W. H., Zhang, Y. W. & Greer, J. R. Insensitivity to Flaws Leads to Damage Tolerance in Brittle Architected Meta-Materials. *Scientific Reports* **6.** ISSN: 20452322 (Feb. 2016).

97. Bauer, J. *et al.* Programmable Mechanical Properties of Two-Photon Polymerized Materials: From Nanowires to Bulk. *Advanced Materials Technologies* **4,** 1900146. ISSN: 2365-709X. `https://onlinelibrary.wiley.com/doi/full/10.1002/admt.201900146%20https://onlinelibrary.wiley.com/doi/abs/10.1002/admt.201900146%20https://onlinelibrary.wiley.com/doi/10.1002/admt.201900146` (Sept. 2019).

98. Berdova, M. *et al.* Mechanical assessment of suspended ALD thin films by bulge and shaft-loading techniques. *Acta Materialia* **66,** 370–377. ISSN: 13596454 (Mar. 2014).

99. Duncan, R. N. The Metallurgical Structure of Electroless Nickel Deposits: Effect on Coating Properties. *Plating and surface finishing* **83,** 65–69 (1996).

100. Weil, R., Lee, J. H., Kim, I. & Parker, K. Comparison of some mechanical and corrosion properties of electroless and electroplated nickel-phosphorous alloys. *Plating and Surface Finishing* **76,** 62–66. ISSN: 03603164 (1989).

101. Jen, S. H., Bertrand, J. A. & George, S. M. Critical tensile and compressive strains for cracking of Al 2O3 films grown by atomic layer deposition. *Journal of Applied Physics* **109.** ISSN: 00218979 (2011).

102. Tertuliano, O. A., Edwards, B. W., Meza, L. R., Deshpande, V. S. & Greer, J. R. Nanofibril-mediated fracture resistance of bone. *Bioinspiration and Biomimetics* **16.** ISSN: 17483190 (May 2021).

103. Miserez, A. *et al.* Effects of laminate architecture on fracture resistance of sponge biosilica: Lessons from nature. *Advanced Functional Materials* **18,** 1241–1248. ISSN: 1616301X (Apr. 2008).

104. Fernandes, M. C., Aizenberg, J., Weaver, J. C. & Bertoldi, K. Mechanically robust lattices inspired by deep-sea glass sponges. *Nature Materials* **20,** 237–241. ISSN: 14764660 (Feb. 2021).

105. Monn, M. A., Weaver, J. C., Zhang, T., Aizenberg, J. & Kesari, H. New functional insights into the internal architecture of the laminated anchor spicules of Euplectella aspergillum. *Proceedings of the National Academy of Sciences of the United States of America* **112,** 4976–4981. ISSN: 10916490 (Apr. 2015).

106. Shi, S., Li, Y., Ngo-Dinh, B. N., Markmann, J. & Weissmüller, J. Scaling behavior of stiffness and strength of hierarchical network nanomaterials. *Science* **371,** 1026–1033. ISSN: 10959203. `https://www.science.org/doi/full/10.1126/science.abd9391` (Mar. 2021).

107. Frölich, A., Fischer, J., Zebrowski, T., Busch, K. & Wegener, M. Titania woodpiles with complete three-dimensional photonic bandgaps in the visible. *Advanced Materials* **25,** 3588–3592. ISSN: 09359648 (July 2013).

108. Harris, J. A., Winter, R. E. & McShane, G. J. Impact response of additively manufactured metallic hybrid lattice materials. *International Journal of Impact Engineering* **104,** 177–191. ISSN: 0734743X (June 2017).

109. Portela, C. M. *et al.* Supersonic impact resilience of nanoarchitected carbon. *Nature Materials* **20,** 1491–1497. ISSN: 14764660 (2021).

110. Rayneau-Kirkhope, D., Mao, Y. & Farr, R. Ultralight fractal structures from hollow tubes. *Physical Review Letters* **109,** 204301. ISSN: 00319007. `https://journals.aps.org/prl/abstract/10.1103/PhysRevLett.109.204301` (Nov. 2012).

111. Ajdari, A., Jahromi, B. H., Papadopoulos, J., Nayeb-Hashemi, H. & Vaziri, A. Hierarchical honeycombs with tailorable properties. *International Journal of Solids and Structures* **49,** 1413–1419. ISSN: 00207683 (June 2012).

112. Oftadeh, R., Haghpanah, B., Vella, D., Boudaoud, A. & Vaziri, A. Optimal fractal-like hierarchical honeycombs. *Physical Review Letters* **113.** ISSN: 10797114 (Sept. 2014).

113. Kooistra, G. W., Deshpande, V. & Wadley, H. N. Hierarchical corrugated core sandwich panel concepts. *Journal of Applied Mechanics, Transactions ASME* **74,** 259–268. ISSN: 00218936 (Mar. 2007).

114. Malek, S. & Gibson, L. Effective elastic properties of periodic hexagonal honeycombs. *Mechanics of Materials* **91,** 226–240. ISSN: 01676636 (Dec. 2015).

115. Shan, S. *et al.* Multistable Architected Materials for Trapping Elastic Strain Energy. *Advanced Materials* **27,** 4296–4301. ISSN: 15214095 (Aug. 2015).

116. Haghpanah, B., Salari-Sharif, L., Pourrajab, P., Hopkins, J. & Valdevit, L. Multistable Shape-Reconfigurable Architected Materials. *Advanced Materials* **28,** 7915–7920. ISSN: 1521-4095. `https://onlinelibrary.wiley.com/doi/full/10.1002/adma.201601650%20https://onlinelibrary.wiley.com/doi/abs/10.1002/adma.201601650%20https://onlinelibrary.wiley.com/doi/10.1002/adma.201601650` (Sept. 2016).

117. Traugutt, N. A. *et al.* Liquid-Crystal-Elastomer-Based Dissipative Structures by Digital Light Processing 3D Printing. *Advanced Materials* **32.** ISSN: 15214095 (July 2020).

118. Frenzel, T. *et al.* Tailored Buckling Microlattices as Reusable Light-Weight Shock Absorbers. *Advanced Materials* **28,** 5865–5870. ISSN: 1521-4095. `https://onlinelibrary.wiley.com/doi/full/10.1002/adma.201600610%20https://onlinelibrary.wiley.com/doi/abs/10.1002/adma.201600610%20https://onlinelibrary.wiley.com/doi/10.1002/adma.201600610` (July 2016).

119. Salari-Sharif, L., Valdevit, L. & Schaedler, T. A. Energy dissipation mechanisms in hollow metallic microlattices. *Journal of Materials Research* **29,** 1755–1770. ISSN: 20445326 (Aug. 2014).

120. Garland, A. P. *et al.* Coulombic friction in metamaterials to dissipate mechanical energy. *Extreme Mechanics Letters* **40.** ISSN: 23524316 (Oct. 2020).

121. Li, J., Chen, Z., Li, Q., Jin, L. & Zhao, Z. Harnessing Friction in Intertwined Structures for High-Capacity Reusable Energy-Absorbing Architected Materials. *Advanced Science.* ISSN: 21983844 (May 2022).

122. Moestopo, W. P., Mateos, A. J., Fuller, R. M., Greer, J. R. & Portela, C. M. Pushing and Pulling on Ropes: Hierarchical Woven Materials. *Advanced Science* **7,** 1–8. ISSN: 21983844 (Oct. 2020).

123. Li, Y. & Pellegrino, S. A Theory for the Design of Multi-Stable Morphing Structures. *Journal of the Mechanics and Physics of Solids* **136.** ISSN: 00225096 (Mar. 2020).

124. Maeda, N., Chen, N., Tirrell, M. & Israelachvili, J. N. *Adhesion and Friction Mechanisms of Polymer-on-Polymer Surfaces* tech. rep. (2002). `https://www.science.org`.

125. Gengenbach, T. R., Major, G. H., Linford, M. R. & Easton, C. D. Practical guides for x-ray photoelectron spectroscopy (XPS): Interpreting the carbon 1s spectrum. *Journal of Vacuum Science & Technology A: Vacuum, Surfaces, and Films* **39,** 013204. ISSN: 0734-2101. `https://avs.scitation.org/doi/abs/10.1116/6.0000682` (Jan. 2021).

126. Shard, A. G. Practical guides for x-ray photoelectron spectroscopy: Quantitative XPS. *Journal of Vacuum Science & Technology A: Vacuum, Surfaces, and Films* **38,** 041201. ISSN: 0734-2101. `https://avs.scitation.org/doi/abs/10.1116/1.5141395` (July 2020).

127. Bauer, J., Schroer, A., Schwaiger, R. & Kraft, O. The Impact of Size and Loading Direction on the Strength of Architected Lattice Materials. *Advanced Engineering Materials* **18,** 1537–1543. ISSN: 15272648 (Sept. 2016).

128. McClure, C. D., Oldham, C. J. & Parsons, G. N. Effect of Al2O3 ALD coating and vapor infusion on the bulk mechanical response of elastic and viscoelastic polymers. *Surface and Coatings Technology* **261,** 411–417. ISSN: 02578972 (Jan. 2015).

129. Bauer, J. *et al.* Thermal post-curing as an efficient strategy to eliminate process parameter sensitivity in the mechanical properties of two-photon polymerized materials. *Optics Express, Vol. 28, Issue 14, pp. 20362-20371* **28,** 20362–20371. ISSN: 1094-4087. `https://opg.optica.org/viewmedia.cfm?uri=oe-28-14-20362&seq=0&html=true%20https://opg.optica.org/abstract.cfm?uri=oe-28-14-20362%20https://opg.optica.org/oe/abstract.cfm?uri=oe-28-14-20362` (July 2020).

130. Zhang, X., Vyatskikh, A., Gao, H., Greer, J. R. & Li, X. Lightweight, flaw-tolerant, and ultrastrong nanoarchitected carbon. *Proceedings of the National Academy of Sciences of the United States of America* **116,** 6665–6672. ISSN: 10916490 (Apr. 2019).

131. Teyssier, J., Saenko, S. V., Van Der Marel, D. & Milinkovitch, M. C. Photonic crystals cause active colour change in chameleons. *Nature Communications 2015 6:1* **6,** 1–7. ISSN: 2041-1723. `https://www.nature.com/articles/ncomms7368` (Mar. 2015).

132. Forterre, Y., Skotheim, J. M., Dumais, J. & Mahadevan, L. How the Venus flytrap snaps. *Nature* **433,** 421–425. ISSN: 0028-0836. `http://www.nature.com/articles/nature03185` (Jan. 2005).

133. Katti, K. S., Katti, D. R., Pradhan, S. M. & Bhosle, A. Platelet interlocks are the key to toughness and strength in nacre. *Journal of Materials Research* **20,** 1097–1100. ISSN: 08842914 (May 2005).

134. Barthelat, F., Tang, H., Zavattieri, P. D., Li, C. M. & Espinosa, H. D. On the mechanics of mother-of-pearl: A key feature in the material hierarchical structure. *Journal of the Mechanics and Physics of Solids* **55,** 306–337. ISSN: 00225096 (2007).

135. Jeronimidis, G. The fracture behaviour of wood and the relations between toughness and morphology. *Proceedings of the Royal Society of London - Biological Sciences* **208,** 447–460. ISSN: 09628452 (1980).

136. Huang, W. *et al.* A natural impact-resistant bicontinuous composite nanoparticle coating. *Nature Materials* **19,** 1236–1243. ISSN: 14764660 (Nov. 2020).

137. Greenfeld, I., Kellersztein, I. & Wagner, H. D. Nested helicoids in biological microstructures. *Nature Communications 2020 11:1* **11,** 1–12. ISSN: 2041-1723. `https://www.nature.com/articles/s41467-019-13978-6` (Jan. 2020).

138. Hamm, C. E. *et al.* Architecture and material properties of diatom shells provide effective mechanical protection. *Nature* **421,** 841–843. ISSN: 00280836 (2003).

139. Lee, N. *et al.* Hierarchical multiscale structure–property relationships of the red-bellied woodpecker (Melanerpes carolinus) beak. *Journal of The Royal Society Interface* **11.** ISSN: 17425662. `https://royalsocietypublishing.org/doi/10.1098/rsif.2014.0274` (July 2014).

140. Rivera, J. *et al.* Toughening mechanisms of the elytra of the diabolical ironclad beetle. *Nature 2020 586:7830* **586,** 543–548. ISSN: 1476-4687. `https://www.nature.com/articles/s41586-020-2813-8` (Oct. 2020).

141. Magrini, T. *et al.* Transparent and tough bulk composites inspired by nacre. *Nature Communications* **10.** ISSN: 20411723 (Dec. 2019).

142. Magrini, T. *et al.* Transparent Nacre-like Composites Toughened through Mineral Bridges. *Advanced Functional Materials* **30.** ISSN: 16163028 (July 2020).

143. Magrini, T., Bouville, F. & Studart, A. R. Transparent materials with stiff and tough hierarchical structures. *Open Ceramics* **6,** 100109. ISSN: 26665395 (June 2021).

144. Moestopo, W. P., Shaker, S. & Greer, J. R. Knots are Not for Naught: Topology and Material Effects in Hierarchical Intertwined Materials. *In preparation* (2022).

145. Arzt, E., Gorb, S. & Spolenak, R. From micro to nano contacts in biological attachment devices. *Proceedings of the National Academy of Sciences* **100,** 10603–10606. `www.pnas.orgcgidoi10.1073pnas.1534701100` (Sept. 2003).

146. Tian, Y. *et al. Adhesion and friction in gecko toe attachment and detachment* tech. rep. (2006). `www.pnas.orgcgidoi10.1073pnas.0608841103`.

147. Boesel, L. F., Cremer, C., Arzt, E. & Campo, A. D. Gecko-Inspired Surfaces: A Path to Strong and Reversible Dry Adhesives. *Advanced Materials* **22,** 2125–2137. ISSN: 1521-4095. `https://onlinelibrary.wiley.com/doi/full/10.1002/adma.200903200%20https://onlinelibrary.wiley.com/doi/abs/10.1002/adma.200903200%20https://onlinelibrary.wiley.com/doi/10.1002/adma.200903200` (May 2010).

148. Lee, H., Lee, B. P. & Messersmith, P. B. A reversible wet/dry adhesive inspired by mussels and geckos. *Nature* **448,** 338–341. ISSN: 14764687 (July 2007).

149. Grierson, D. S., Flater, E. E. & Carpick, R. W. Accounting for the JKR–DMT transition in adhesion and friction measurements with atomic force microscopy. *Journal of Adhesion Science and Technology* **19,** 291–311. eprint: `https://doi.org/10.1163/1568561054352685`. `https://doi.org/10.1163/1568561054352685` (2005).

150. Hibbeler, R. C. *Mechanics of Materials, Tenth Edition* (Pearson Education Limited, United Kingdom, 2018).

151. He, G., Müser, M. H. & Robbins, M. O. Adsorbed Layers and the Origin of Static Friction. *Science* **284,** 1650–1652. eprint: `https://www.science.org/doi/pdf/10.1126/science.284.5420.1650`. `https://www.science.org/doi/abs/10.1126/science.284.5420.1650` (1999).

152. Rohbeck, N. *et al.* Effect of high strain rates and temperature on the micromechanical properties of 3D-printed polymer structures made by two-photon lithography. *Materials & Design* **195,** 108977. ISSN: 0264-1275. `https://www.sciencedirect.com/science/article/pii/S0264127520305116` (2020).

153. Zavarise, G. & Wriggers, P. Contact with friction between beams in 3-D space. *International Journal for Numerical Methods in Engineering* **49,** 977–1006 (2000).

154. Weeks, J. S. & Ravichandran, G. High strain-rate compression behavior of polymeric rod and plate Kelvin lattice structures. *Mechanics of Materials* **166,** 104216. ISSN: 0167-6636 (Mar. 2022).

155. Braam, J. In touch: Plant responses to mechanical stimuli. *New Phytologist* **165,** 373–389. ISSN: 0028646X (Feb. 2005).

156. Roy, D., Cambre, J. N. & Sumerlin, B. S. Future perspectives and recent advances in stimuli-responsive materials. *Progress in Polymer Science (Oxford)* **35,** 278–301. ISSN: 00796700 (Jan. 2010).

157. Kempaiah, R. & Nie, Z. From nature to synthetic systems: Shape transformation in soft materials. *Journal of Materials Chemistry B* **2,** 2357–2368. ISSN: 20507518 (May 2014).

158. Nojoomi, A., Arslan, H., Lee, K. & Yum, K. Bioinspired 3D structures with programmable morphologies and motions. *Nature Communications* **9,** 1–11. ISSN: 20411723. `http://dx.doi.org/10.1038/s41467-018-05569-8` (Dec. 2018).

159. Ding, Z. *et al.* Direct 4D printing via active composite materials. *Science Advances* **3.** ISSN: 23752548 (Apr. 2017).

160. Sydney Gladman, A., Matsumoto, E. A., Nuzzo, R. G., Mahadevan, L. & Lewis, J. A. Biomimetic 4D printing. *Nature Materials* **15,** 413–418. ISSN: 14764660. `www.nature.com/naturematerials` (Apr. 2016).

161. Kotikian, A. *et al.* Untethered soft robotic matter with passive control of shape morphing and propulsion. *Science Robotics* **4.** ISSN: 24709476. `https://www.science.org/doi/10.1126/scirobotics.aax7044` (Aug. 2019).

162. Guseinov, R., McMahan, C., Pérez, J., Daraio, C. & Bickel, B. Programming temporal morphing of self-actuated shells. *Nature Communications 2020 11:1* **11,** 1–7. ISSN: 2041-1723. `https://www.nature.com/articles/s41467-019-14015-2` (Jan. 2020).

163. Akerson, A., Bourdin, B. & Bhattacharya, K. Optimal design of responsive structures. *Structural and Multidisciplinary Optimization* **65,** 1–18. ISSN: 16151488. `https://link.springer.com/article/10.1007/s00158-022-03200-5` (Apr. 2022).

164. Jackson, J. A. *et al.* Field responsive mechanical metamaterials. *Science Advances* **4** (2018).

165. Momeni, F., M.Mehdi Hassani.N, S., Liu, X. & Ni, J. A review of 4D printing. *Materials and Design* **122,** 42–79. ISSN: 18734197 (May 2017).

Appendix A

SUPPLEMENTARY MOVIES

Movie 1

Video comparing the tensile and compressive behaviors of woven octahedron lattice from Figure 3.2c (shown in red) and monolithic octahedron lattices (shown in gray) for $\bar{\rho} \approx 5\%$ at 150x playback speed. The still image of monolithic octahedron lattice at the end of the video shows the image of the lattice after two cycles of compression up to 70% strain.

Movie 2

Video displaying the tension-compression experiment of a woven diamond lattice ($\bar{\rho} \approx 5\%$) shown in Figure 3.2c at 150x playback speed.

Movie 3

Video of the first three cycles of cyclic tensile testing of a woven octahedron lattice ($\bar{\rho} \approx 5\%$) shown in Figure S3.8 at 500x playback speed.

Movie 4

Video of the first three cycles of cyclic tensile testing of a woven diamond lattice ($\bar{\rho} \approx 5\%$) shown in Figure S3.8 at 500x playback speed.

Movie 5

Video showing an IP-Dip pillar loaded in tension up to failure at 100x playback speed.

Movie 6

Video of hierarchical knotted (left, purple) and woven (right, red) rhombuses with designed height $H = 70\mu\text{m}$ pulled up to failure played at 75x speed, showing a unique knotting mechanism only available in hierarchical knotted rhombus once fibers are aligned to the loading direction.

Movie 7

Video of hierarchical knotted (left, purple) and woven (right, red) rhombuses with designed height $H = 70\mu\text{m}$ cyclically loaded in tension to an increasing strain value in each subsequent cycle with 300x playback speed. Within the first two cycles, both rhombuses returned to shapes close to their undeformed configurations. In the third cycle, the woven rhombus experienced failure whereas the knotted rhombus was tightened and retained its shape after unloading.

Movie 8

Video of hierarchical knotted rhombuses of height $H = 70\mu\text{m}$ (left, dashed line) and 140 µm (right, solid line) loaded in tension up to failure played at 100x speed. The normalized load is defined as the applied load divided by the product of the Young's Modulus of pristine IP-Dip and the fiber cross-sectional area.